



MASTERARBEIT / MASTER'S THESIS

Titel der Masterarbeit / Title of the Master's Thesis

„ The quarry Grossau: faults, fault rocks and effective porosity in the Hauptdolomit Formation “

verfasst von / submitted by

Mag. Harald Zwilling BSc.

angestrebter akademischer Grad / in partial fulfilment of the requirements for the degree of
Master of Science (MSc.)

Wien, 2017 / Vienna 2017

Studienkennzahl lt. Studienblatt /
degree programme code as it appears on
the student record sheet:

A 066 815

Studienrichtung lt. Studienblatt /
degree programme as it appears on
the student record sheet:

Erdwissenschaften

Betreut von / Supervisor:

Dr. Kurt Decker

Mitbetreut von / Co-Supervisor:

>Akademische(r) Grad(e) Vorname Zuname< /
degree(s) first name family name

Table of contents

1.	Introduction: Situation of the quarry, lithology and tectonics	5
1.1	Regional Tectonic History: Deformation in the Northern Calcareous Alps (NCA)	9
1.2	Tectonic history of the Vienna Basin	12
2.	Methodology	14
2.1	Scanlines	14
2.2	Assessment of fault kinematics	18
2.3	Assessing fault frequency	19
2.4	Fault rock classes used for scanlines and porosity estimate	24
2.5	Rock Mass classification by Fracture Density Classes (FDCs).....	28
2.6	Lab determination of open porosity and bulk density for dolomite FDCs and cohesive fault rocks	35
2.7	Sample collection.....	36
2.8	Methodology of thin section preparation	37
3.	Faults in the quarry Grossau	38
3.1	Category 1: SE-E dipping flats and ramps.....	39
3.2	Category 2: Steeply dipping NE-SW striking faults.....	42
3.3	Category 3: NNW-SSE striking faults	44
3.4	Category 5: NE-dipping normal faults.....	46
3.5	Category 6: steeply dipping NS-striking faults	48
3.6	Category 7: E-W striking faults	49
3.7	Tension gashes	51
4.	Quantitative assessment of the anisotropy of the rock mass.....	53
4.1	Spatial distribution of discontinuities of sedimentary origin (bedding and siliciclastic layers).....	53
4.2	Spatial distribution of faults and fault rocks.....	54
4.3	Category 4: WNW-ESE striking faults	56
5.	Fault Rocks in Grossau	57
5.1	Thin section and sample descriptions	57
5.1.1	Sample 1.....	58
5.1.2	Sample 2.....	61
5.1.3	Samples 3 and 3.2	63
5.1.4	Sample 5.2.....	67
5.1.5	Sample 7.2.....	72
5.1.6	Sample 10.....	76
5.1.7	Sample 11.....	82
5.1.8	Sample 13.....	84
5.1.9	Sample 14.....	86
5.2	Classification systems	90
5.2.1	The classic: Sibson 1977	90

5.2.2	Same, same but different: Implosion-, dilation and mosaic-breccias	92
5.2.3	Classification system by fabric	94
5.3	Processes of grain size reduction in fault rocks	95
5.4	Structural indicators for seismic slip on carbonate fault rocks.....	99
6.	Porosity Evaluation.....	104
6.1	Effective porosity of rock samples	104
6.1.1	Effective porosity of fractured dolostones and fault rocks	104
6.1.2	High porosity facies identified during measurements	106
6.2	Porosity evaluation for rock mass without fault rocks.....	108
6.3	Porosity of rock mass including fault rocks	109
7.	Conclusions	113
8.	Literature	115
9.	Appendix	119
	Zusammenfassung	129
	Abstract.....	130

1. Introduction: Situation of the quarry, lithology and tectonics

The Northern Calcareous Alps (NCA) are (according to the dominant model, for a discussion see Frisch & Gawlick 2001, 2002) tectonically separated into three main nappe systems, ordered here from top to base: Juvavikum, Tirolikum and Bajuvarikum.

The quarry Grossau is situated near the western margin of the Vienna basin in the GÖller Nappe System, which is the main nappe of the Tirolikum in the eastern part of the NCA (Tollmann 1966, p.238). It is located in rocks of the Hauptdolomit Formation at the northern border of the Peilstein Nappe to the Lindkogel Nappe of the GÖller Nappe System.

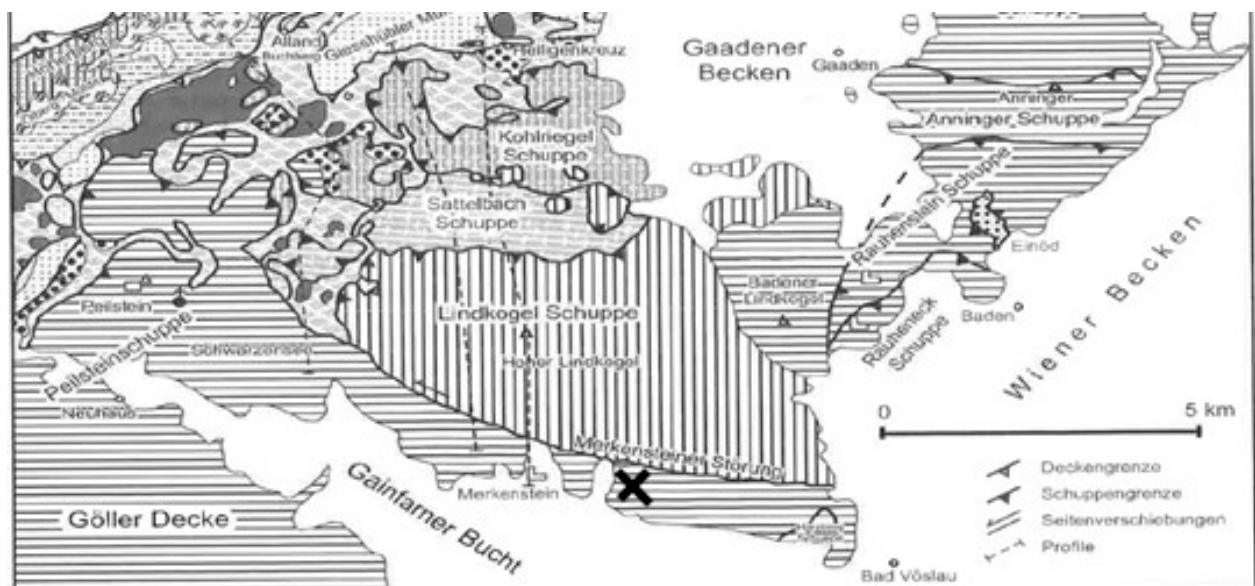


Figure 1: Tectonic map of the Northern Calcareous Alps west of the Vienna Basin. North is up. Black cross marks the position of the quarry Grossau. Modified after Wessely 2008, p. 204.

The northern border of the Peilstein Nappe is formed by an E-W to NW-SE striking, sinistral fault system, the Merkenstein Fault (“Merkensteiner Störung”, compare Figure 1). Subparallel faults belonging to the same system shape the local topography and are of hydrogeological importance (Wessely et al., 2007).

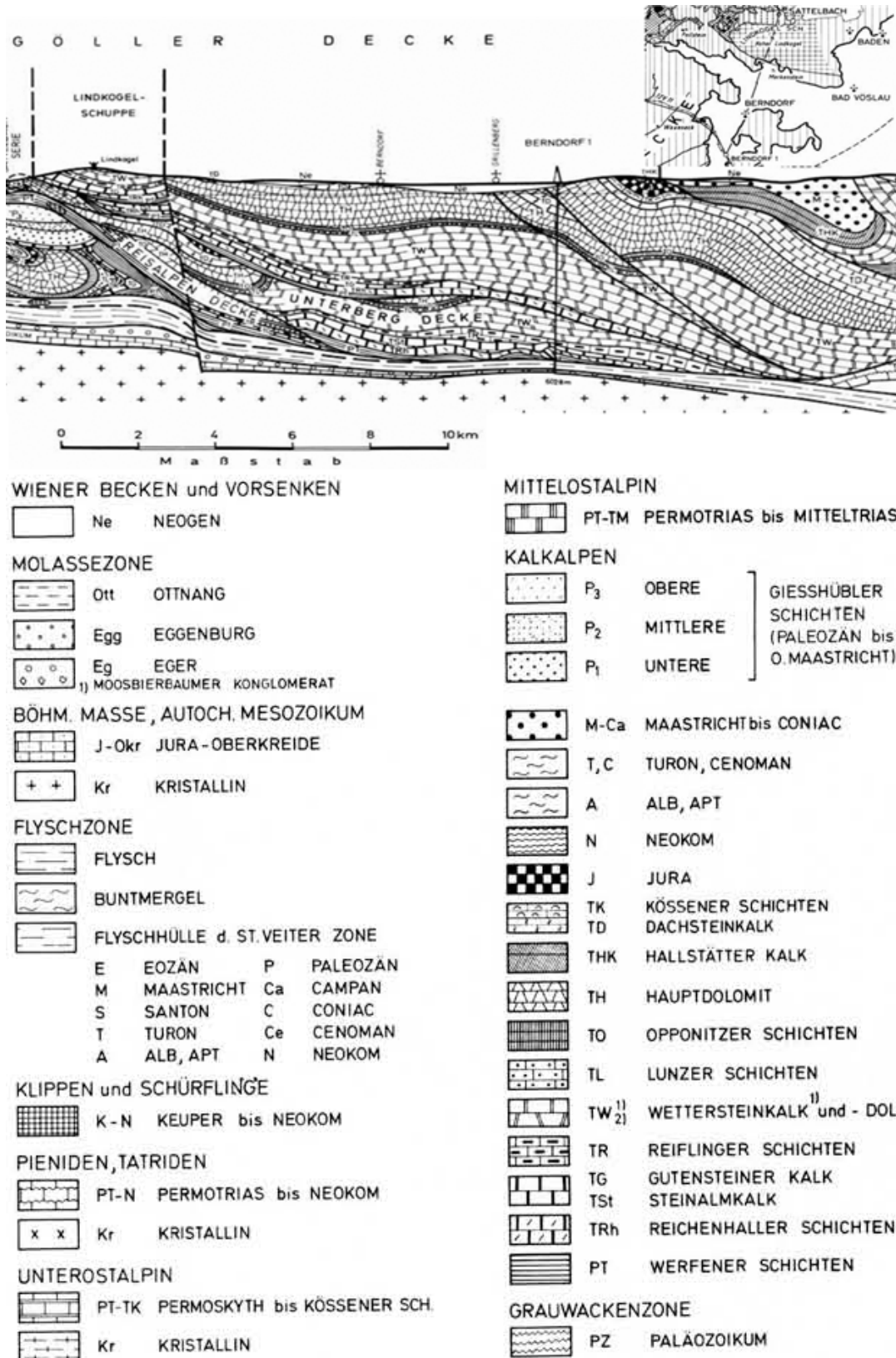


Figure 2: NNE –SSW-Profile across the Göll-Nappe near Grossau. South- to south-east dipping thrust planes and shallow dip of bedding are consistent with the observations made in this work. Modified after Wachtel & Wessely, 1981, Abb. 7.

A huge fault of this system, the Harzberg Fault, crops out well visible along nearly the whole quarry wall, which is formed by a single large slickenside in a closed quarry directly above Bad Vöslau (not Grossau!). This fault was reactivated as normal fault (compare Wessely et al., 2007 p. 428), the slickenlines in this quarry indicate SE directed normal faulting according to my own measurements (Figure 3).

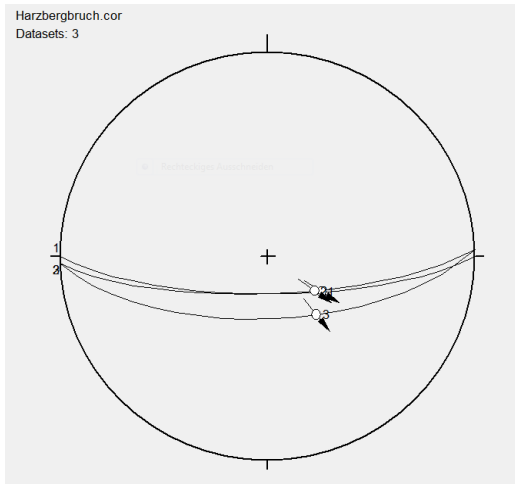


Figure 3: Lower hemisphere Schmidt-net plot of fault slip data from the Harzberg Fault, quarry above Vöslau

Schopper (1991, p. 125) attributes this NW-SE extension at the Harzberg Fault to the formation of the Miocene Berndorf Basin. Middle Miocene NW-SE extension during NE-SW compression is well documented for the area, compare chapter 1.1.

The lithostratigraphy of the Göller Nappe System (see Figure 4) starts with evaporites and siliciclastic rocks of Permian to Triassic age and continues with Triassic to Jurassic mostly carbonate sediments, including those of the Norian Hauptdolomit Formation cropping out in Grossau. After a hiatus, sedimentation continues with siliciclastic sediments of the Upper Cretaceous to Paleogene Nierental and Gießhübl Formation of the Gosau Group.

The outcropping dolomite rocks of the Hauptdolomit Formation at Grossau are interrupted by thin (usually <1cm) layers of green, grey or brown fine siliciclastic layers ("Keuper") in irregular intervals ranging from 0.2 m to more than 8.56 m (the outcrop ended before another siliciclastic layer was encountered). The dolostones show a dominance of dark grey beds with some reddish or lighter colored beds often showing lamination, beds with vuggy porosity and rarely sugar grained beds. Dolomite bed thickness varies between 6.20 and 0.12m.

Göller-Decke

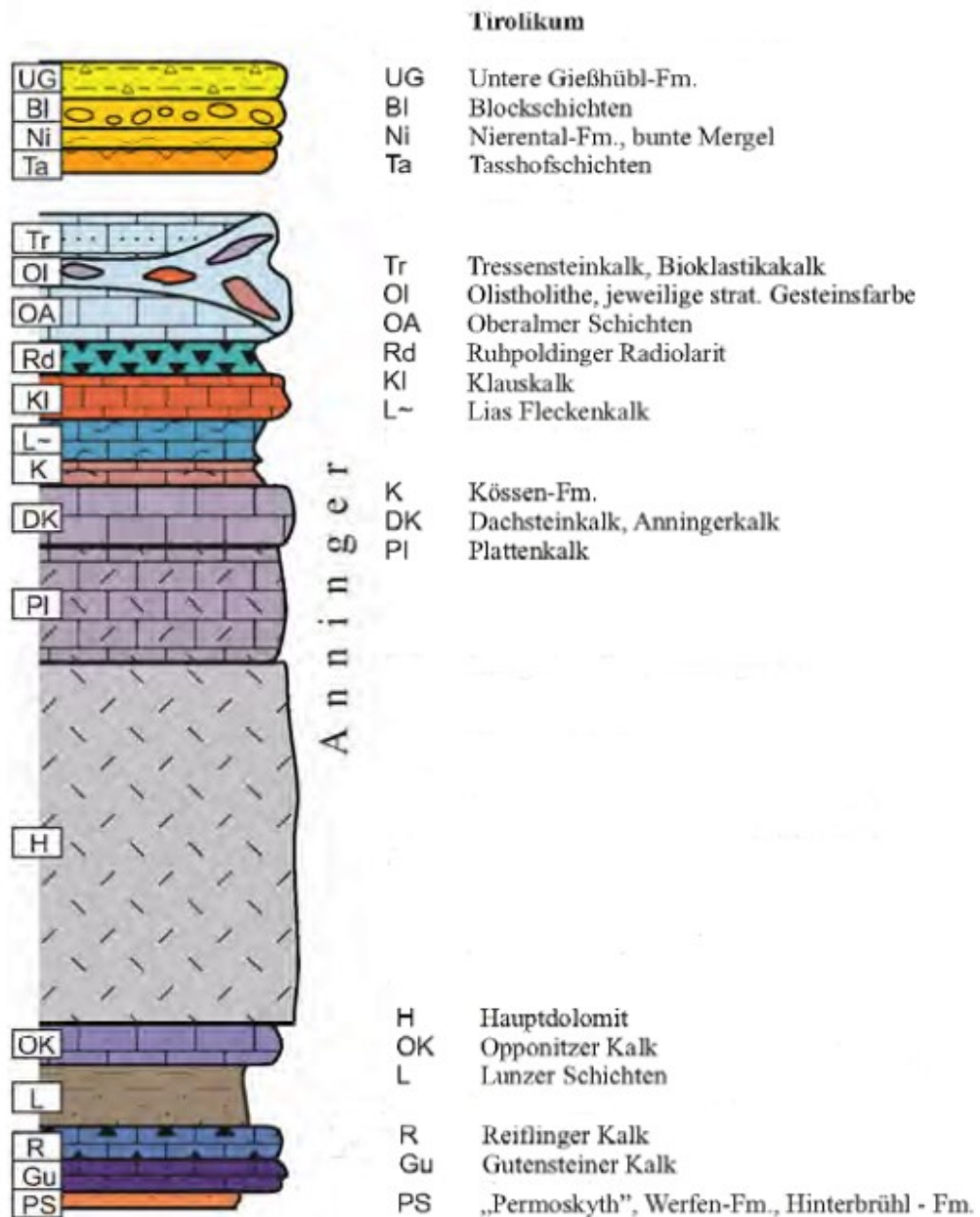


Figure 4: Stratigraphic profile through the Göller Nappe System. Thicknesses not to scale. Modified after Wessely 2013, p.16. Graph is from a historic source and contains local formation names, which do not conform with ICS rules.

The different color and grain size of dolostone beds show some similarity with the Hauptdolomit Fm. of the Frankenfels-Lunzer Nappe (Wessely, 1993, pp. 255-256) and the lower Hauptdolomit Fm. of the Göller Nappe System encountered in Schönkirchen Tief which is characterized by darker dolomite and an abundance of siliciclastic (Keuper) layers (Wessely, 1993, p. 257).

The dolostone succession is heavily fractured and crosscut by a multitude of faults, which have their origin in the complex tectonic histories of the Northern Calcareous Alps and the nearby Vienna Basin, which are summarized in Table 1 and Table 2 in the next chapter.

1.1 Regional Tectonic History: Deformation in the Northern Calcareous Alps (NCA)

The rocks now forming the main part of the Göller Nappe System (including the Hauptdolomit Fm.) are carbonates sedimented in a tectonically calm environment during the Triassic and Jurassic in the southern Tethys. They were sedimented on rocks of the (partly) siliciclastic Early Triassic Werfen Formation and evaporites of the so called "Hinterbrühl Formation".

These evaporites and siliciclastics formed the detachment horizon (and now form the base of the Göller Nappe System) when these units were thrust towards NW in the Lower Cretaceous (around 135 Ma ago) during the so called "ealpine event", which involved southward subduction of parts of the Adriatic plate. Whether this happened as the northern part got subducted southwards under the southern part of Adria within an intracontinental subduction zone or by one or another kind of oceanic subduction is still a matter of discussion (compare Schuster & Stüwe, 2010). This detachment of the alpine nappes is fractally mirrored within the Göller Nappe System in the small scale by normal faults which formed along siliciclastic Keuper layers within the Hauptdolomit Fm. of Grossau. Generally, the deformation style within the Tyrolian nappes is defined by the brittle Triassic dolomites: thrusting dominates over folding as a way of shortening. A fact that is mirrored on the outcrop scale in Grossau in the relative abundance of thrust faults and lack of folds.

Basins within the ealpine fold and thrust belt served as sedimentation space for the Gosau Group (compare e.g. Stern & Wagreich, 2013, p.2) which now forms the youngest sediments in the sedimentary succession of the Göller Nappe System ("Tasshof-Schichten", "Blockschichten", Gießhübel Formation, Nierental Formation = "Nierentaler Schichten" in Figure 4).

In the Paleogene (see Peresson & Decker, 1997 for the ideas repeated here), the north directed continental collision between Adria (upper plate) and Europe (lower plate) after the closing of the Penninic Ocean that separated them is the driving tectonic force. The onset of collision is dated to 53 Ma (Early Eocene) via the age of the youngest sediments of the Penninic Ocean (Flysch). In this process, the nappes of the NCA first are thrust over the remains of the Penninic ocean and the sediments on the

southern shelf of Europe, finally incorporating these in the thrust wedge as the Penninic and Helvetic Nappes. In the Neogene, the Molasse sediments of the foreland basin produced by the collision get overthrust during (Oligocene to Early Miocene). During this process, the northward-moving Adriatic Plate rotates counterclockwise, generating, in the beginning, a stress field dominated by NW-compression. This process produced NW-directed fold and thrust structures and WNW-trending dextral strike-slip faults (D1).

A major change in the stress field and consequently in deformation occurs when the Periadriatic Fault decouples the Eastern Alps from the rotation of Adria between late Eocene and Middle Miocene by taking up the rotation component. This resulted in a stress field with N-S compression. Sinistral, NE-SW striking faults like the SEMP Fault System (Linzer et al., 1995) develop in the north, while dextral faults develop in the south allowing for the eastward extrusion of the Eastern Alps. This is aided by a retreating subduction zone at the Carpathian plate boundary to the east not just allowing material transfer in this direction, but even pulling out material to the east (D2).

The sum of the forces of the northward movement of the Adriatic Plate and eastward extrusion produces a stress field of NE-SW compression. This results in NE-directed thrusts to the west of the spur of the Bohemian Massif but extensional structures (NW-SE directed normal faulting) in the area of interest of this work, which is located to the east of the spur. Last but not least it generates (E)NE striking sinistral faults that branch off from the SEMP Fault System (D3).

Increasing dominance of the eastward extrusion over the N-S-shortening opens the Vienna Basin along some of these NE striking sinistral faults formed during D3. E-directed normal faulting is the dominant expression of eastward extension (D4). E-directed extension is inverted to E directed compression in the late Miocene, likely when after the subduction of all oceanic crust thick and buoyant European continental crust entered the subduction zone and the European and Carpathian plate got more and more mechanically coupled and thereby exerted E-W directed far-field stress (D5).

During D6 the convergence between Adria and Europe continues at slow rates up to the present (compare Weber et al., 2009) resulting in continued N-S compression. In spite of these boundary conditions, Peresesson and Decker (1997) identified normal faulting along the northern margin of the Eastern Alps. The significance of this deformation is not understood.

Phase	Chronostratigraphic age	Direction of compression/extension	Tectonic reason	Associated structures (strike/shear sense) and events
D0	Lower to middle cretaceous	NW-SE compression	Oceanic or intercontinental subduction	NW- and SE-directed reverse faults NE-SW trending fold axes
D1	Eocene to Early Miocene	NW-SE Compression	Adria moves northwards into Europe rotating counterclockwise	WNW-ESE striking dextral strike-slip faults N-S striking sinistral strike-slip faults NW-and SE-directed reverse faults
D2	Late Eocene-Middle Miocene	NS Compression	PAF* decouples the eastern alps from the rotation of Adria. Onset of eastward extrusion of the Eastern Alps,	NW-SE-striking dextral strike-slip faults NE-SW-striking sinistral strike-slip faults N- and S-directed reverse faults
D3	Middle Miocene	NE Compression		NE- and SW-directed reverse faults N-S striking dextral strike-slip faults ENE-WSW striking sinistral faults
D4	Middle Miocene	E-W-Extension	Drag from the eastward extruding eastern Alps	At the eastern margin of the NCA the Vienna Basin opens along sin faults from D 3 Extension: E- and W-directed normal faults
D5	Late Miocene	E - W Compression	End of mass transfer to E	ENE-WSW striking dextral strike-slip faults WNW-ESE striking sinistral strike-slip faults
D6	Late to post-Miocene	N-S Compression		Extension: Ndirected normal faults

Table 1: Deformation events in the NCA. Modified after (Peresson & Decker, 1997), (Piller et al., 1996) *PAF: Periadriatic Fault

1.2 Tectonic history of the Vienna Basin

As the quarry lies right next to the well-researched Vienna Basin a similar (e.g. sinistral SEMP branches during D3) or connected (e.g. normal faults towards the basin) deformation history can be assumed. For this reason, the tectonic history of the basin is shortly reviewed, starting with the Early Miocene deformation.

Between the Eggenburgian and the Karpatian a piggy-back basin formed on top of the Eastern Alpine thrust units as they were thrust towards NW (Hölzel et al., 2010). During lateral extrusion, the Vienna Basin was formed as a pull apart basin between overstepping sinistral, NE-SW striking strike-slip faults. This deformation corresponds to D4 identified in the NCA (Table 1). With the end of lateral extrusion and the inversion of the stress field pull-apart subsidence terminated and the former sinistral faults that shaped the pull-apart were partly reactivated as dextral faults (D5). In the Pliocene to early Quaternary, deformation in the basin changed to NE-SW-directed extension, which, (east in its northern part, led to the formation of grabens and half grabens. Decker et al. (2005, p. 312) describe NE-SW extension on NW striking normal faults Kutý-Dobruška area of Slovakia and the Czech Morava Graben near Olomouc. Cross cutting relations constrained the age of these faults to Pliocene to Quaternary. The normal faults are crosscut by active faults, but offset Miocene NE-striking faults of the Vienna basin (Salcher et al., 2012, Decker et al., 2005). Active faulting in the basin results from current N-S directed compression between the Adriatic and the European Plates (D6, Table 1).

Phase	Chronostratigraphic age	Sedimentation-space / tectonic events	Stress field
Proto-basin-phase ≈ D1	Eggenburgian-Karpatian (Burdigalium)	Piggy-back basin on the alpine- carpathian thrust sheets	NW-SE compression
Pull -apart-basin formation ≈(D2), D3, D4	Badenian -upper Panno- nian (upper Burdigalian to upper Tortonian)	Pull-apart basin along NE-striking sinistral faults (// to SEMP-Branches)	E-W extension
End of pull-apart-basin formation D5	Upper Pannonian (upper Tortonian)	E-W compression ends pull-apart basin formation (N)NE striking sinistral faults get reactivated as dextral faults	E-W compression
Quaternary basin reactivation			NE-SW extension

Table 2: Deformation events recorded in the Vienna Basin area. Modified after Wessely (2006), Piller et al. (1996), Peresson & Decker (1997), and Lee & Wagreich (2016).

2. Methodology

The general goal of the tectonic analysis of the quarry Grossau was the quantitative assessment of the abundance and orientation of faults, fractures and rock types (fractured/unfractured dolstone and fault rock). These data together with porosity measurements from different rock types should allow an assessment of the bulk porosity of the rock mass of the exposed Hauptdolomit Fm. To achieve these objectives I applied a combination of scanline techniques to establish quantitative fault data (abundance, orientation, spacing, fault rock thickness and type), a classification of small-scale fracture density (rock mass classification by fracture density classification) and porosity measurements in the lab. Investigations were supported by thin section analyses.

2.1 Scanlines

Faults were measured along the scanlines shown in Figure 7. The orientation of each scanline (or each section of different orientation within a scanline) was measured and noted (see Figure 5).

The five horizontal scanlines have a combined length of 248.6m. For each fault encountered in the scanline, the following parameters were collected: Orientation of the fault (dip angle and dip direction), relative position on the scanline, fault rock thicknesses, visible length, types of fault rock (see the classification scheme given in chapter 0), and fault slip data (shear sense, orientation of slickenlines). If present, cross cutting relations of faults were noted. For an overview of the data minus the “visible fault length” which was in nearly all cases determined by outcrop size only see the tables in the Appendix.

Scanline 1

The 63 m long Scanline 1 is divided in 3 sections of different orientation. From north to south these are (direction of consecutive measurements): 22.7 m oriented (23-203), 18.6 m oriented (162-342) and 21.7 m oriented (128-308).



Figure 5: Strike of the first section of scanline 1, which is intersected 36 fault planes.

Scanline 2

The scanline is 44.90 m and intersected 12 fault planes. It is divided into two sections of different orientation. From east to west, these are (direction of consecutive measurements): 21.5 m oriented (20 -200) and 23.3 m oriented (62-242)).



Figure 6: The main part of scanline 2. Quarry wall is around 12m high.

Scanline 3

The 93.78 m long scanline intersected 26 fault planes and is divided in four sections of different orientation. From west to east (direction of consecutive measurements) :21.2 m oriented (88-268), 18.2 m oriented (130- 310) 18.7 m oriented (70-250) and 35.6 m oriented (60-240).

Scanline 4

Scanline 4 is 30 m long with E-W (90-270) orientation. It comprises 18 fault planes. Measurements progressed from W to E.

Scanline 5

The 17 m long scanline 5 was oriented (350-170) and intersected 8 fault planes. Measurements progressed from N to S.

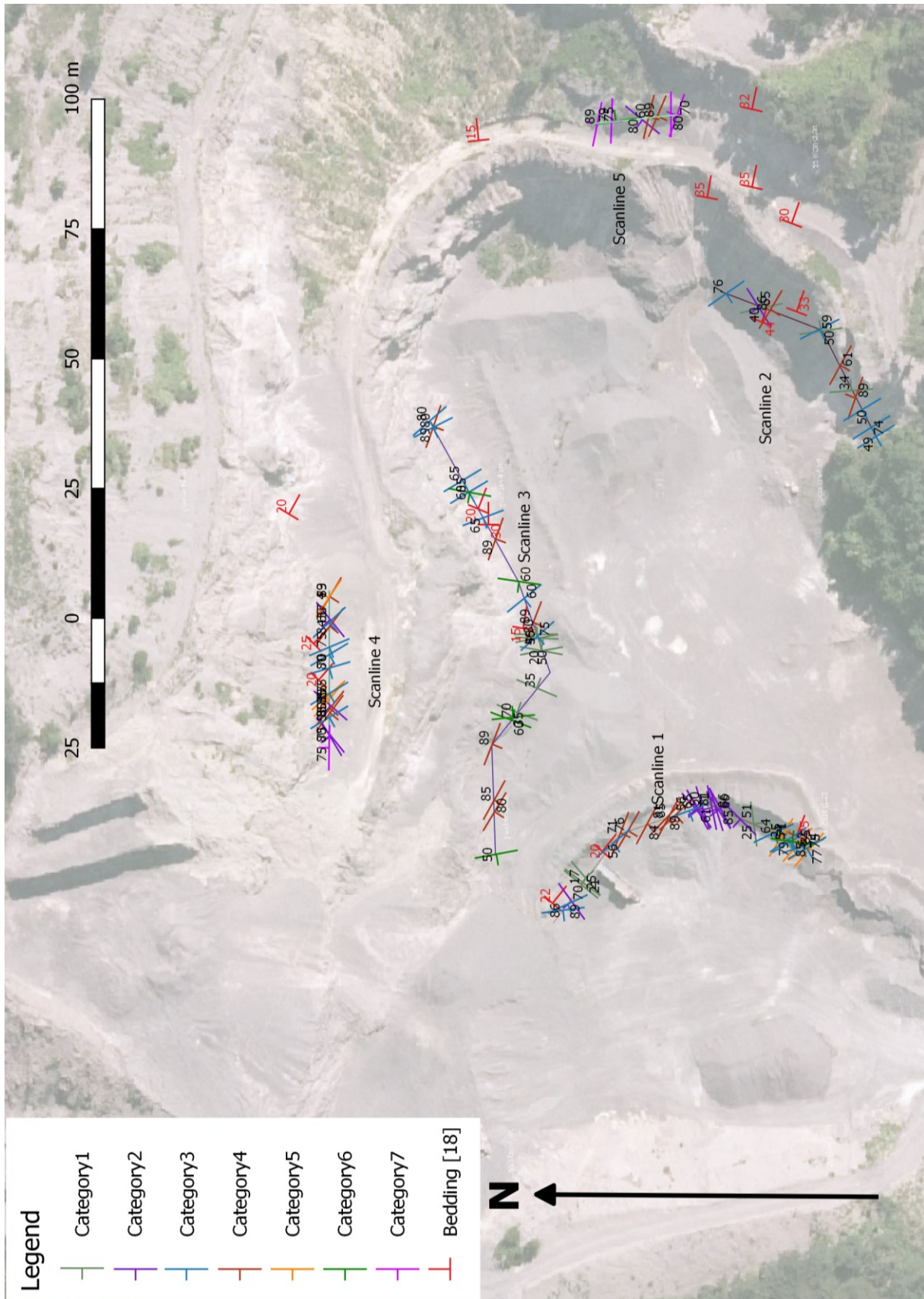


Figure 7: Overview of scanline measurements as a referenced map on an orthophoto done in Qgis. Orthophoto source: Basemap Austria.

2.2 *Assessment of fault kinematics*

I used the following shear sense criteria to determine fault kinematics (see Figure 8 for illustration, compare Petit, 1987, p.597-607):

- (1) In simple shear, Riedel planes form including 30 degrees with the shortening direction/15 degrees with the main slip surface. They show slickenlines themselves and intersect the slickenline on the main slip surface at an angle of around 90°. Antithetical Riedel shears form as conjugated set with the Riedel planes, that is at approximately 60° to them or 75° to the main fault plane.
- (2) T-Criteria: tension gashes showing no slickenlines/striations parallel to shortening direction, around 45 degrees with slickenside in simple shear. The angles given for the criteria in Figure 8 can vary between materials (different cohesion and angle of internal friction in the mohr coulomb theory) and are different for faults formed within transpressive or transtensive regimes: The angles between main fault plane, the Riedel planes and the T-criteria get bigger in transpressive and smaller in transtensive regimes as the shortening direction is more than 45° from the main fault plane in transpressive and less than that in transtensive systems.
- (3) Offset marker beds/offset of older faults and veins: when a clearly distinguishable bed/set of beds is offset along a fault this allows conclusions on shear sense. On faults with multiple reactivation on the slickensides like in Grossau however, the observed offset might be the sum of different movements. While telling us something about finite displacement it doesn't allow to come to the conclusion all the movement happening on this fault happened in one increment in the same direction along the vector defined by a slickenline we observe. Even if only one slickenline is observed it can very well be the trace of a motion that was the last of a series and erased the traces of its precursors.
- (4) Synkinematic fiber crystals grow in the direction of movement of the opposite plate.
- (5) Lunate fractures form the intersection of Riedel planes with the fault plane.

Additional faults outside of the scanlines were measured all over the quarry to get more fault slip data than the sparse information from the scanlines.



Figure 8: Some kinematic indicators used to determine shear sense on faults for this work. P-Criteria were not observed/ used. Modified from Petit et al., 1987.

2.3 Assessing fault frequency

Faults measured in the scanlines were categorized in the seven subparallel categories presented in Table 3 using Tectonics FP and sorting out clusters of poles. This was done using Pi-plots (plots showing the poles of planes in a lower hemisphere Schmidt-net plot).

All data presented here is in the form of lower hemisphere Schmidt net plots showing faults as great circles (in cases where no slickenside could be identified) or great circles with punctuation point of a slickenside on the great circle and arrows denoting shear sense where identifiable (Angelier plots).

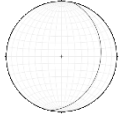
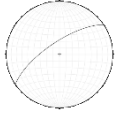
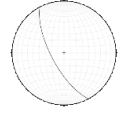
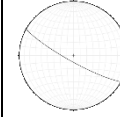
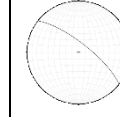
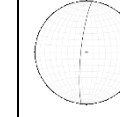
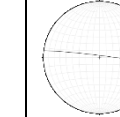
Fault orientation	Bedding parallel Dip E-SE	NE-SW striking	NW-SE striking Dip SW	WNW- ESE strik- ing Dip SW	NW strik- ing Dip NE	NS- striking	EW- striking
Fault orientation category	1	2	3	4	5	6	7
Computed average orientation							
Scanline 1	1	2	3	4	5	6	7
Faults (1 fault not assorted)	5	10	9	6	4	1	0
Scanline 2	1	2	3	4	5	6	7
Faults	3	1	5	3	0	0	0
Scanline 3	1	2	3	4	5	6	7
Faults (1 fault not assorted)	7	0	7	6	0	5	0
Scanline 4	1	2	3	4	5	6	7
Faults	0	4	6	4	3	0	1
Scanline 5	1	2	3	4	5	6	7
Faults	-	1	-	2	0	1	4
Sum: all scanlines	1	2	3	4	5	6	7
Faults (2 faults not assorted)	15	16	27	21	7	7	5
Average Orientation (EVC)	102/30	326/71	242/70	209/81	38/75	276/81	007/87

Table 3: Classification of faults according to their orientation and fault abundance in scanlines 1 to 5. EVC: average fault orientation calculated using eigenvectors (see text for further explanation).

For each category of faults, a mean orientation was computed using the eigenvector with the highest eigenvalue in Tectonics FP (which corresponds to the mean pole direction) by adding 180 to the first value and subtracting the second from 90.

Using the mean pole direction, the minimum angle α between these pole directions and the orientation of each scanline section were computed in Stereonet. Results of Stereonet were partly tested by hand plotting in the Schmidt Net.

This resulted in a 11 (scanline orientations) *7 (classes of parallel faults) matrix containing these minimum pole-scanline angles.

With these angles and the scanline distance between parallel faults the right angle distances between the individual faults and the right angle distance-aequivalent of scanline length for each of the 7 categories could be computed. The pole direction and scanline form a right-angled triangle with the scanline distance between two parallel faults being the hypotenuse, and the right-angle distance being the adjacent side relative to the angle between them (Figure 9).

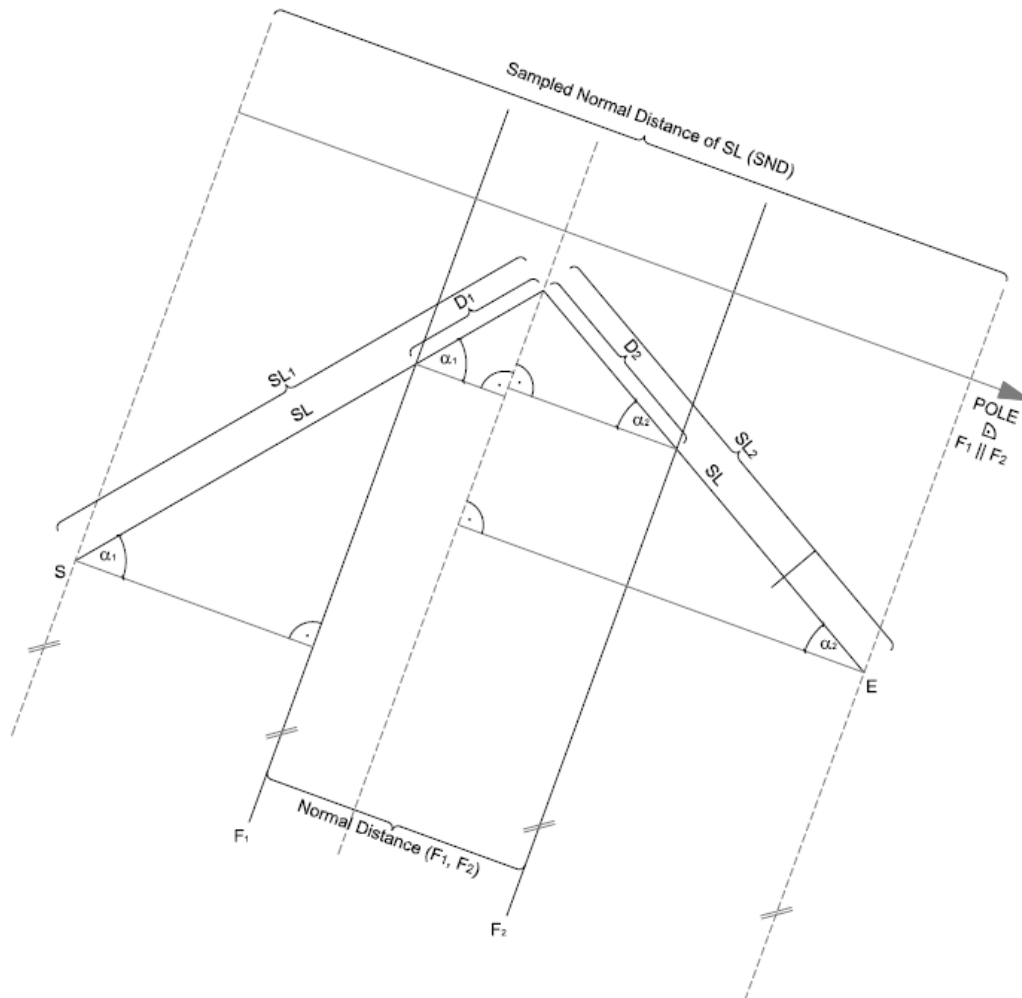


Figure 9: Calculation of standard distances between parallel faults and right-angle distance equivalents of scanline-lengths. SL is the true scanline-length. SND is the Sampled Normal Distance (the right-angle distance aequivalent) of the scanline for this set of parallel faults.

The right angle distances between faults or the “right angle distance equivalent” of the scanlines (called sampled normal distance or SND in the following text) for a certain category of faults were then computed in Excel using basic trigonometry as scanline distance* $\cos(\alpha)$. If the scanline changed direction, distances were simply added, see Figure 9. For example: calculating the right angle distance (called Normal Distance (F1, F2) in the figure above) between the two faults F1 and F2: $D1 \cdot \cos(\alpha_1) + D2 \cdot \cos(\alpha_2)$. The SND is $SL1 \cdot \cos(\alpha_1) + SL2 \cdot \cos(\alpha_2)$. (While Figure 9 shows a special case with perfectly vertical fault planes for ease of drawing, this also works with inclined planes.)

This was useful to calculate standard (right angle) distances of faults within one category of faults over different scanline orientations, to get a grip on scanline bias and for the calculation of the fault rock proportion in the scanlines as the data was acquired as faultrock true width.

Scanlines, by their mere orientation, produce a sampling bias: faults that are parallel to a section have a high probability of not being sampled; faults at approximately an angle of 90 degrees with the section have the best chance to be sampled. Simple corrections for that fact like the one from Terzaghi (Terzaghi 1965) assume evenly spaced, parallel faults or fractures. While assuming parallelism and, for the sake of projection on the pole direction, infinite fault lengths within categories here, my field data does not support the universal assumption of even distribution of fault right angle distances (for example there are faults only occurring in small corridors like those of category 7 and 2) and datasets are too small ($N \ll 32$) to mathematically test hypothesis for distributions using the z-test.). So to give an indicator for the scanline bias for each category I computed the right-angle distance sampled for each category (SND) as a percentage of the total scanline length (Table 4). The SND of each category was divided by the number of faults of the category, to give an indicator for how often they occurred in the scanlines. This should not imply that the faults of any category are necessarily normal distributed around this value. They could follow any kind of distribution in 3-D space.

It is interesting to observe though, that the arithmetic mean of the right angle distances between faults of the most common fault categories 3 and 4 calculated from actually measured distances between faults of this categories (6.33 and 7.85 m) show values quite similar to the value calculated by dividing the sampled normal distance for the category by the number of faults of the category encountered (5.56 and 8m). This could hint towards an actual even distribution of fault right angle distances around this value. For the faults of category 1, which are likely linked to the uneven distribution of Keuper layers and general bedding-related anisotropies the numbers calculated by these different approaches are far apart. (1.27m vs 5.59m). The same is true of course for the faults of category 2 which occurred only in a small corridor (7.89m vs. 0.96m). For the other categories, the sample numbers are simply too low for speculations on distribution patterns.

Fault orientation category	C1	C2	C3	C4	C5	C6	C7
No. of faults	15	16	27	21	7	7	5
Sampled Normal Distance (SND) [m]	83,81	126,28	170,91	164,90	168,23	170,15	147,36
SND [%] of total scanline length (248,6m)	33,72	50,80	68,75	66,34	67,68	68,45	59,28
SND/No. of Faults [m]	5,59	7,89	6,33	7,85	24,03	24,31	29,47
Arithmetic mean of right angle distances [m]	1,27	0,96	5,56	8,00	3,81	13,62	5,72

Table 4: Scanline bias, expressed as sampled right angle distance in % of actual scanline length and comparison between arithmetic mean of actual right angle distances and calculated mean right angle distance (sampled right angle distance divided by number of faults of category). Numbers (bold) are similar for the faults with the most samples, hinting towards and actual even distribution around this value.

2.4 Fault rock classes used for scanlines and porosity estimate

For field classification of fault rocks encountered in the scanlines I used the scheme presented in the following paragraphs. A finer classification of fault rocks like I applied it in microscopy work for chapter 4.3 would have made no sense as fault rock development actually changes within the same fault within small distances and finding enough homogeneous samples for these few categories already provided a challenge.

Fault rocks were classified as uncemented rocks, cemented breccias, cataclasites, dilation breccias and extremely fractured rock (FDC4) in fault damage zones according to the following definitions.

Uncemented fault rock (kikirite)

If rocks did not show cohesion, they were classified as uncemented fault rocks (Figure 10). Variations in grain size distribution were hard to observe as fine grain sizes were often washed out and observed grains thereby were not representative for the actual fault rock.



Figure 10: uncemented fault rocks often formed cones of washed out fault rock at their base showing a strong cohesion during dry weather.

Cataclasites

Matrix supported cohesive fault rocks of a white, chalky appearance with less than 50% eye visible protolith grains were classified as cataclasites (Figure 11). That translates into a grain size distribution with more than 50% grains smaller than 0.03 mm, so a material consisting mostly of silt and clay sized particles and less than 50% coarse silt, sand, gravel and stone sized particles.



Figure 11: Matrix supported fault rocks were classified as cataclasites for the porosity estimation.

Cemented fault breccias

Cohesive, mostly grain supported fault rocks with more than 50% eye visible protolith clasts were categorized as “cemented breccias” (Figure 12). “Eye visible” translates into particles in sizes over 0.03 mm, that is between coarse silt and stones.



Figure 12: 1 cm of cataclasite on a piece of cemented breccia: Grain supported fault rocks were classified as cemented breccias.

Dilatational breccias

Rocks, which showed a puzzle-like fit of protolith clasts within the fine-grained matrix, were classified as “dilatational breccias” (Figure 13). Their protolith clasts often showed a subrounded appearance while clearly fitting their next neighbor and so still being in situ.



Figure 13: Dilation breccia with rock fragments showing jigsaw-puzzle-like fit of protolith components separated by matrix or cement were classified as dilatational breccia.

Intensely fractured dolostone (Ifd) in faults zones

In some cases, faults or their damage zones contained rock that would not fit in any of the above categories of fault rocks but looked like the surrounding protolith, just more heavily fractured to the degree of a rock of fracture density class 4 (Figure 14). Such fault rocks were categorized as intensely fractured dolostone and treated like FDC-4 rocks in the porosity modelling.



Figure 14: Fractured rock that was clearly caused by the effects of a fault (zone) but did not fit in any of the previous fault rock categories was classified as intensely fractured dolostone.

2.5 Rock Mass classification by Fracture Density Classes (FDCs)

Structural outcrop analysis discerns between faults and fractured matrix/rock mass. The distinction is based on the scale of the structures and the development of fault rock. In the analyzed outcrops the length of small-scale fractures constituting the fractured matrix is between several centimeters and few meters with apertures in the sub-millimeter range. Faults are defined in this context as structures which significantly exceed the size (length) of the small-scale fractures constituting the fractured

matrix. In addition, faults may include new-formed fault rock (e.g., cataclasite) in the fault, intensely fractured wall rock in fault damage zones and show signs of offset between the blocks they separate.

When assessing fracture density of a rock mass along a scanline in the field in densely fractured material like the dolostones in Grossau it makes sense to categorize the rock in “fracture density classes” rather than to perform quantitative measurements, which are extremely time consuming and subjected to significant inaccuracies.

For areas with few, easily distinguished fracture sets more precise field-measurement methods would be applicable: Counting fractures, either in pictures or with software or along a scanline and measuring their apertures. An interesting approach for borehole data which could be altered for scanlines is shown by Wang (2005). This, however, is not purposeful in heavily fractured rock as it shows in the outcrop of interest. Coarse categories were decided on to mirror the average distribution of fracture densities following an example done by Decker (2007) nearby in rocks of the same formation in the quarry Gaaden near Mödling. The classification into FDCs was done by visual inspection of the fractured dolostone. Classification uses 4 classes with fracture densities (FDCs) increasing from class 1 to 4 (FDC1 to FDC4). These classes are illustrated in Figure 15.

1. FDC 1

Little to moderately jointed dolostone showing less than three sets of fractures or three to four sets of fractures with an average joint spacing bigger than 10 cm. Rocks with such fracture densities were not found in Grossau.

2. FDC 2



Closely jointed dolostone with individual joint-distances bigger than 5 and smaller than 10 cm.

3. FDC 3

Very closely jointed dolostone with joint-delimited multifaceted rock fragments with an average length from 5 to 1cm.

4. FDC 4

Extremely fractured dolostone with joint-delimited rock fragments with average sizes of less than 1cm

Fracture Density Class (FDC)	No. of joint sets	Average edge length of pieces a	Picture
1= nearly unfractured rock		a>10 cm	Not found
2	≥3	10 cm ≥ a > 5 cm	
3	(≥3) *	a=5-1cm	


Fracture Density Class (FDC)	No. of joint sets	Average edge length of pieces a	Picture
4	(≥ 3) *	a < 1cm	

Figure 15: Fracture density classes (FDCs) 1-4.

Lithostratigraphic profiles for assessing the “matrix” porosity

Profiles in sections perpendicular to bedding (sampling of as many beds as possible for their fracture density) were chosen to assess the share of these FDC’s in the “matrix” (matrix meaning: the fractured rock mass without fault rocks, compare the introduction to chapter 2.5) of the Grossau dolostone-succession.



Figure 16: Fracture density varying between individual dolostone beds as visible on the rocks in the foreground. View towards SW.

This was done based on the field observation that the variation in the dolomite and strain partitioning on siliciclastic layers (“Keuper”) exert strong control on the degree of fracturing (see the rocks in the foreground in Figure 16 and the closer look at a few beds in Figure 17. See also examples shown in Figure 87, Figure 88, Figure 89 and Figure 90 in chapter 6.1.2).

This observation got even more weight by the results of the lab measurements for porosity (see chapter 6.1) which revealed high porosity outliers belonging to easily identifiable lithofacies within the dolostone succession.



Figure 17: A closer look: Strain partitioning on Keuper bed (thin brown layer between reddish and grey beds) and bedding-controlled fracture density with FDC2 in the lower laminated bed (hammer) and FDC4 in the overlying reddish bed.



Figure 18: Locations of recorded lithostratigraphic profiles. The short profile in the eastern part of the quarry exposes part of the dolostone succession on top of the section recorded in the long profile along the northern quarry walls.

The true thickness of beds, their respective FDC and their lithology with regard to the dolostone facies types with exceptionally high effective porosity were noted along the lines shown in Figure 18. These were chosen to sample as many different clear distinguishable beds as possible.

Parts of the outcrop near big faults were excluded for these profiles. The stratigraphic sections have a combined length of 42 m (perpendicular to the bedding). For the full data see Table 14 in the Appendix

2.6 Lab determination of open porosity and bulk density for dolomite FDCs and cohesive fault rocks

For the measuring and calculation, a method based on ÖNORM B 3121 and ÖNORM EN 1936 was used. Accordingly, the samples were dried in an oven and weighed until mass stayed constant within 0.1 %. Samples were then two times submerged in water for a minimum of 24 hours – first partly, then total to guarantee complete saturation of the samples. The wet samples were weighed, one time in air and onetime submerged in water, again with a maximum error of 0.1% allowed between each pair of measurements.

Open porosity:

$$po = \frac{100 * (ms - md)}{(ms - mh)} [\%]$$

Bulk density:

$$\rho b = \frac{(md * \rho rh)}{(ms - mh)} [g/cm^3]$$

po ... Open porosity [%]

ρb ... Bulk density [g/cm^3]

md ... Dry mass of sample [g]

ms ... Mass of saturated sample in air [g]

mh ... Mass of sample submerged in water [g]

(ρrh ... Density of Water =1 [g/cm^3])

Samples that were processed in the lab weighed between 2 and 4 kilos with an average around 2 kilos. This specimen size was necessary to sample a representative amount of the fractures in the rock volume for FDC 3 and 4: Samples with about 2 kilos roughly correspond to a cube of around 9 cm edge length of solid dolomite with a density of 2.85 [g/cm^3]. With a defined average spacing of fractures of 10 to 5 cm for FDC 2 the workable sample size is too small to catch a relevant amount of the fracture porosity of this class. The values for FDC 2 rather gives us an idea of matrix porosity and thereby underestimates total porosity. The same is still true for FDC3, but to a lower extent. Another sampling problem is sample stability: The less fractures and the better cemented the fractures in a sample are (i.e., the lower the fracture porosity), the higher is the chance for a sample to survive hammer-and chisel sampling plus transport in the back bag. Even if it makes it to the lab, the porosity measurements include repeated, yet careful, heating, cooling and water saturation, which again is very likely to cause strongly fractured and weakly cemented rocks of high porosity not to survive the process.

2.7 *Sample collection*

While samples for porosity measurements were also collected from loose talus, samples for thin section preparation were all taken directly from hardrock-outcrops. Whenever possible, samples were taken oriented as shown in Figure 19: Dip angle and Dip direction of slickensides and slickenlines were noted on the specimen together with noting as was whether they belonged to the foot- or hanging wall, the eastern, western, northern or southern wall of the fault. Photos and sometimes drawings of the sample position were made for further documentation in most cases.



Figure 19: Careful removal of oriented sample using a set of flat wedges (sample 5.2).

Samples from fault rocks and matrix for porosity measurements were collected parallel to drawing and photographing faults, fault rocks and structures.

2.8 Methodology of thin section preparation

Thin sections were first looked at and described directly after preparation, which involved vacuum treatment with blue coloured resin to get an idea of the distribution of porosity (which could potentially be unobservable after the second step of colouring). Thin sections then were etched with diluted hydrochloric acid and coloured with sodium alizarin sulfonate and potassium hexacyanoferrate (III) to be able to observe differences in Fe respectively Mg content in the matrix/cement and protolith composition (compare Ney, 1986) with no useful results because the resin used to colour and stabilize the rocks in the step before, took colour as well.

Matrix/protolith ratios in the fault rocks were estimated with comparison pictures from Flügel (1978, p. 161), in strongly zoned samples values were given for each zone.

While for the field description of fault rocks the simple categorization explained in chapter 0 proved useful, the microscopical work allows for finer description and the nomenclature by Billi (2010), which was developed for the microscopical description of carbonate fault rocks, was used.

Oriented fault rock sections were prepared by slicing the rock perpendicular to the fault plane and parallel to the (most prominent) slickenline. Care was taken to re-check orientation of section after preparation in the lab by comparison with the remaining blocks/samples. All orientation data is given in the form of dip direction/dip angle.

3. Faults in the quarry Grossau

The fault orientation categories introduced in chapter 2.3 were mostly assigned to guarantee sub-parallelism of faults for the calculation of right angle distances used in chapter 4 for describing the characteristics of the rock mass with respect to the abundance and orientation of faults, small-scale fractures and bedding planes. Under the assumption that parallel faults are mostly, but not always also genetically linked (with other words: result from the same stress field that caused brittle failure in their orientation) faults measured in the scanlines were compared with fault slip data from measurements all over the quarry and interpreted in the context of literature on the regional deformation history as outlined in chapter 1.1.

In the following figures showing lower hemisphere Schmidt net plots the graph on the left shows the planes assorted to a category in the scanlines for the computing of the right angle distance, with other words faults with similar orientation/poles plotting in a cluster. Graphs on the right show fault-slip data collected all over the quarry associated with that category that could give some insight in the kinematics and history of the faults in the category when compared with literature on the tectonic history.

3.1 Category 1: SE-E dipping flats and ramps

All over the quarry faulting on bedding-parallel, E- to SE-dipping flats and connected, mostly E- to ENE-dipping ramps can be observed (Figure 20 to Figure 23). Structures include mirror-like polished bedding planes with slickenlines beneath siliciclastic layers, duplexes and a massive bedding parallel fault rock cropping out in the east wall of the quarry with more than 2m apparent thickness (see Figure 23).

ALLS0par.pln
Datasets: 15

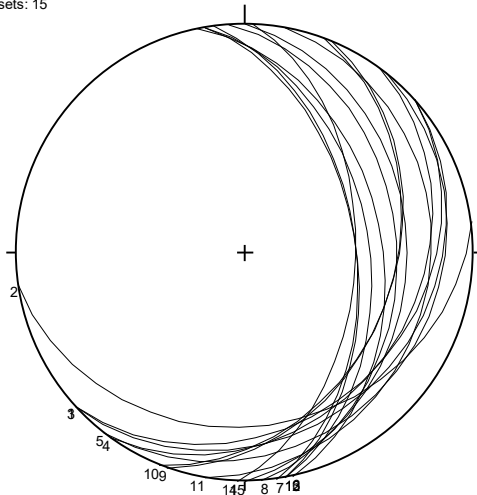


Figure 20: Faults sampled in the scanlines assorted to category 1.

RampenausRandommessung.cor
Harnische auf S0 ohne7.cor

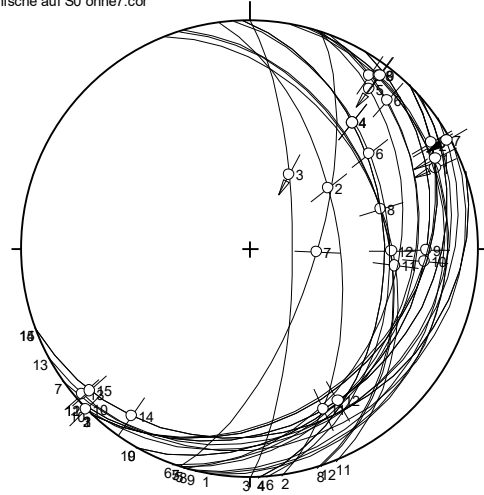


Figure 21: Slickenlines and shear sense data of faults fitting category 1 measured all over the quarry.

With the bedding dipping relatively homogeneously towards the SE, the genesis of the flats can relatively safely be attributed to the NW-SE compression in D0 and D1. While most of the flats dip to the SE, the ramps show a tendency to dip E to ENE. At the absence of shear sense criteria, the formation of duplexes could be interpreted to indicate thrusting, as a stacking of material is only rarely attributed to normal faulting for space-reasons. However, extensional duplexes (compare Root, 1990) are an actual alternative explanation for the duplex depicted in Figure 22.



Figure 22: Structures interpreted as duplexes here with reverse faulting as the assumed process. Compare with the plot of all faults associated with this category and with the lineaments measured on faults all over the quarry.

Normal faulting to the east seems the more likely explanation in the western vicinity of the Vienna basin. The three types of slickenlines found on this faults point towards multiple reactivation, which could have been NW directed thrusting during D0/ D1, nearly strike-parallel, likely sinistral movements during D3 and E-directed normal faulting towards the Vienna basin during D4 or W directed thrusting during D5. The NW-trending slickenlines plotting exactly at the intersection of flats and ramps are likely younger than those and could result from gliding of the blocks parallel to the intersection.



Figure 23: Bedding parallel fault rock with cataclasite of more than 2m apparent thickness in the eastern quarry wall (white next to measuring stick). View to N.

Bedding-parallel fault-rocks of the flats could be observed to be offset by younger faults of category 5 (Figure 32) with an apparent offset between half a meter and up to 5 meters.

Considering the difficulty in spotting faults subparallel to the bedding in a rather homogenous lithology and the fact that this fault category is most affected by scanline bias these faults are still relatively abundant.

Concerning sampling it was interesting that no faults of this type were encountered in scanlines 4 and 5, which are on the second level of the quarry in rocks generally more exposed to weathering/the influence of water. Bigger faults of this kind could be observed in the higher/more weathered levels but outside the range of the scanlines. It therefore seems that small slickensides are obscured by weathering. Especially bedding planes, visible as “planes of separation” are harder to distinguish from fault planes paralleling bedding planes with increasing weathering.

3.2 Category 2: Steeply dipping NE-SW striking faults

These generally NW dipping faults (Figure 24, Figure 25) form a corridor of about 6m true width in the lowermost wall of the quarry (see Figure 7) sampled by scanline 1. Parallel faults rarely show up elsewhere in the scanlines. This could be attributed to scanline-bias, as a huge part of the scanlines is oriented sub-parallel to the strike of the SW striking faults as visible from the map in Figure 7.

Category2.pln
Datasets: 16

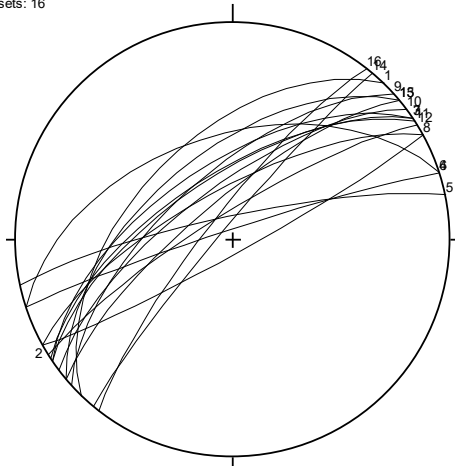


Figure 24: Faults sampled in the scanlines assorted in category 2.

Category2.cor
Datasets: 4

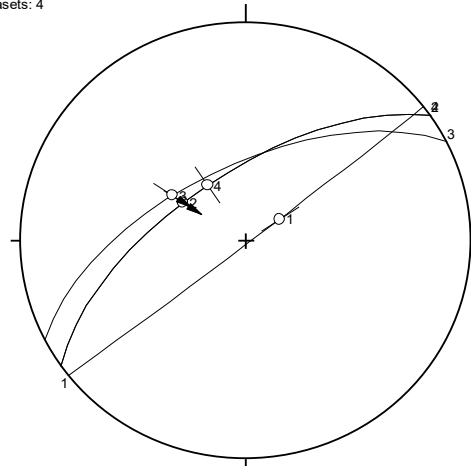


Figure 25: Slickenlines and shear sense data of faults fitting category 2 measured all over the quarry

In the uppermost level of the quarry, two faults parallel to the orientation of this group allowed measurements of slickenlines and showed clear shear sense indicators indicating reverse faulting (Figure 26).

Overstepping, NE striking sinistral strike slip faults are responsible for the nearby Vienna Basin, but these faults and the margin of the Vienna basin rather strike N- NNE near Vöslau according to tectonic maps (e.g., Piller et al. 1996, p. 9).



Figure 26: Synkinematic fiber crystals on the footwall of a fault oriented 333/62 with a slickenside 302/59 indicating reverse faulting (view direction SE).

3.3 Category 3: NNW-SSE striking faults

Slickenlines on the steeper dipping faults of this class strike and dip mostly NNW (Figure 27, Figure 28). Shear sense indicators were sparse and contradictory indicating both dextral and sinistral shear on the steeper faults. Interpretations on samples 5.2 and 7.2, which derive from faults fitting the steeper members of this category indicate sinistral shear but evidence is only robust in the case of sample 7.2. The faults dipping with around 60 degrees to the SW show a dip-slip slickenline in two cases, which shows a striking parallelism to some of the NE-SW-directed slickenlines on faults of category 1.

Category3.pln
Datasets: 27

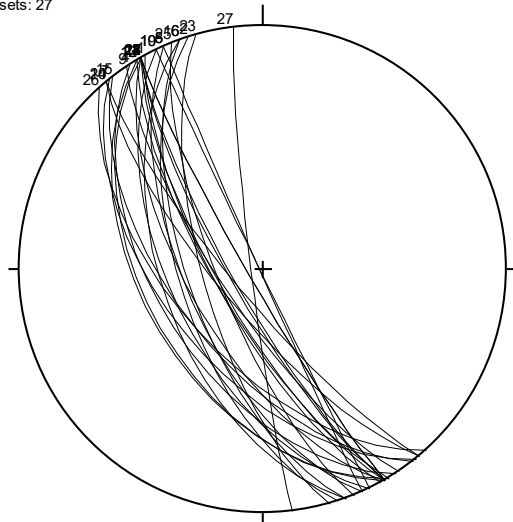


Figure 27: Faults sampled in the scan-lines assorted in category 3.

Category3.cor
Datasets: 11

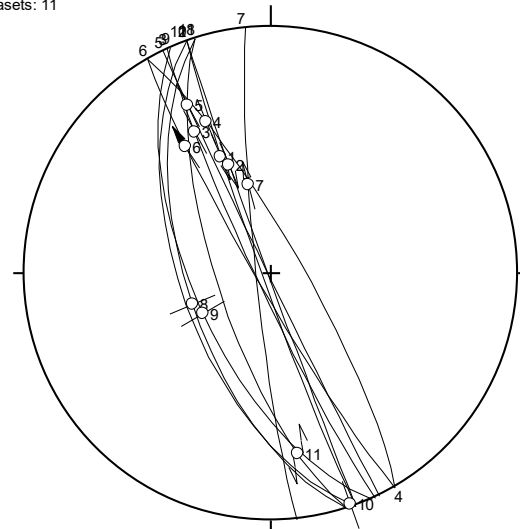


Figure 28: Slickenlines and shear sense data of faults fitting category 3 found all over the quarry.

These slickenlines could be attributed to NE-SW compression in D3, an interpretation aided by the observation of a nearly fault-plane parallel stylolite in sample 7.2 indicating that the fault rock of a preexisting fault was affected by compression nearly perpendicular to its strike direction.

One of these faults, showing a strike slip slickenline and weak indicators for sinistral shear, is offset by normal faulting at a fault of category 5, proving that it is older than the faults (or at least the last reactivation of the faults) of category 5 (see Figure 29).

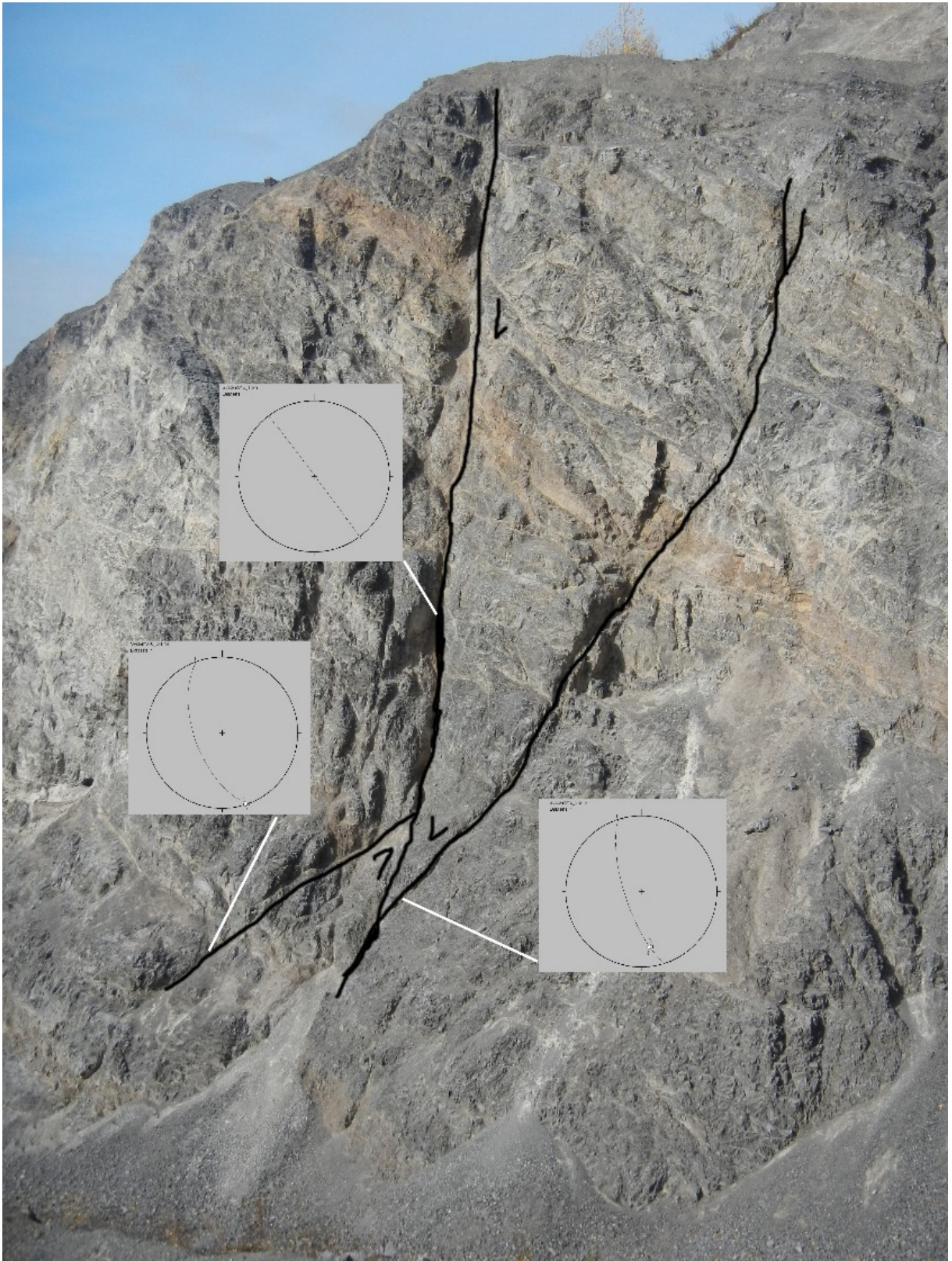


Figure 29: Typical fault of category 3 offset by one of the steeper faults of category 5. Quarry wall approx. 12m. View towards NW.

3.4 Category 5: NE-dipping normal faults

Faults of this category (Figure 30, Figure 31) offset marker beds, flats from category 1 and faults of category 3 (Figure 32 to Figure 34). NE-directed normal faulting in the direction parallel to the general dip direction of the faults is observed on scales from 0.3m to about 5m apparent offset. Most of the faults contain uncemented fault rocks and no slickenlines. In the few (three) cases where slickenlines on cemented faultrock were found on faults fitting this category, fault slip data indicates NE-directed normal faulting, which, as a general direction is surely also true for the faults with uncemented fault rock though they are likely of a younger age.

Category5.pln
Datasets: 7

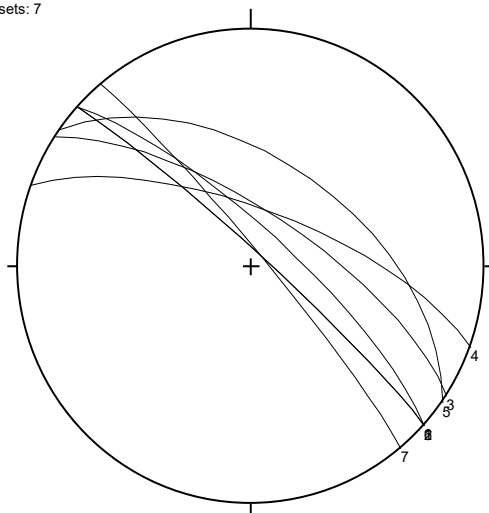


Figure 30: Category 5 faults from the scanlines

Category5.cor
Datasets: 3

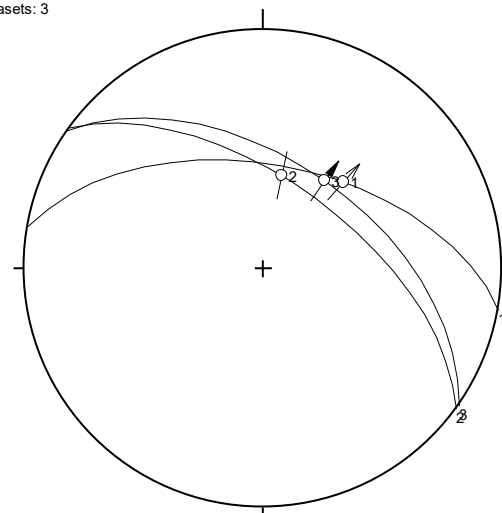


Figure 31: Slickenlines on category 5 faults

Decker et al. (2005, p. 312) describe NE-SW extension on NW trending normal faults, but from the northern side of the basin, from Kutý-Dobruška area of Slovakia and the Czech Morava Graben near Olomouc. Cross cutting relations constrained the age of these faults to Pliocene to Quaternary. The faults are crosscut by active faults, but offset Miocene NE-striking faults of the Vienna basin (Salcher et al., 2012, Decker et al., 2005).



Figure 32: NE dipping normal faults offsetting marker beds and flats of category 1 faults in the south-eastern quarry walls. Height of wall = 30 m, view towards SE.



Figure 33: A category 5 normal-fault offsetting red marker beds divided by a category 1 flat



Figure 34: A category 1 flat offset by a category 5 normal fault

3.5 Category 6: steeply dipping NS-striking faults

The sparse fault slip data on steep N-S striking faults (Figure 35, Figure 36) shows slickenlines parallel to those found on the faults of category 1 for the ones dipping to the E, but they are too steep to belong to the ramps, so this is likely a reactivation. The slickenlines on the west dipping faults of the category resemble those of category 3 faults.

Category6.pln
Datasets: 7

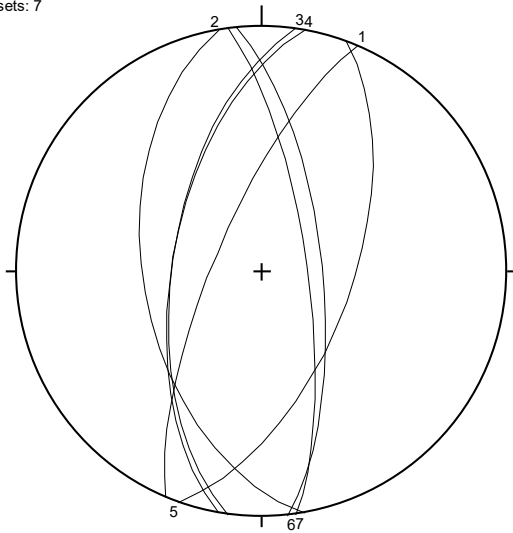


Figure 35: N-S striking faults encountered in the scanlines and grouped in category 6.

Category 6.cor
Datasets: 5

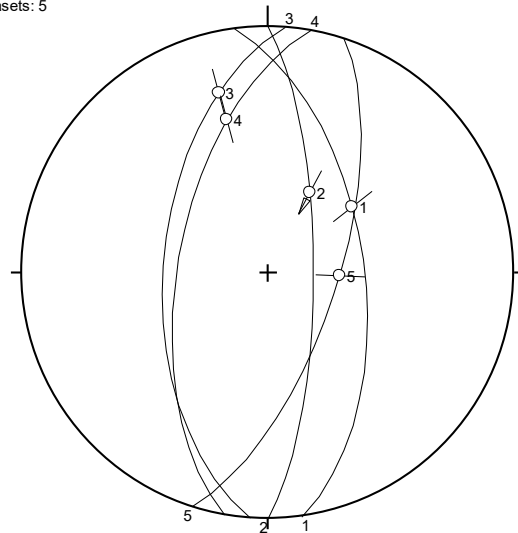


Figure 36: Slickenlines on faults of category 6 resemble those on some category 1 faults (slickenline 1 and 2) and such found on category 3 faults (slickenlines 3 and 4).

3.6 Category 7: E-W striking faults

Steep EW-striking faults only occur in scanline 5 and scanline 4 (one fault). The few shear sense for the south dipping faults of this category were acquired from a fault outside of the scanlines (Figure 37, Figure 38).

Category7.pln
Datasets: 5

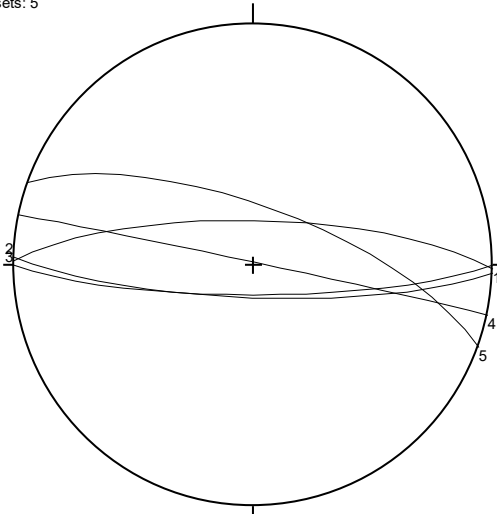


Figure 37: EW-striking faults encountered in the scanlines were grouped in category 7.

Category7.cor
Datasets: 5

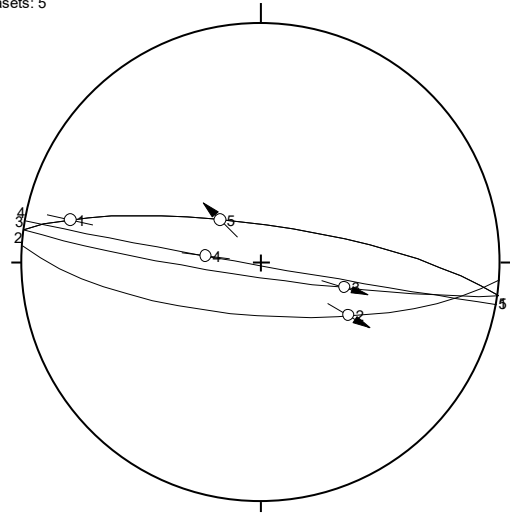


Figure 38: Kinematic indicators found on EW striking faults indicating NW-SE extension.

They stem from the biggest steep fault in the quarry, cropping out in the NE- corner of the second level and showing more than one m of well-developed fine grained cataclastic fault rock (Figure 39).

For one north-dipping fault of this category normal faulting could be proved by a combination of field observations and thin section data (sample 2, chapter 5.1.2). The few datasets with shear sense data for the category indicate that NW-SE-directed extension produced the slickenlines in question. The steep faults though have likely an origin as strike slip faults.

Wessely interpreted the slickenline indicating NW-SE extension at the Harzberg fault above Vöslau as normal faulting towards the Gainfarn Basin ("Gainfarn Bucht"; Wessely et al., 2007, p. 428). Schopper interprets this normal faulting to be associated with the formation of the Berndorf Basin (Schopper, 1991, p. 125). These slickenlines could be the traces of the same event in a parallel oriented fault 2.5 kilometers to the W. Middle Miocene NW-SE extension (D3) is generally observed east of the bohemian basement spur (Peresson & Decker 1997, p. 153).



Figure 39: Apparently E-W striking fault system showing well developed fault rock, steep slickenlines and lunate fractures indicating downwards slip of the (missing) hanging wall. View towards ENE.

3.7 Tension gashes

Dolomite-filled tension gashes are relatively rare and well cemented with sparitic dolomite (Figure 40). The structures therefore do not carry significant porosity. Tension gashes are strikingly parallel wherever measured pointing to an origin in a common stress field with NW-directed extension.

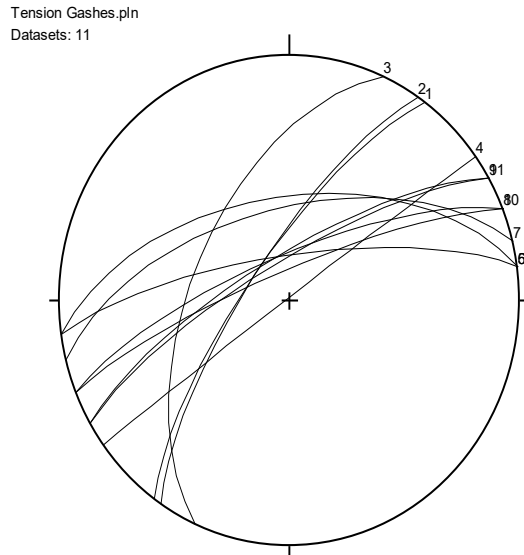


Figure 40: Tension gashes measured all over the quarry

Although often a little sigmoidal (compare Figure 41) the axis connecting their tips is oriented more or less at a right angle with the bedding.

The average computed orientation (329/71) of the 11 measured tension gashes encloses an angle of 88.5° with the average computed orientation of the bedding (127/22) from 27 data.

Tension gashes therefore may have formed in the hinge zone of (fault-bend) folds during NW-directed compression in deformation D0/ D1. Formation during NE-SW-directed compression in D3 appears less likely and would not explain the observed orientation at right angles to the bedding planes.



Figure 41: Subparallel tension gashes at right angles to the bedding. Observe also varying fracture density between beds.

4. Quantitative assessment of the anisotropy of the rock mass

The scanlines and the porosity profile done mainly for purpose of the porosity estimate also yielded information about the distribution of discontinuities in the rock mass like bedding planes and faults within the rock mass. This information could be useful in explaining directional anisotropies (e.g. concerning permeability) of the rock mass.

4.1 Spatial distribution of discontinuities of sedimentary origin (bedding and siliciclastic layers)

Measured bed thicknesses of dolostones varied between a few centimeters and around 6 meters (Table 5). Layers of fine-grained siliciclastic sediments (“Keuper”) intersect the dolomite at irregular intervals. Only six undisturbed true distances between “Keuper” beds could be measured. These varied between 28cm and 5.92m. One distance between a Keuper bed to the end of an undisturbed profile was larger than this maximum with 8.89 m, indicating still larger distances are possible. The Keuper intercalations are usually detachment horizons (faults of category 1) with dolomite rocks showing polished slickensides underneath the siliciclastic layers. The layers therefore cannot be regarded as undisturbed beds. The siliciclastic layers are mostly not continuous as they are intersected and offset by a multitude of faults. They are therefore not likely to act as seals.

It is likely that flats of faults of category 1 with bigger offset and thicker fault rock have developed along such Keuper beds and worked them up in the process.

Bed thickness of dolostone beds [m] (N= 46)	
Max	6.20
Min	0.12
Arithmetic Mean	0.91
Bed thickness of siliciclastic layers (Keuper) [m] (N=10)	
Max	0.009
Min	0.001
Arithmetic Mean	0.005
True Distance between siliciclastic layers [m] (N=6)	
Min	0.28
Max	5.92
Arithmetic Mean	1.81
Max. Distance without Keuper	8,89

Table 5: Discontinuities of sedimentary origin

4.2 *Spatial distribution of faults and fault rocks*

The percentage of contribution to the total fault rock volume was calculated from the percentages of fault rock in the sampled normal distance (the right angle distance equivalent of the total scanline length) of each group of parallel faults (Table 6). This was done under the assumption that the share of the true thickness of fault rock in the SND provides a value-correction for scanline bias. Any additive or subtractive relationships faults crosscutting each other might have were ignored as they could not be observed in the field.

NW striking and SW dipping faults of category 3 and category 4 were the most abundant in numbers and fault-rock percentage in the scanlines. Wherever they occur, they intersect the entire outcrop proving fault length in excess of 12 m. Karstic cavities visible in the northern quarry wall are also likely connected to these faults and point towards a higher permeability of the rock mass in their strike-direction.

Uncemented fault rocks at normal faults of category 5, which also strike NW, further enhance the permeability in NW-SE direction.

While faults of category 3 and 4 show the highest proportion of cemented fault rocks with high porosity and low permeability in the scanlines it seems unlikely that they would act as seals. The cemented fault rocks appear to be affected and bypassed by open younger fractures and uncemented faults wherever they crop out.

The high fault rock percentage of the category 2 faults, which only show up in a small corridor in scanline 1, is due to a single observation of one more than 1m thick fault rock and therefore should not be over interpreted. Faults of category 1 are likely to be more important, especially as the flats were often hard to spot and distinguish from bedding planes in places where the rocks showed more intense weathering like in the scanlines 4 and 5 in the second level of the quarry. Category 1 is also the fault category most strongly underrepresented due to scanline bias (compare Table 4). The faults of category 1 intersected by the scanlines hardly showed cemented fault rocks. Instead, crumbly but cohesive fault rock with up to around one meter true thickness could be observed.

Faults of the categories 6 and 7 are too few in number within the scanlines to speculate on their relevance. A steep, apparently E-W striking fault system in the northeast corner of the second level of the quarry should be mentioned though: The fault is visible on the outcrop scale and as a white trace in historical orthophotos of the quarry accessible over NÖGIS (accessed in 2017). It shows mature cataclasite of more than a meter true thickness and a damage zone with a minimum thickness of 2m affecting the whole visible outcrop (compare Figure 39).

Category	C1	C2	C3	C4	C5	C6	C7
No. of faults	15,00	16,00	27,00	21,00	7,00	7,00	5,00
Fault Rock Total [cm] in all scan-lines	45,00	157,00	472,00	303,70	23,00	59,00	15,50
% contribution to total fault rock volume (calculated from scanline-direction-corrected share in total rock, not from apparent value in the row above!)	7,70	17,82	39,58	26,40	2,03	4,97	1,51
Sampled Normal Distance [m]	83,81	126,28	170,91	164,90	168,23	170,15	147,36
SND/No. of Faults [m]	5,59	7,89	6,33	7,85	24,03	24,31	29,47
Meas. true distance Min. [m]	0,22	0,13	0,50	0,43	0,38	0,15	1,27
Meas. true distance Max. [m]	10,49	28,94	16,63	21,16	11,17	25,82	11,68
Meas. true distance A. Mean [m]	1,27	0,96	5,56	8,00	3,81	13,62	5,72

Table 6: Distribution of faults and fault rock in the rock mass.

4.3 Category 4: WNW-ESE striking faults

The steep faults are oriented parallel to the prominent strike of the Merkenstein Fault System, which gradually changes from an EW-directed strike near the Vienna Basin to WNW-ESE-directed strike further W (Figure 42, Figure 43). The faults could be interpreted as belonging to D1 and being equivalents of post-Eocene dextral WNW-striking faults like the Wolfgangsee-, Windischgarsten - and Hochwart Fault (compare Peresson & Decker, 1997).

Category4.pln
Datasets: 21

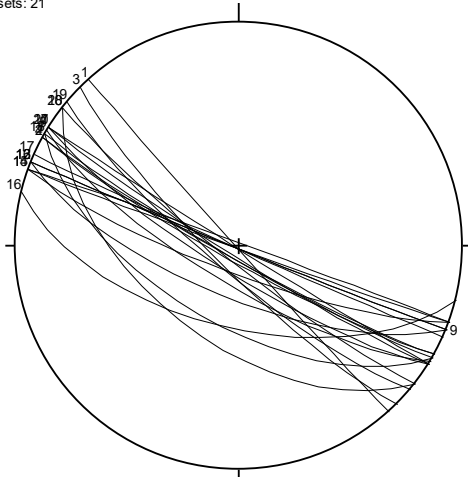


Figure 42: Faults from the scanlines assorted to category 4

Category4.cor
Datasets: 14

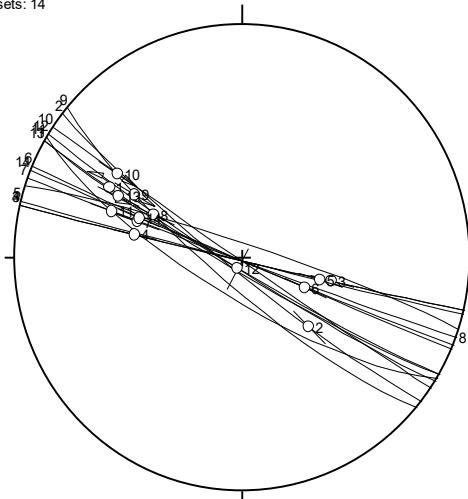


Figure 43: Slickenlines found on faults fitting category 4.

I could observe weak sinistral shear sense indicators in the field in three cases as well as signs for multiple reactivation with up to three slickenlines on the same fault. Observations on samples 3 and 10 (see chapter 5.1.3 and 5.1.6) give additional weight to this observation. Wessely et al. (2007, p. 428) as well observed sinistral shear on the Merkenstein Fault. Peresson & Decker (1997, p. 154) observed sinistral reactivation of the dextral D1 faults during E-directed compression during deformation D5 and it seems likely that the indicators for the youngest movements are the ones that are best preserved / observed.

5. Fault Rocks in Grossau

5.1 Thin section and sample descriptions

In my opinion, to be of any meaning, observations on thin sections need context from the sample and outcrop. This also is a preventive measure against errors with oriented samples. As a result, thin sections are described here parallel with the remains of the samples, and – if this helps to prove a point – with the information/pictures of the outcrop they stemmed from. Some samples were lost either due to vandalism during storage in the quarry or destroyed during transport and preparation. To have a consistent system with my fieldnotes I decided to keep the numbers (Table 7). Samples 5.2 and 7.2 were resampled at the same locations/fault after destruction of sample 5 and 7 respectively. The fault-rock terminology used in microscopy work is based on the system from Billi (2010) outlined in chapter 5.2.3 below within a general discussion of fault rock classification systems based on my experiences with the fault rocks of Grossau.

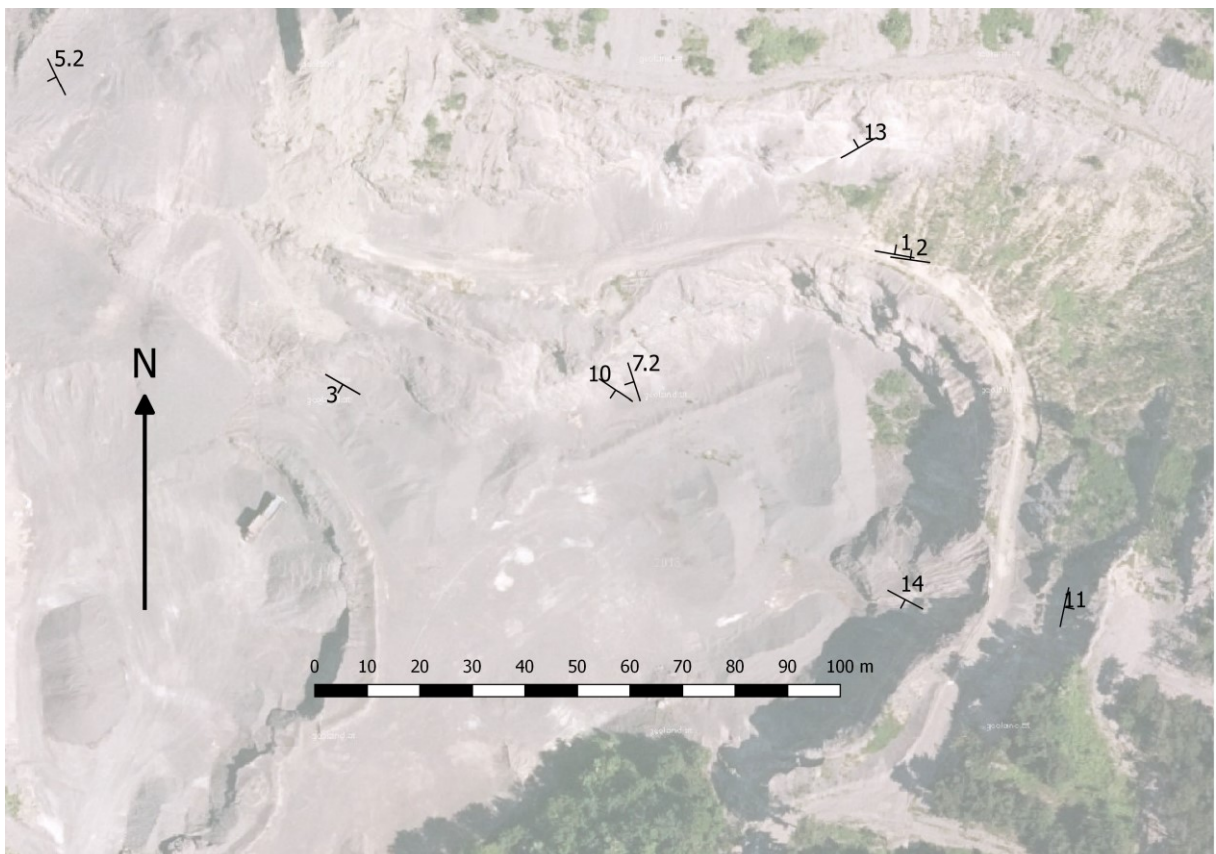


Figure 44: Locations of samples given with the symbol indicating the strike and dip of the faults they stem from. Dip angles given in Table 7.

Sample No.	Dip Direction of Fault	Dip Angle of Fault	Fault Category	Remarks
1	010	54	5	Categorized in 5 because of NW directed normal faulting
2	008	77	7	
3	210	86	4	
5.2	244	89	3	
7.2	252	75	3	
10	214	89	4	
11	(102)	(32)	1	Bedding parallel fault rock. Orientation data from nearest bedding measurement.
13	330*	80*		Orientation of sample slickenside and fault system likely EW
14	208	70		

Table 7: Fault rock samples, the orientation and categorization faults they stem from. Orientation values for sample 11 are from the nearest bedding measurements as sample had to be hammered out overhead and the bedding parallel fault couldn't be measured. Sample 13 stems from a fault system of unclear main orientation with multiple meandering slickensides. The orientation data are the ones of the main plane on the sample.

5.1.1 Sample 1

Macroscopic Description, Orientation of sample and thin sections

Sample 1 (Figure 45) is a piece from the footwall of a fault of category 7 with the orientation 010/54 showing a slickenline of 040/45. It was cut perpendicular to this plane and parallel to its slickenline to prepare a panorama" section and a smaller one. The sample seems to consist macroscopically of around 2 cm of mature cataclasite on fractured dolomite matrix.



Figure 45: Sample 1 viewed in the orientation of sections.

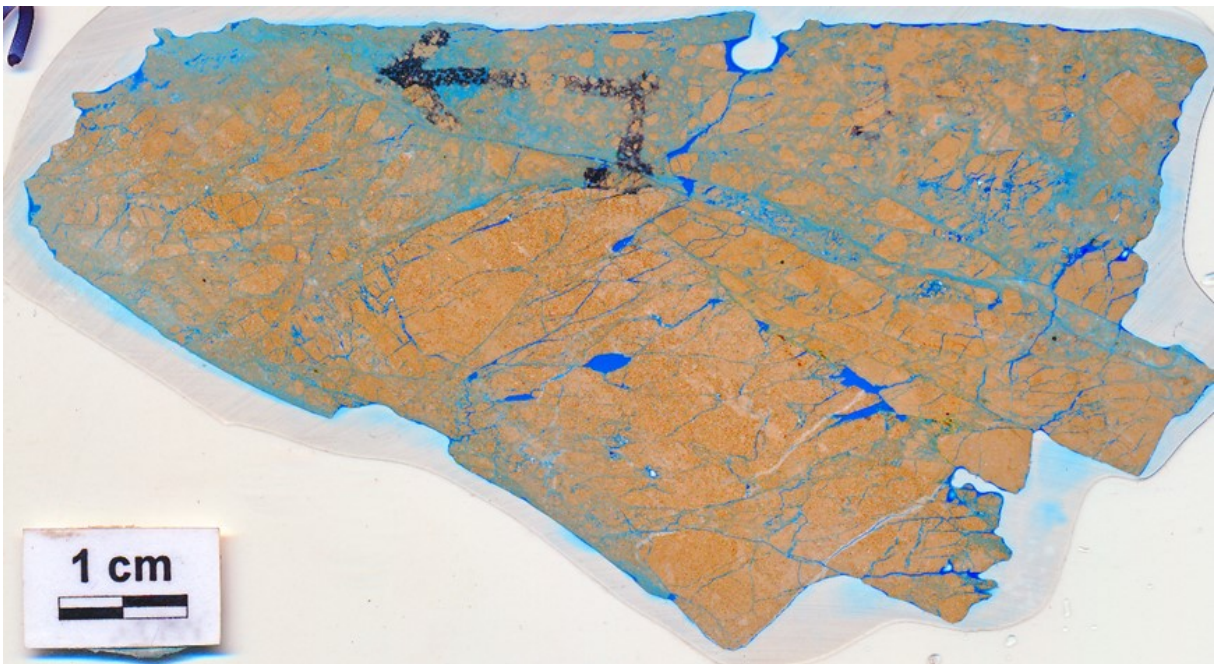


Figure 46: Panorama section of sample 1 in a scan with artificially enhanced saturation. Dark blue color is the stained resin highlighting open pores and fractures, cataclastic material with varying porosity due to smaller (microscopic) pores appears in shades of paler blues. Long arrow points towards the dip direction of the slickenline, section is parallel to the slickenline and perpendicular to the fault plane.

Zoning

The panorama section and the cut sample can be separated in two zones: intact, but heavily fractured dolomite makes up around 2/3 away from the slickenside, 1/3 is intermediate to mature cataclasite with a few subangular grains in it.

Microscopic description

Apart from the first 2 mm adjacent to the principal slip surface (in the following text: PSS) most of what appears as “matrix” macroscopically consists of protolith grains of 0.05 to 0.1 mm size thereby giving a lower matrix estimate than the macroscopic impression of this layer would indicate.

The first two mm near the PSS however are mostly made up of grains smaller than the resolution of the light microscope. Still they contain eye-visible protolith clasts. In the left part of the panorama section, and in the small section, elongated pieces with preferential fracturing perpendicular to their long axis are observed.

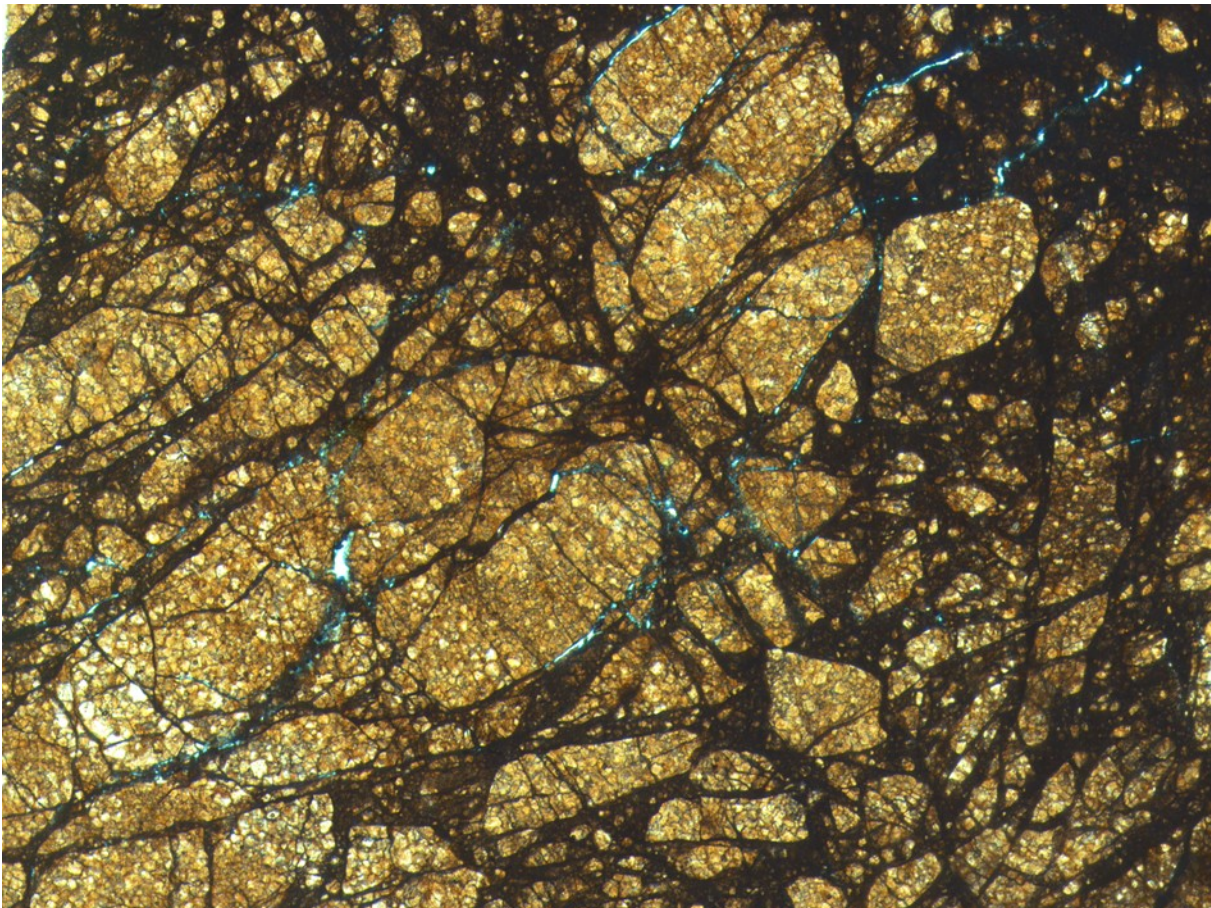


Figure 47: Elongated grains shaped by extension fractures at 45° to the fault plane showing preferential fracturing perpendicular to their long axis. Scan from section 1 with artificially enhanced saturation. Fine cataclastic material appears dark in these scans. Note rounding of more or less in-situ grains without signs of rotation. Picture width = 1 cm.

Shear-sense indicators observed in sample and thin section

In the field, a T-criterion indicating normal faulting could be observed. A fault intersecting the main fault plane at an angle of 15 to 20 degrees is well visible in the thin section and shows a slip surface with a slickenline roughly on the plane of the section as seen in the remains of the sample. This would indicate reverse faulting if interpreted as R-plane.

As typical faults of this orientation show obvious normal faulting on marker beds (see description of fault category 5) the field observation on the T-Criterion seems more trustworthy. Most of the obvious normal faults did not show cemented fault rock however.

Matrix/protolith ratio

The whole piece is around 2/3 protolith and 1/3 fine cataclastic matrix, the latter mostly to be found in the PSS and the fault transecting the piece mentioned above.

Protolith grain shape and orientation

Towards the PSS rounding of protolith grains increases from angular over sub-rounded to rounded pieces. Elongated grains with preferential fracturing along their long axis are observed in two sections prepared from the sample. They tend to be oriented at 45° to the PSS, so in the orientation of the T-criteria with their long axis. The elongated grains, while in situ, show rounded grain shapes (Figure 47).

Distribution and carriers of porosity in the sample

Porosity is found in the abundant open fractures. These connective open fractures show opening widths in the sub mm range and show a preferred orientation of around 25° to the fault plane in the panorama section (Figure 46). Porosity also shows in pores in the cataclastic material, which are smaller than the resolution capability of the light microscope.

Other Observations

In some of the ultracataclastic parts, but also in fractures dendritic rusty-brown bodies were observed. These might be Fe or Mn precipitates from fluids penetrating the rock or the remains of surface oxidized pyrite.

5.1.2 Sample 2

Macroscopic description, orientation of sample and thin section

Sample 2 is a 3cm wide piece consisting entirely of intermediate cataclasite (Figure 48) from a fault matching Category 7, dipping 008/77. It was cut perpendicular to this slickenside and parallel to the dominant slickenline (328/65) to make the thin section. The plane used for marking belonged to the hanging wall of the fault.

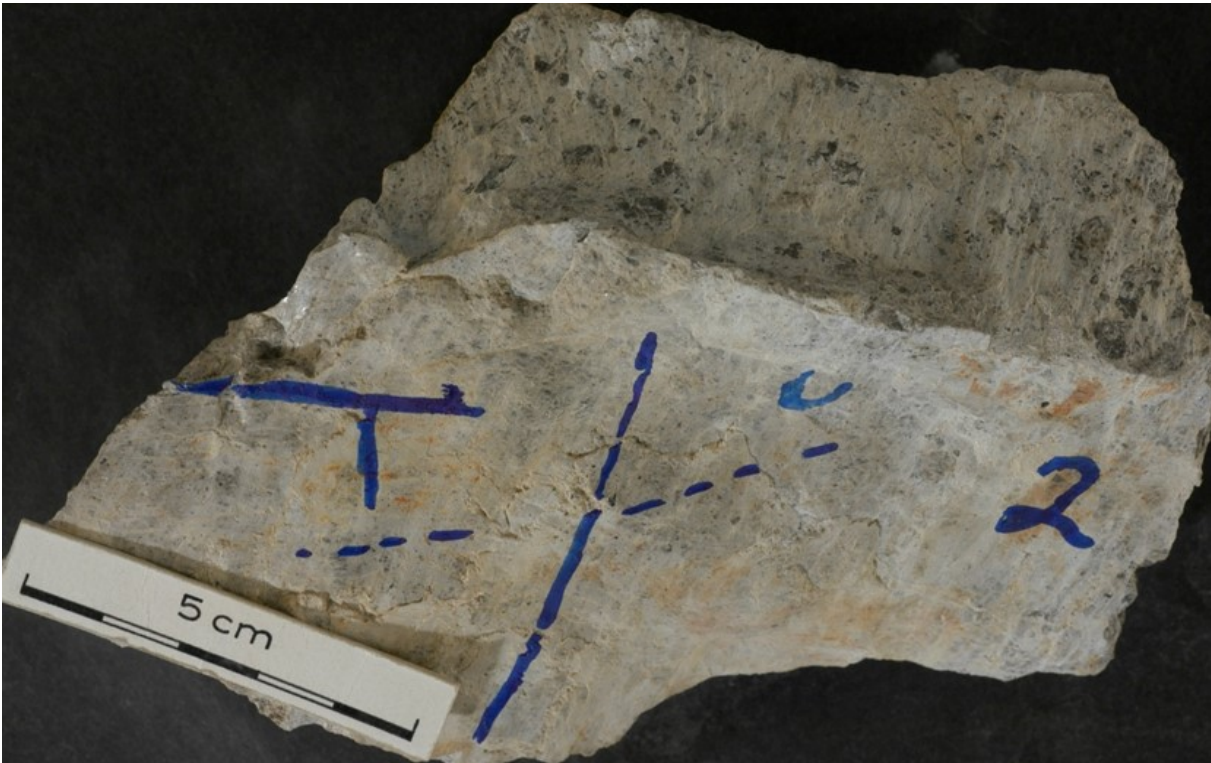


Figure 48: Sample 2 bordered by slip surfaces.

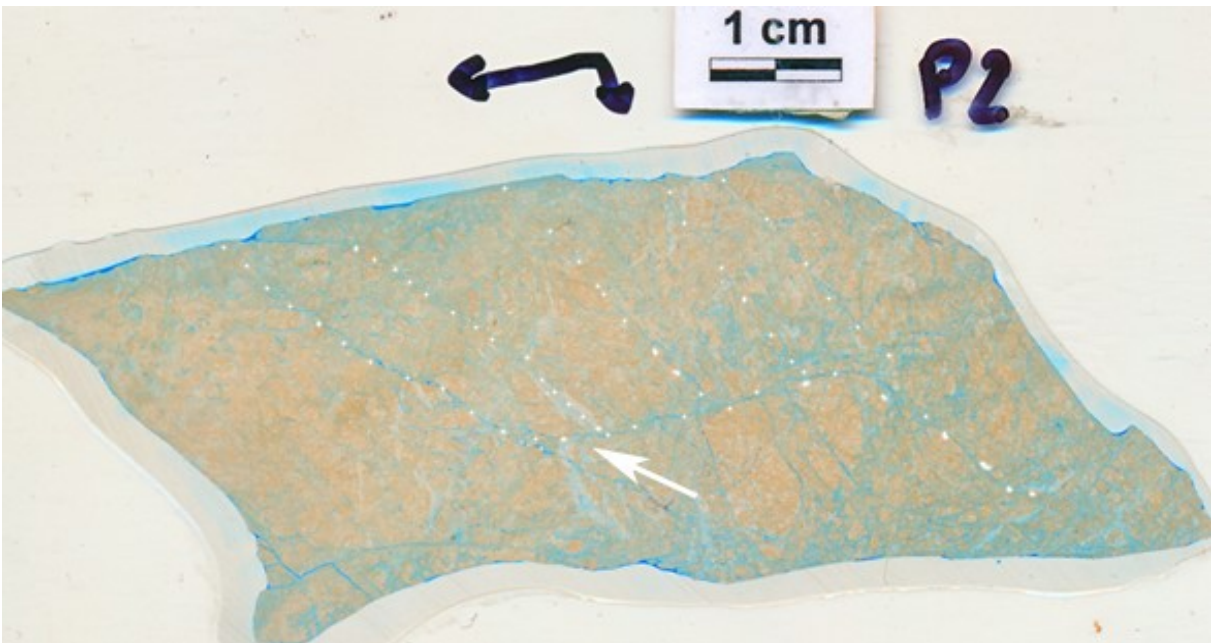


Figure 49: Thin section of sample 2. Sample was part of the hanging wall of the fault and is pictured upside down: Note offset on dolomite vein (white arrow) indicating normal faulting. Dotted lines: en echelon fractures connecting slip surfaces and micro fault offsetting the dolomite vein. Black arrow is marking the dip direction of the lineament/ the direction perpendicular to the fault plane. Picture was manipulated by raising saturation to show a better contrast between matrix and protolith.

Zoning

No zoning was observed apart from a sub-mm layer of ultra- fine mature cataclasite forming the pss.

Shear-sense indicators observed in sample and thin section

En echelon fractures intersecting the principal slip surface (PSS, which was part of the hanging wall as should be kept in mind when interpreting shear sense) at 45° indicate normal faulting if interpreted as tensile cracks. The same direction is indicated by a dolomite-filled vein offset by a plane subparallel to the PSS.

Matrix /protolith ratio

The whole piece consists of roughly 50% protolith.

Protolith grain shape and orientation

Grains appear angular to subangular with rounded tips. Many flat, elongated pieces which cause a lens-shape appearance in the section dominate and point towards intragranular extension fracturing as mechanism of grain size reduction (compare Billi, 2010, pp. 1397-1398). Grains are predominantly smaller than 5mm, but a few, internally heavily fractured grains reach up to 2.5cm diameter in the direction of the thin section and even more in the plane perpendicular to it as seen in the hand specimen. This preferred orientation of flat grains (Figure 49) seem to be produced by the en-echelon fractures discussed above.

Distribution and carriers of porosity in the sample

Fractures filled with porous cataclasite matrix carry most of the porosity observable in the thin section. The en echelon parallel fractures interpreted above as tension gashes show the largest opening widths (0.25-0.5mm). The very fine grained cataclastic matrix looks pale blue after vacuum treatment (Figure 49) with coloured resin and seems to be quite porous with pore sizes that cannot be resolved in the light microscope.

5.1.3 Samples 3 and 3.2

Macroscopic description, orientation of sample and thin section

Samples 3 and 3.2 stems from a fault of category 4 oriented 210/86 showing a slickenline of 300/35 and T-criteria indicating sinistral shear (see Figure 50). The thin section 3.2 is not oriented. Sample 3 is oriented and a thin section was prepared by slicing it parallel to the slickenline and perpendicular to the fault plane.

Sample 3 and sample 3.2 show distinct differences although they stem from the PSS of the same fault at less than a meter distance.

Shear-sense indicators observed in sample and thin section

Sample 3 shows matrix-filled en echelon faults at a low angle to the principal slip surface suggesting sinistral shear sense if interpreted as Riedel-Shears (and thereby giving additional weight to the field observations on the fault).



Figure 50: Looking down on the fault with samples 3 and 3.2 still in place. T-criteria indicate sinistral shear. The assumed tension gashes terminate in the protolith rock and are filled with the mature cataclasite forming the PSS. Tension gashes widen towards the fault and terminate at a distance of a few centimeters from the PSS. Note the presence of cemented and uncemented fault rock in the same fault pointing towards a reactivation postdating the cementation event. Note the thicker development of intermediate to mature cataclasite at the zone near the tension gashes (sample 3.2) and the dominance of the matrix to the right (sample 3) while bordering the same slickenside.

Zoning

While sample 3.2 consists of around 1 cm of mature cataclasite on intermediate cataclasite (see Figure 52), sample 3 looks different with mature cataclasite forming a 5 mm to 1 cm thick layer of mature cataclasite on 1-2 cm thick embryonic cataclasite above fractured dolomite protolith (Figure 51). This is an observation that I made repeatedly in the field: It seems that differences in fault geometry affects the way fault rocks form very locally.

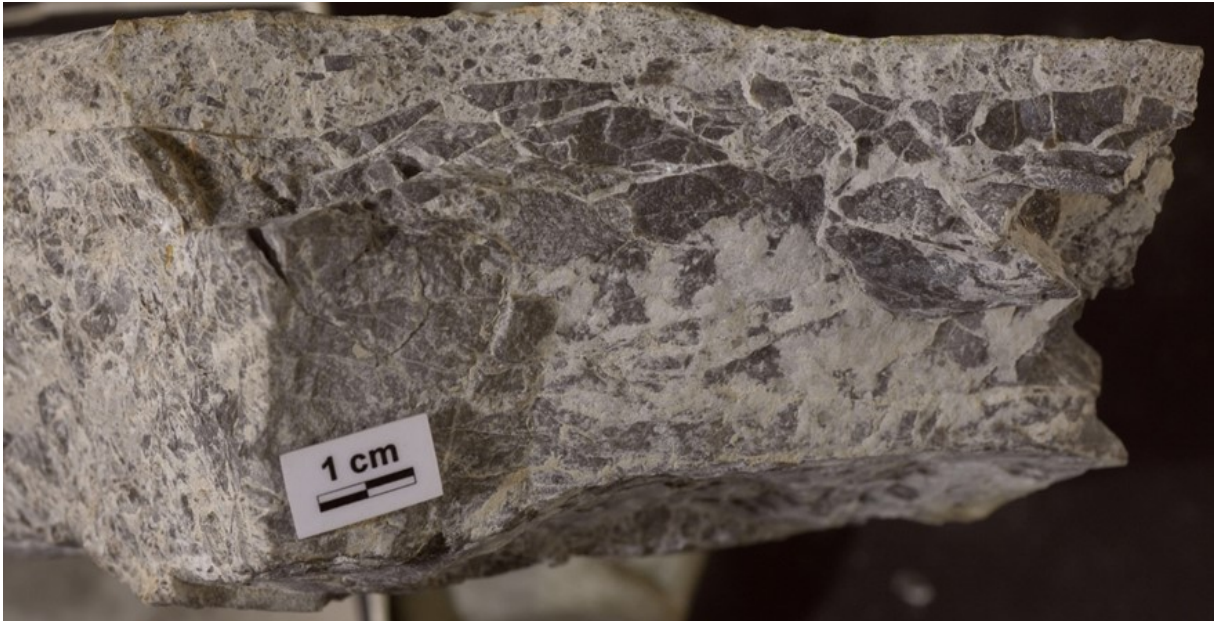


Figure 51: Sample 3. Mature cataclasite on embryonic cataclasite. Collected in-situ within a few centimeters from the same fault plane (compare Figure 50) from sample 3.2 (Figure 52).

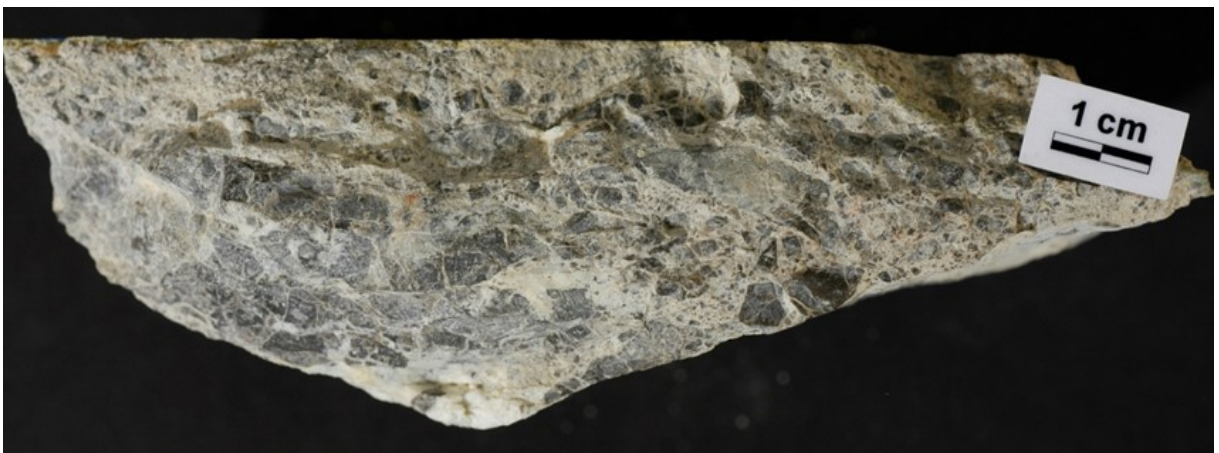


Figure 52: Sample 3.2 of mature cataclasite on intermediate cataclasite.

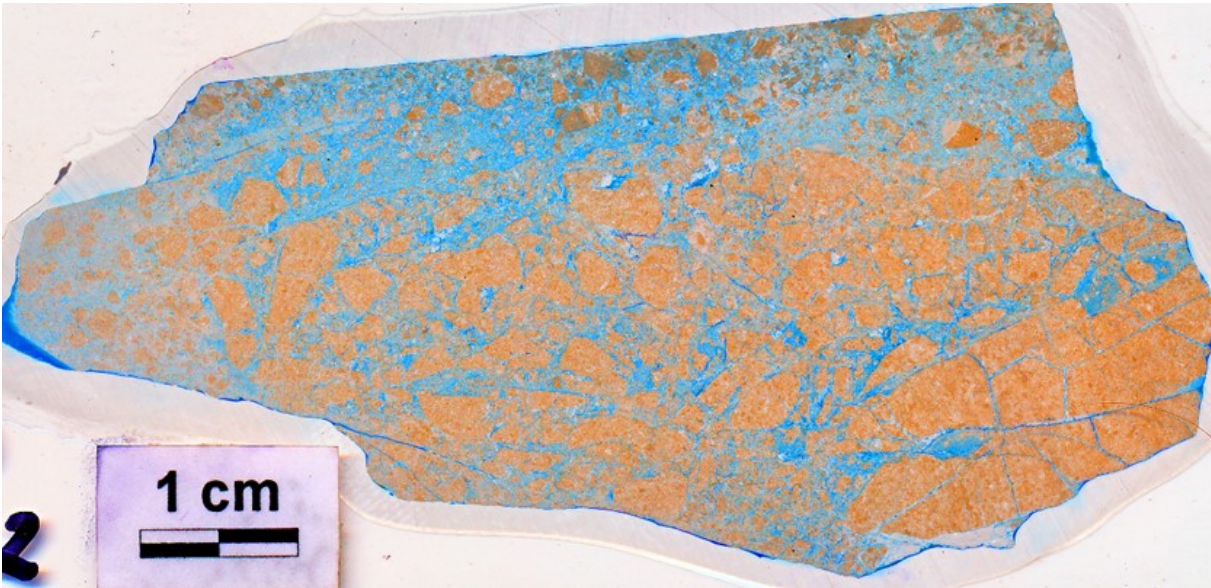


Figure 53: Thin section of sample 3.2.

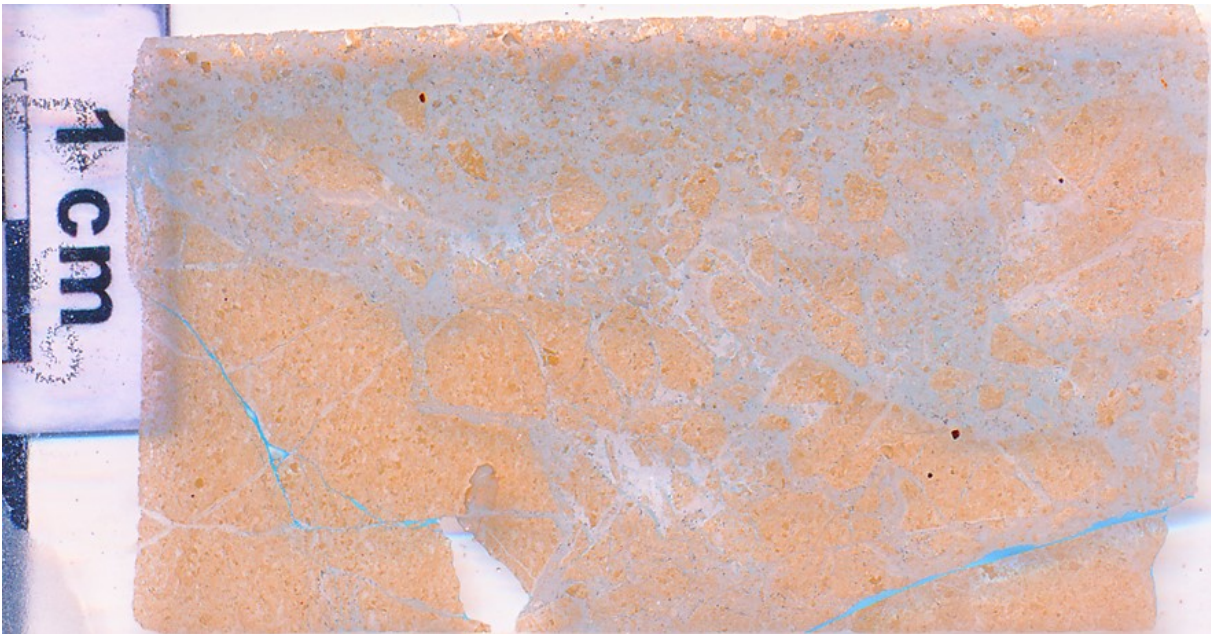


Figure 54: Thin section of sample 3.

Matrix/protolith ratio

Total sample 3 is around 80% fine grained matrix to 20% protolith, while sample 3.2 its 40% matrix to 60% protolith.

Protolith grain shape and orientation

Sample 3.2 shows a lot of elongated pieces often broken perpendicular to their long axis in the intermediate cataclasite-zone. Pieces, though elongated (of low sphericity) are sub-angular to sub rounded. The protolith pieces in the intermediate cataclasite are in the mm to cm range, the mature cataclasite contains- with few exceptions- pieces with a maximum diameter of one mm.

Distribution and carriers of porosity in the sample

Fractures and the fine cataclastic matrix separating the Protolith remains carry porosity. Its highest porosity is found in a 7mm layer adjacent to the PSS where the ultra-cataclastic material is dominant. The contents of cataclastic material gets less at larger distances from the PSS as protolith relics become dominant. Sample 3.2 should show higher porosity than sample 3 as it contains significantly more of the high-porosity matrix.

Other observations

An unusual observation in section 3.2 is a concentration of grains darker than the in-situ-protolith of the sample near the principal slip surface. They seem to stem from a bed of different composition dragged into the fault (Figure 53).

5.1.4 Sample 5.2

Macroscopic description, orientation of sample and thin section

Sample 5.2 is a 7cm wide piece consisting entirely of mature cataclasite (Figure 55) from a steep dipping fault bordered on both sides by slickenside showing slickenlines of three different movements. The slip surface is oriented 244/89, the dominant slickenline 330/25. The fault is classified to category 3. The fault rock consists of mostly microscopically fine grained material with eye visible intact protolith grains less than 5mm in diameter.

There are a few scratches on the surface indicating younger movements as well. The thin section was prepared by cutting parallel to the dominant slickenline and perpendicular to the fault plane.



Figure 55: Sample 5.2. A plane of ultra-fine mature cataclasite, likely a former PSS, separates two zones of different matrix/protolith ratio and protolith grain size. Length of sample = 12 cm.

Zoning

The hand specimen is separated into two coarse zones parallel to the strike of the fault (Figure 56). The two slip surfaces form the border of the sample by a layer of protolith free pure white matrix-material. This layer, which can be considered a former slip surface, was cemented after being blurred by what were likely processes of liquefaction (compare Schröckenfuchs et al 2015 p.67) and not activated in later movements on the fault.

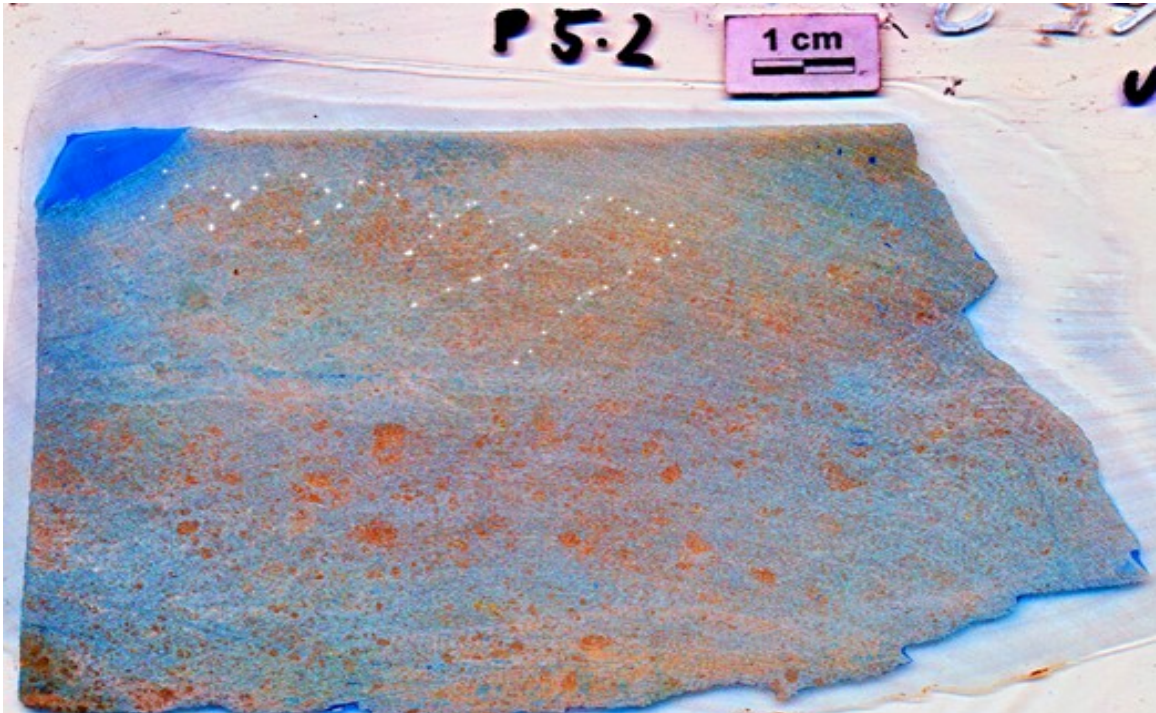


Figure 56: Sample 5.2 "Ghosts" of domino-like blocks (marked by the white dots) with high content of protolith-fragments separated by matrix rich areas resemble the structure produced by en echelon fractures connecting slip surfaces in Figure 49.



Figure 57: Small section prepared from sample 5.2.

Matrix/protolith ratio

Between the former slip surface mentioned above and the upper (in the pictures of sample and panorama-section) PSS the protolith content is around 5%, on the other side its clearly higher and around 15%.

Protolith grain size shape and orientation

While protolith grains stay well below 5mm diameter in the zone above the former PSS, they are bigger in average with a few clasts reaching 8 to 12mm right below it. Grains are subrounded to rounded with high sphericity in the zone above the cemented former PSS, subangular to subrounded for around 1.5cm right below it and get increasingly rounded and spherical again towards the second PSS.

Distribution and carriers of porosity in the sample

Porosity is carried by the fine matrix but is lower here than in other fine cataclasites. White seemingly cemented and thereby impermeable parts of the sample could not be penetrated by the coloured resin used for preparation (Figure 58). These impermeable areas preferentially occur near the PSS forming the long sides of the sample and more so in the zone with less protolith and more cataclastic matrix but can be found all over the section.



Figure 58: Spotty porosity distribution: Long side = 2 cm, saturation enhanced

Spot shaped areas of higher porosity can be found within areas of no or little effective porosity in the section. Fractures within protolith grains remained open (Figure 59), but are likely enclosed in the impermeable matrix and thereby not part of “effective porosity”. The absence of fracture porosity and the small pore diameters are indicative for low permeability, as well as the only weak and partial penetration by the resin after weeks of vacuum treatment.



Figure 59: fragmented protolith grains in sample 5.2 showing partly open fractures with a cement. Length of picture is 2 cm.

Other observations: Matrioschka fault rock and liquefaction structures on former PSS

The bigger protolith grains in the second zone are often fragmented into smaller pieces. The cracks in between are partly open (which could be an artefact of section preparation) and partly cemented with a white cement different from the material surrounding the clasts which points towards reactivation of already fractured and cemented rock. Some clasts (see Figure 79 for an image) are clearly reworked cemented faultrock within cemented faultrock – Matrioschka fault rock so to speak. The ce-

mented PSS in the center of the specimen shows cloudy, bulbous deformation pointing towards potential liquefaction processes (compare Schröckenfuchs et al. p.67) instead of forming a sharp line (see Figure 83 and its discussion on page 101).

Shear-sense indicators observed in sample and thin section

Some darker areas (with a higher percentage of eye-visible protolith grains) which are interpreted as the remains of even bigger in-situ fragmented protolith fragments show a domino-like pattern (highlighted by dotted line in Figure 56) separated by en-echelon areas filled with ultra-cataclastic material. These supposed en-echelon fractures include an acute angle of 35° with the slickenside in the section sub-parallel to the dominant slickenline and perpendicular to the two slickensides. These fractures separating the dominos terminate in the ultra-fine cataclasite forming the sample-terminating slickenside on one side and in the former slip surface on the other. Interpreted as Riedel-faults formed in a transpressive regime these fractures would indicate sinistral shear for the event causing the pattern on that fault H 244/89, L 330/25, which would belong to the steeper members of category 3. It looks a lot like the pattern observed in the section of sample 2, just that the protolith is already fragmented to a higher degree and that the fine material forming the "faults" indicates their formation as shear surfaces. Anyhow, shear sense interpretation would be the same if interpreted as T-criteria like I did in sample 2.

5.1.5 Sample 7.2

Macroscopic Description, Orientation of sample and thin section.

Sample 7.2 (Figure 60) is a piece from the north-eastern wall of a fault categorized as category 3. The orientation of the fault plane is 252/72, that of the slickenline 172/27. The fault showed questionable sinistral shear sense indicators in the field. Sections were prepared parallel to the lineaments and perpendicular to the fault plane.

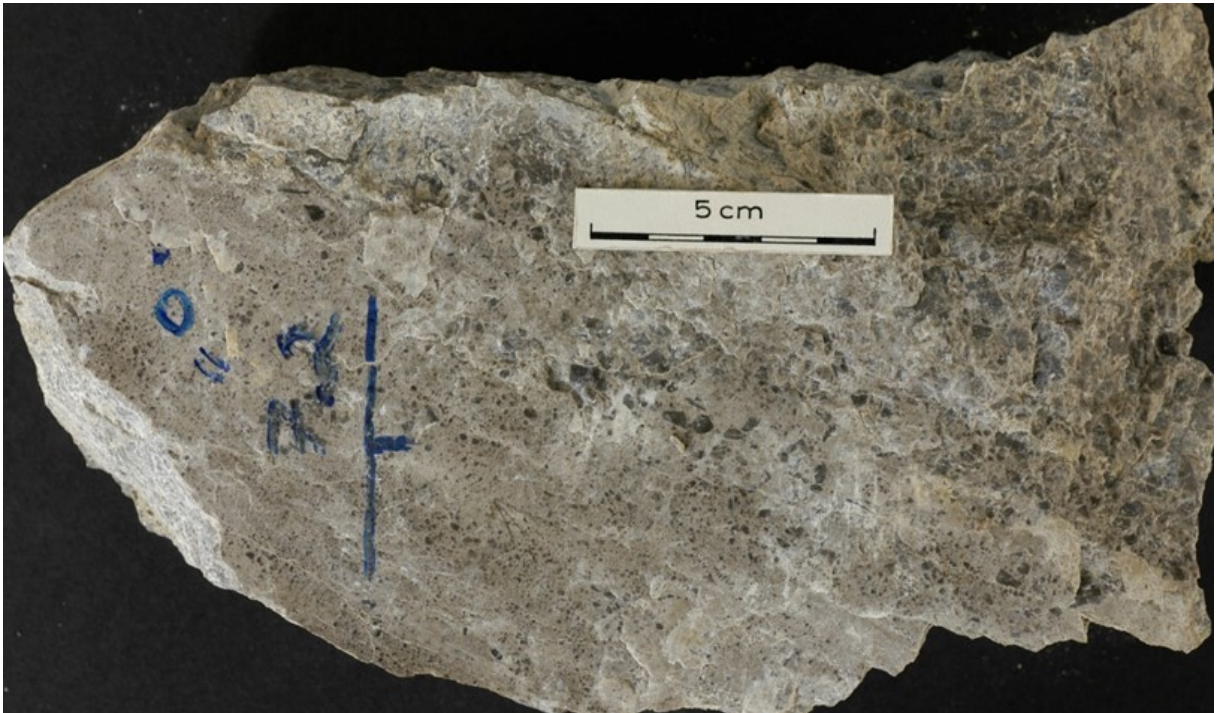


Figure 60: Sample 7.2, view on the mirror polished slickenside showing (also mirror polished) truncated clasts

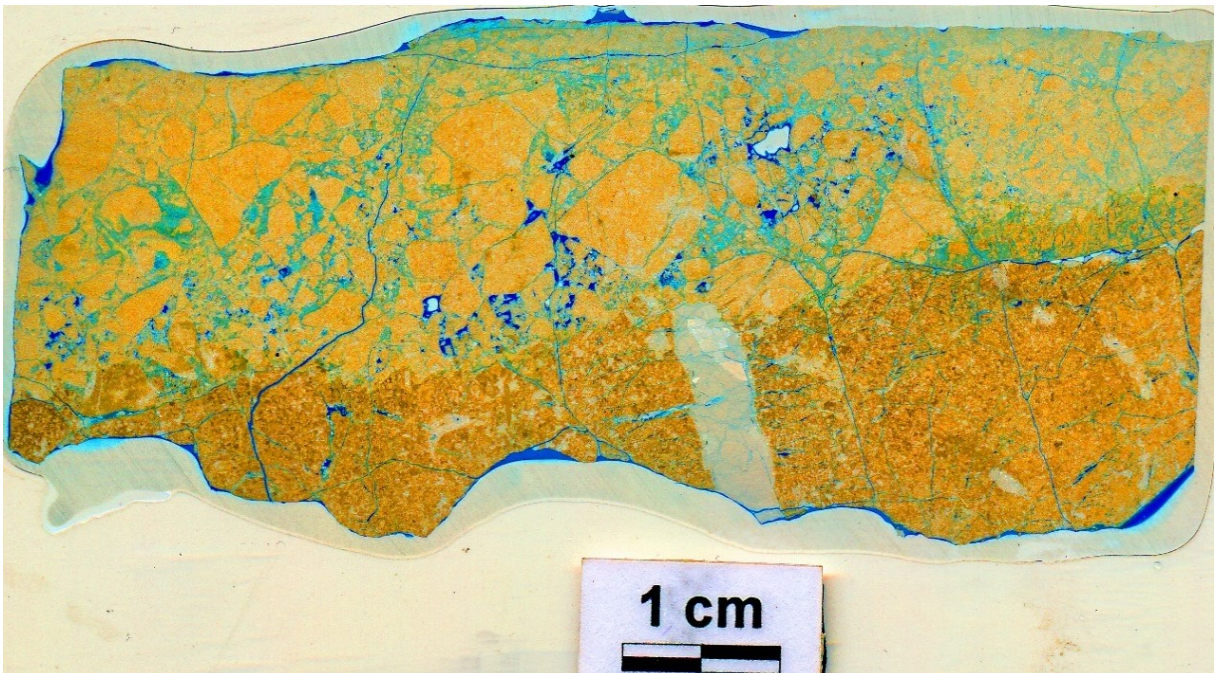


Figure 61: Panorama section parallel to the slickenline and perpendicular to the fault plane of sample 7.2. Saturation electronically enhanced to show diffuse porosity in fine-grained fault rock. Dark blue areas mark open fractures with 100% porosity.

Zoning

The remaining sample blocks consist of fractured dolomite and intermediate to mature cataclasite towards the PSS (as also visible from the section in Figure 61). Fault rock thickness and type varies in 3D (over several blocks sliced for the preparation of thin sections), but on average its 2cm of intermediate cataclasite forming a relative sharp border with slightly fractured protolith dolomite.



Figure 62: Stylolites and subtle zoning in a section prepared from sample 7.2. Saturation enhanced.

The thin section of sample 7.2 pictured in Figure 62 was prepared from a part of the sample consisting mostly of mature cataclasite that was bordered by two PSSs with slickensides at the upper and lower side (of the section like in Figure 62). It shows roughly four zones:

The 5mm thick mature cataclasite at the upper PSS in Figure 62 contains a stylolite at 2-3mm distance from the PSS. Another seemingly slickenside-parallel stylolite separates the center of the thin section showing a higher content and size of the protolith clasts. These clasts are broken and rotated. Fine-grained cataclastic material separates this rock type from the 1cm thick intermediate to mature cataclasite adjacent to the lower PSS.

Matrix/protolith ratio

The intermediate cataclasite that forms the most part of the fault rock in the sample (slightly fractured matrix forms the rest) has, as a protolith content of around 70%.

Distribution and carriers of porosity in the sample

Porosity is partly carried by the fine cataclastic matrix. There are also open vuggy, spherical cavities up to a few mm diameter, partly containing idiomorphic dolomite crystals in the cataclastic parts that could be reached by the resin (the dark blue-rimmed holes in the section in Figure 61). This fault rock shows no connective fractures in the sample.

Protolith grain size, shape and orientation

The small section is quite different from the panorama section as it stems from a part of the fault with a thicker layer of mature cataclasite and samples only this layer. In the panorama section a thin layer of mature cataclasite with rounded to sub-rounded grains is covering a layer of around 2 cm of intermediate cataclasite containing mostly subangular grains which in turn forms a relatively sharp contact to slightly fractured protolith (compare Figure 61)

In the small section two zones of fine grained, mature cataclasite enclose a zone of subrounded to subangular grains, with one of the stylolites shown in Figure 62 forming the boarder towards the PSS (upper border in Figure 62).

Other Observations: Stylolites

The occurrence of stylolites in the section in Figure 62 points towards pressure solution mechanisms at work. Their parallelism to the PSS in the section seems strange (stylolites, if formed in the same stress field as the fault, should be oriented perpendicular to the shortening direction); observations on the remaining block show the lower stylolite to also occur at a relative flat angle to the pss. They mostly affect the matrix, with a few noteworthy interactions with protolith grains. While the upper (towards the PSS) stylolite seems to only affect the cataclastic matrix, the lower stylolite also runs around protolith grains and through pre-existing fractures in protolith grains. The frequency of the stylolite-serrations goes down in the cases it passes through fractures in grains, while the grains which are in outer surface contact with the stylolite are also affected by the serrations which in turn get a more rounded appearance than if occurring only in the matrix.

The stylolites likely originate from a stress field younger than the fault because:

- a) they formed in already established fault rock
- b) a stress field with the compression direction nearly perpendicular to the fault plane cannot have produced the fault nor caused any movement on it as its shear stress component would be near zero for this plane.

Shear sense indicators

While none of the sections shows shear sense indicators, a vein filled with dolomite cement terminating at the border between protolith and fault rock (also visible in the big section) shows a few mm of sinistral offset in one of the oriented blocks confirming the field observations (Figure 63).

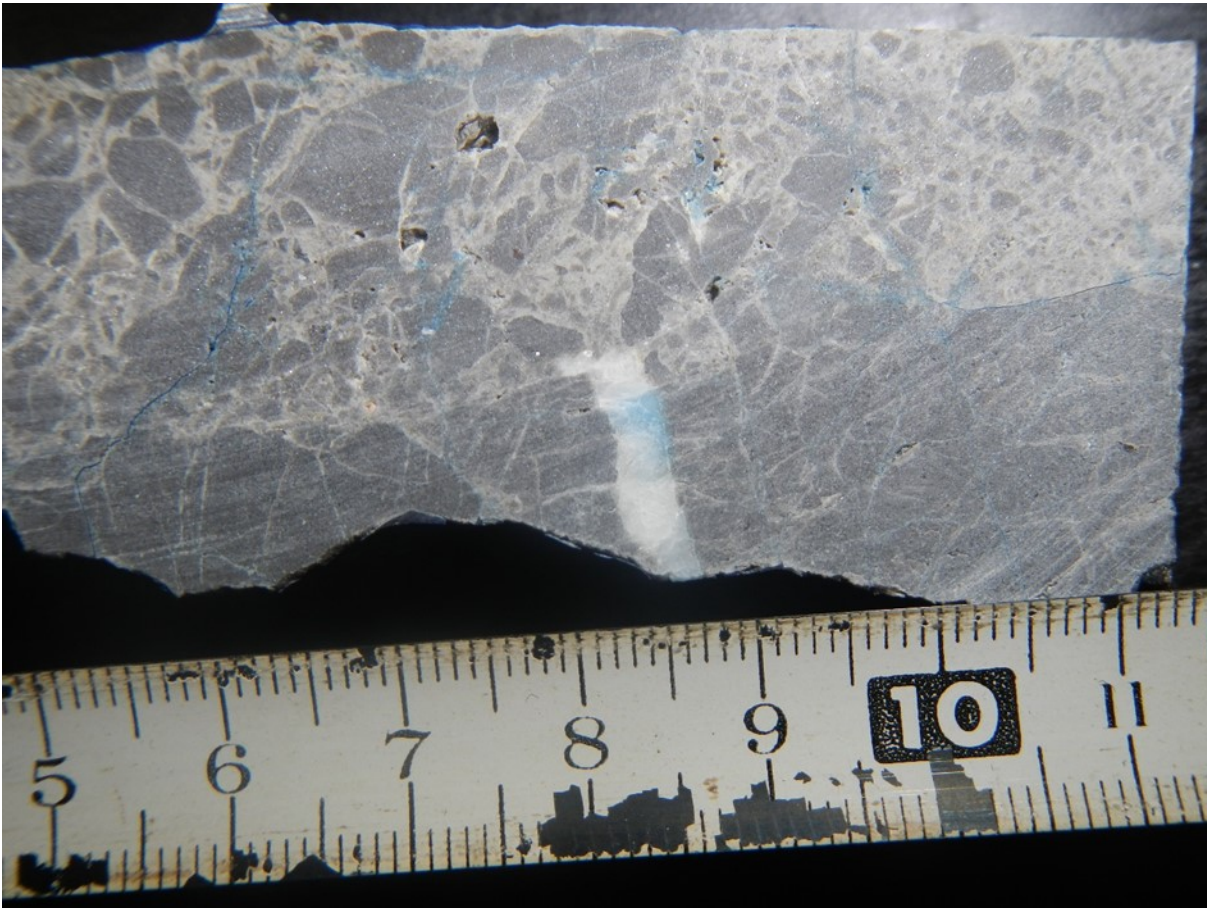


Figure 63: Sample 7.2. View from above (on the true upside) of a block cut parallel to the slickenline and perpendicular to the fault plane. The section shows a clast containing part of a dolomite-vein offset to the left along the border between fractured matrix containing the vein and fault rock.

5.1.6 Sample 10

Macroscopic description, orientation of sample and thin section

Sample 10 (Figure 64) derives from a fault with the orientation 214/89 showing a slickenline oriented 300/35. By its orientation the fault is very similar to the one sample 3 and 3.2 were taken from. The thin section was prepared parallel to the slickenline and perpendicular to the slickenside.

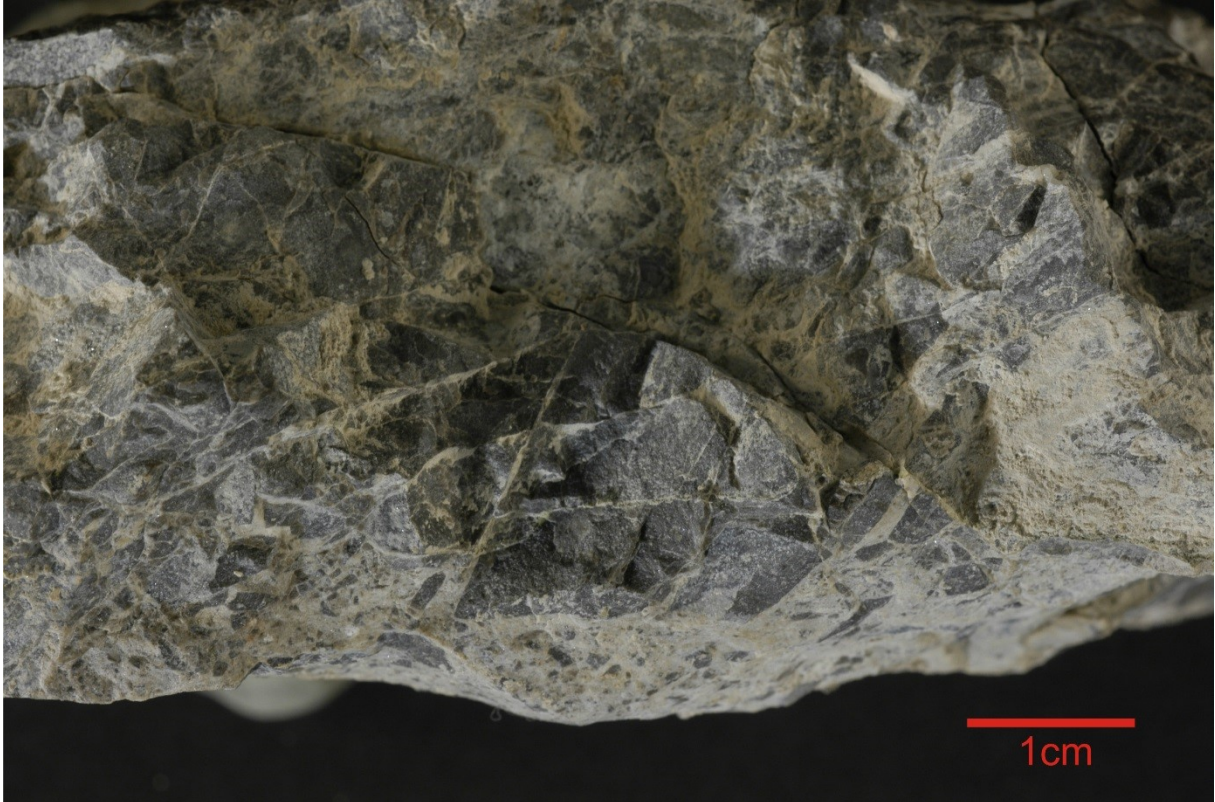


Figure 64: Sample 10, the PSS with a layer of cataclastic material visible on the lower side.

Shear-sense indicators observed in sample and thin section

T-criteria pointing towards sinistral shear are observed in the hand specimen and the thin section.

Zoning

A 5-8 mm thick layer made up of mature cataclasite forms the slickenside above a damage zone of cracked unaltered dolomite host rock (Figure 64) which is still in situ but fragmented with up to 1cm wide gashes filled with the fine-cataclastic material penetrating the host rock from the PSS to a distance of up to 3 cm (Figure 64, Figure 65, Figure 66).

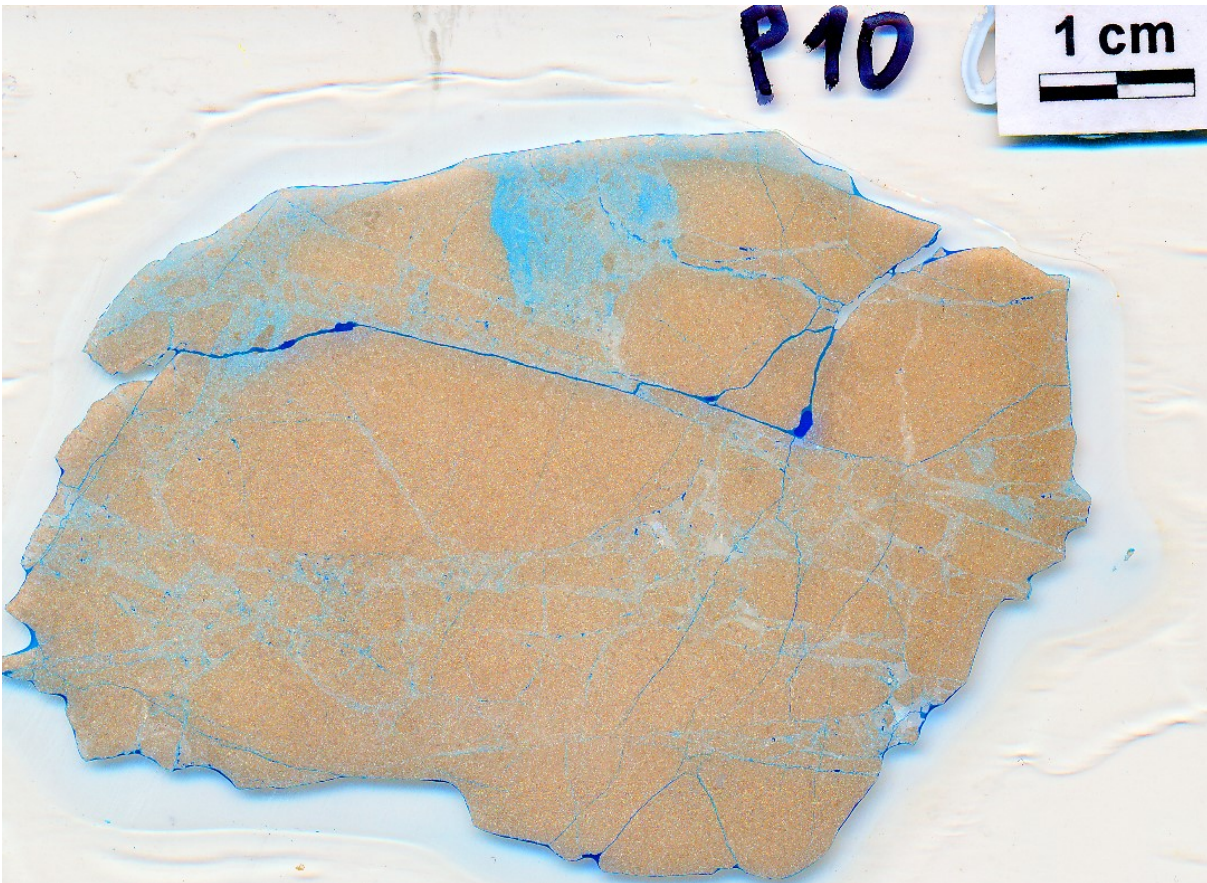


Figure 65: Thin section of sample 10. Fractured protolith with a thin layer of mature cataclasite forming the PSS. Fine cataclastic fault rock (blue) penetrating seemingly insitu dolomite along a wide fracture in the upper center of the section.

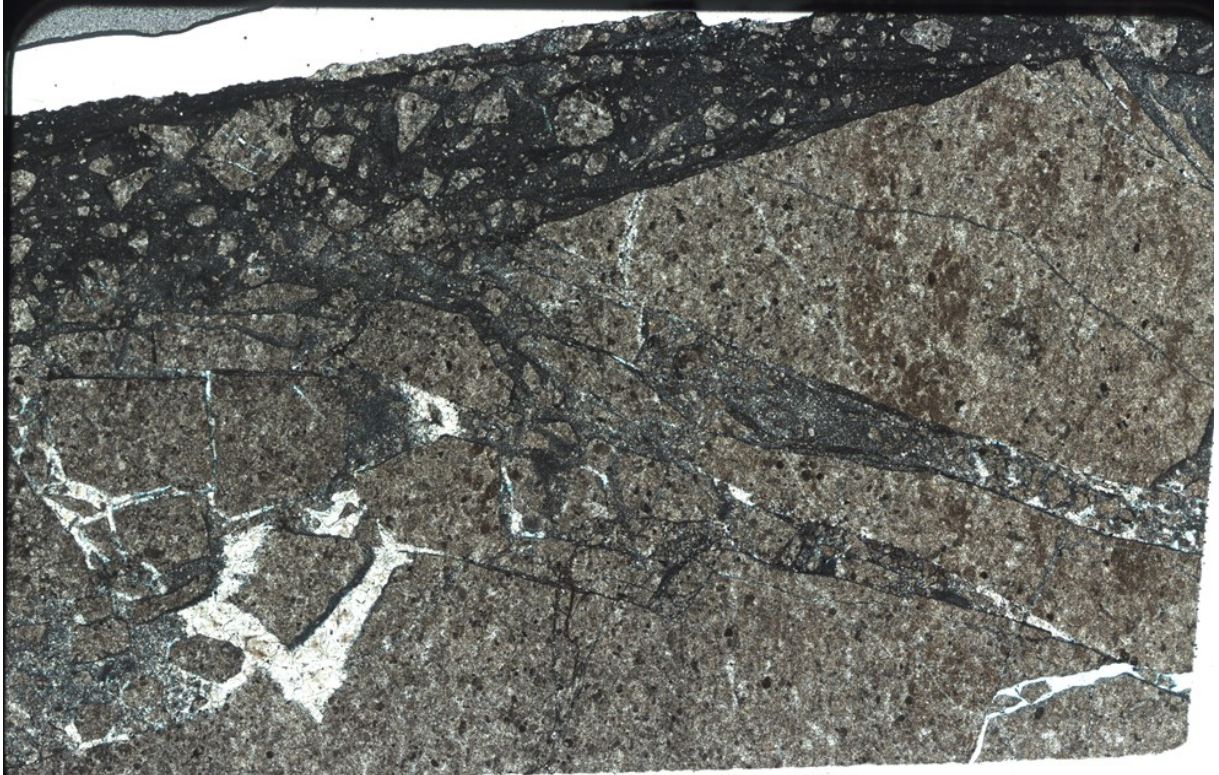


Figure 66: Thin section prepared from sample 10. Small grains, mature cataclasite (dark material) and cements (white areas) in tensile cracks in fractured protolith rock. Long edge of image = 3.7cm.

Matrix/protolith ratio

In the whole piece: 2/3 protolith to 1/3 matrix, in the mature cataclasite between 15 and 20%.

Protolith grain shape and orientation

The cataclasite layer near the PSS shows subrounded to rounded clasts of varying sphericity, with parts of the sample showing elongated pieces likely produced by tension gashes like the one visible in the section shown in Figure 66 .

Distribution and carriers of porosity in the sample

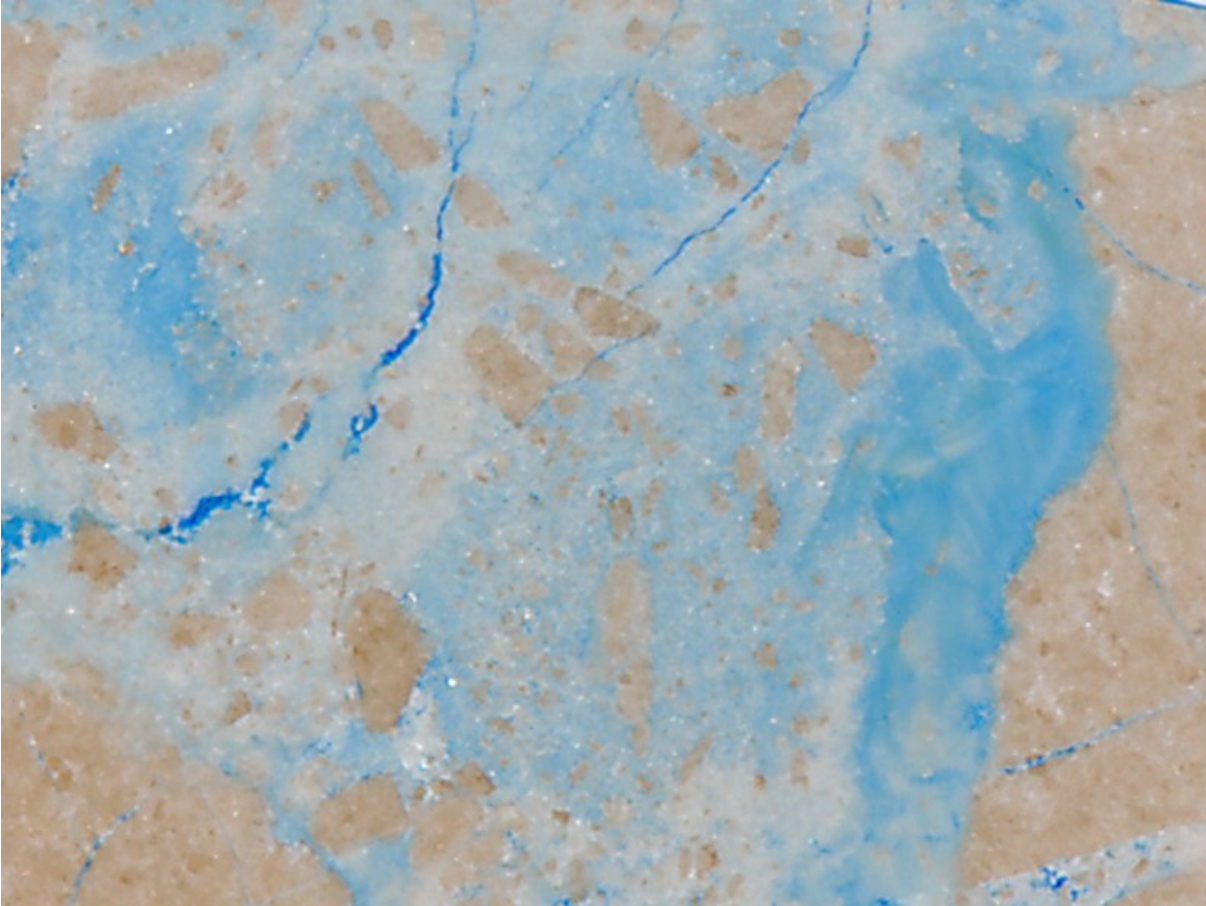


Figure 67: Thin section of sample 10. Porosity is distributed unevenly in the cataclastic matrix. Scan from the panorama section, saturation electronically enhanced. Length of picture = 1 cm,

Most of the porosity of the sample is provided by small pores distributed in the mature cataclasite forming the PSS and filling the cracks and the fracture described above. This material is not homogenous in its porosity. The blue resin-dye shows cloudy distribution with cemented impermeable/non-porous white areas in-between (Figure 67). Some of the few open fractures could well have developed during sampling, but sure not all of them. Most of the fractures in the section are filled with the microporous cataclastic material, but there are also parts entirely sealed by well-crystallized cements of iron free dolomite and tiny open cavities lined by idiomorphic calcite of the same material.

Other Observations

In the thin section made from sample 10 the tension gashes opening towards the PSS are filled with cataclastic material (showing pores and looking dark in transmitted light) nearly to the end. At the tips/ of the fractures they are cemented with clear, idiomorphic crystals of iron-free dolomite (Figure 68).

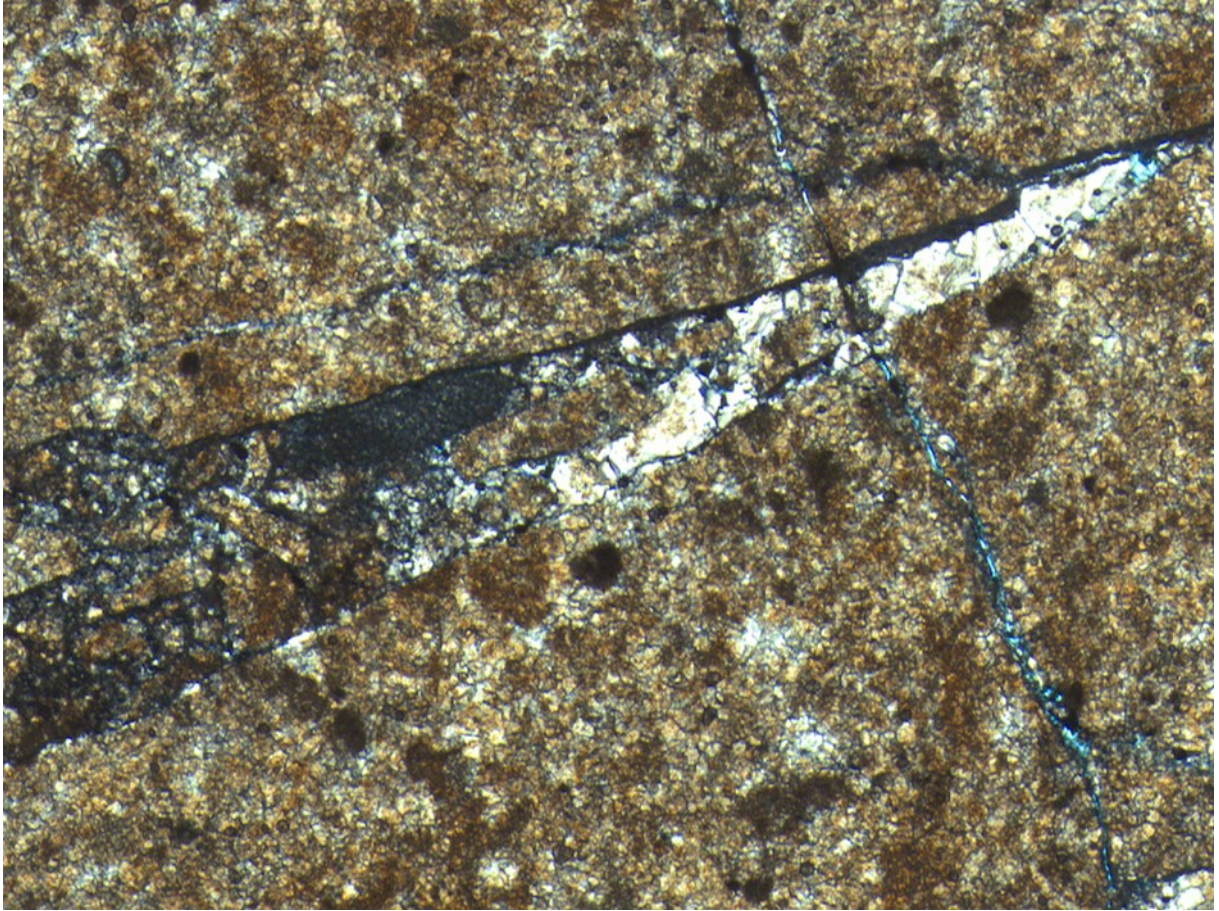


Figure 68: Sample 10. Dolomite cement at the end of a tensile crack otherwise filled with cataclastic matrix and small grains (dark material). Length of picture = 7mm.

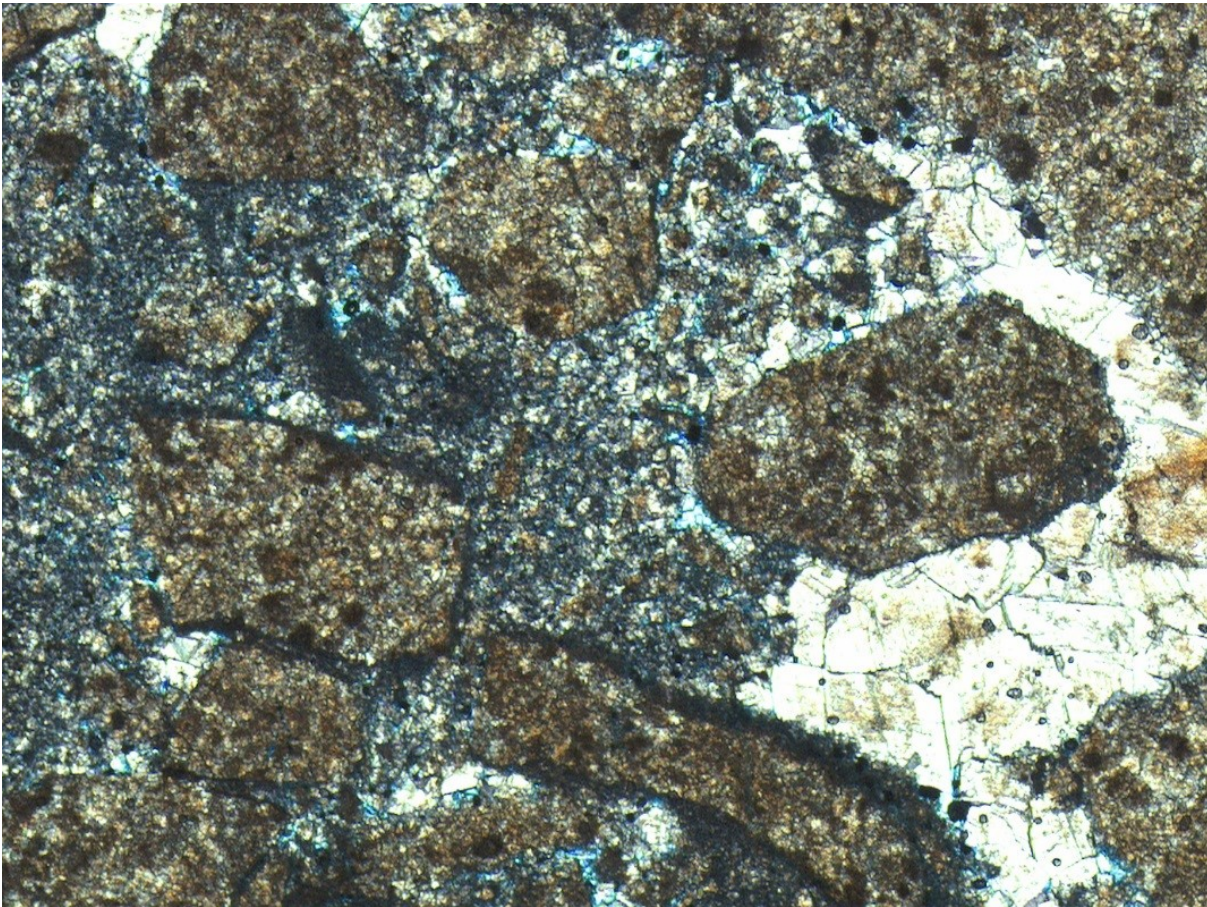


Figure 69: Sample 10. Dolomite cement and cataclastic matrix in another crack. Length of picture = 7mm. Dark rim around grains could be a fine grained rim as compared to data by Theresa Schröckenfuchs.

While the cataclastic material shows some porosity, the cement does not. The cataclastic material is usually absent from wherever the cement fills fractures, it was either absorbed, came later or somehow manages to block nucleation/crystal growth (Figure 69).

5.1.7 Sample 11

Macroscopic description, orientation of sample and thin section

Sample 11 (Figure 70) is a piece from one of the strongly fractured, slightly red coloured beds that show a distinctly different deformation behaviour and porosity than the surrounding dolomite rock in the quarry. The sample was taken from a position directly below a bedding-subparallel slip zone. It is unoriented. The sample is strongly fractured dolomite (most fragments smaller than one cm) showing a jigsaw-puzzle like pattern produced by protolith grains separated by finely porous cataclastic material. (Figure 70, Figure 71). Thereby it fits the description of a dilation-breccia. While most of the veins of sparitic dolomite transecting the piece show no

offset on the younger fractures, only a few show a tiny lateral (shear) component as well. A low percentage of partly open fractures shows idiomorphic dolomite crystals growing on the walls.



Figure 70: Sample 11 Jigsaw-puzzle-like fit of protolith grains in a "dilation breccia".



Figure 71: Section of sample 11. Note the fine network of younger fractures filled with porous material only rarely offsetting cemented older ones.

Matrix/protolith ratio

More than 60% protolith.

Protolith grain size, shape and orientation

Protolith grains are angular to subangular and increase in rounding and sphericity as they decrease in size in the areas with higher matrix content. Wherever there is hardly no matrix involved and only slim fractures separate pieces also the smaller grains show an angular appearance. Grains marked by dolomite-cemented veins rarely show lateral displacement (although they do in some cases); most fractures seem to be purely extensional without showing any shear component in the displacement in the section (Figure 71).

5.1.8 Sample 13**Macroscopic description, orientation of sample and thin section**

Sample 13 stems from a mighty fault system with anastomosing fault planes of unknown variable orientation. The strike direction of the fault at a larger scale is unknown but may be approximately E-W as suggested by old aerial photos from NÖGIS suggest. It is cropping out in the NE of the second level of the quarry and shows a core of mature cataclasite with over 1 m thickness. It consists purely of mature cataclasite showing multiple slickenlines and fault planes. The system shows late and dominant slickenlines caused by normal faulting. The fault is more or less vertical, indicating that it formed as a strike slip fault if thinking about Anderson's law. The section was erroneously prepared perpendicular to the dominant slickenline and the fault plane. The section is terminated by fault planes at both long sides.

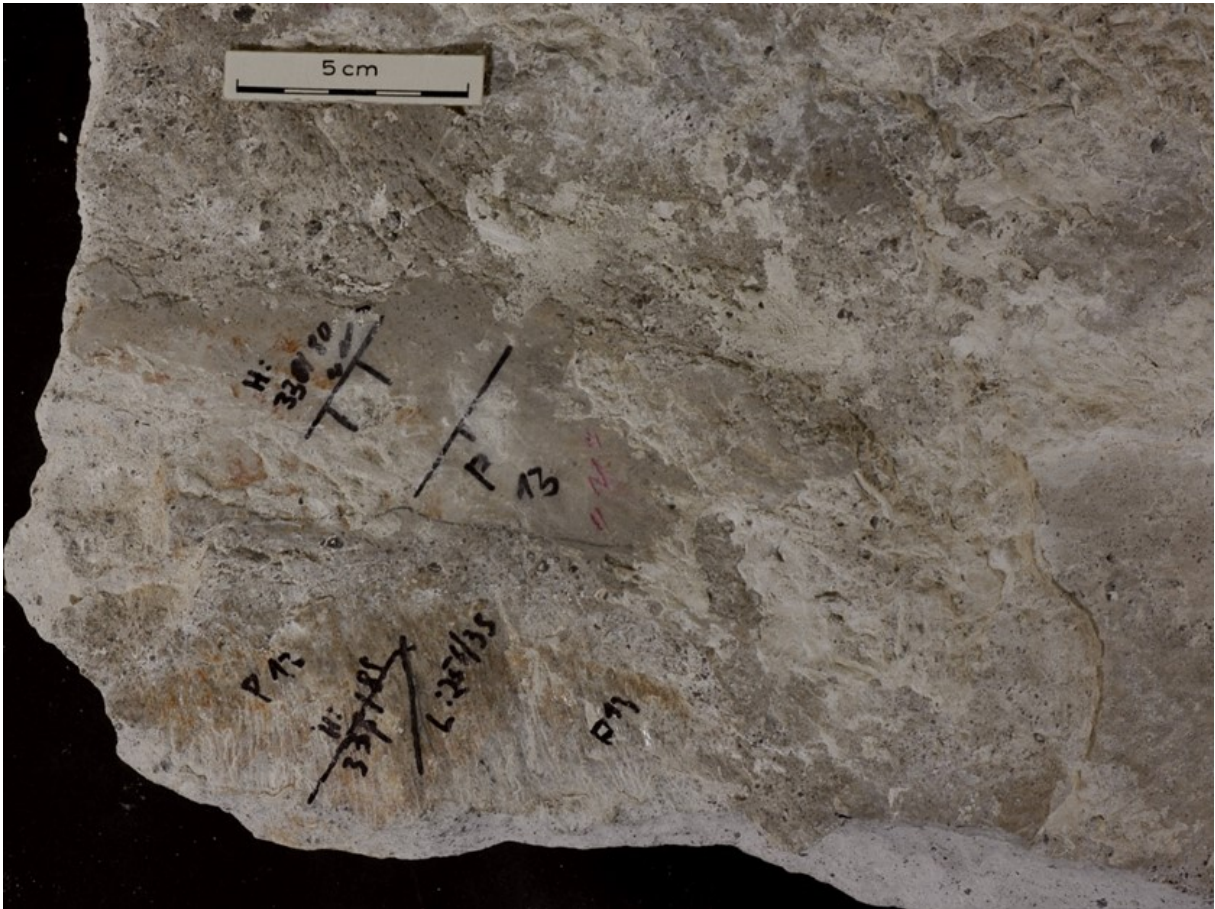


Figure 72: Sample 13 shows multiple slickensides in a piece of mature cataclasite

Shear sense indicators

Normal faulting was indicated by field observation of lunate fractures.

The sample shows subordinate fault planes at a low angle with the PSS with slickensides different from the one on the main PSS (Figure 72). These could be conserved Riedl planes of an earlier movement. Interpreted as such, they would indicate a phase of dextral shear on the fault that predates normal faulting. For a steep fault like this development as a strike-slip fault is likely.

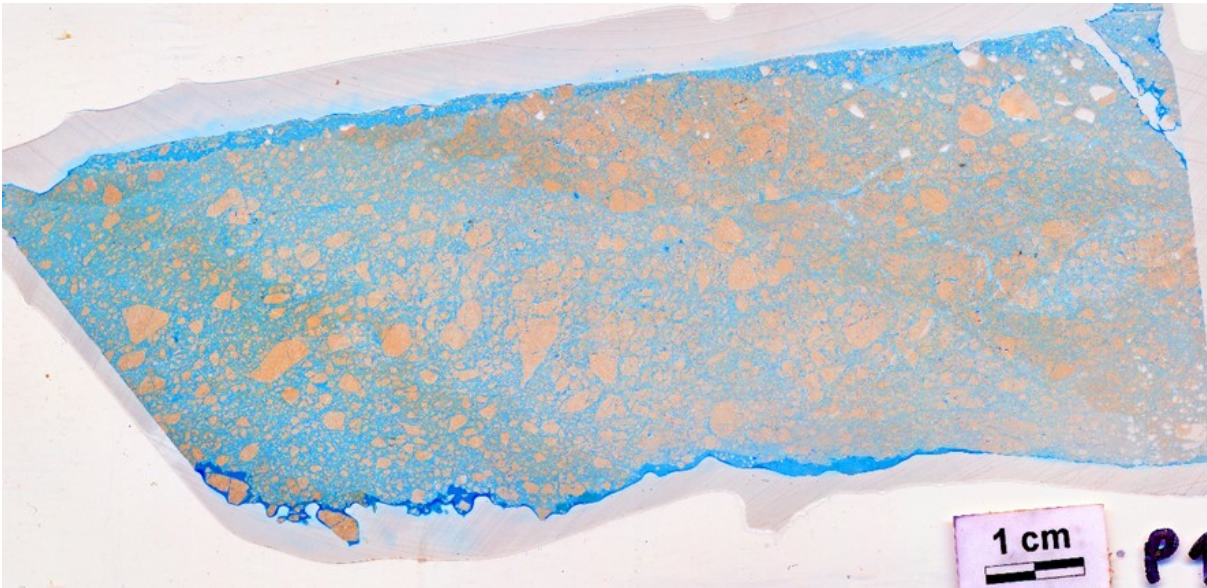


Figure 73: Section prepared from sample 13

Distribution and carriers of porosity in the sample

Porosity is distributed all over the fine cataclastic material in pores smaller than the resolution of the light microscope.

The material shows no relevant fracture porosity (Figure 73). Because of this and the tiny pore diameters permeability of the fault rock is likely low.

Zoning

A slight tendency of “coarsening inwards” is observed with bigger protolith clasts occurring closer to the centre between the two slip-surfaces shaping the hand specimen and thin section (Figure 73).

Matrix/protolith ratio

50% relatively homogenous throughout the piece.

Protolith grain size, shape and orientation Grains appear subrounded to rounded in the first 1.5 cm from the two PSS of the piece and get subangular to angular towards its core. In the center, away from the two slickenplanes, a few pieces of low sphericity are observed while sphericity is generally high

5.1.9 Sample 14

Macroscopic description, orientation of sample and thin section

Sample 14 (Figure 74) stems from a big fault zone in the SE of the lowermost level of the quarry. It is a piece of fault rock that was just cemented enough to be taken away

as a piece during a dry weather period. The same rock softens in water. This rock type is truly at the border between “kakirite” and “cataclasite” and could only be cut and treated after prolonged drying and vacuum-impregnation with resin. As orientation got lost during preparation, the sample is a random section with no relation to the PSS.

Zoning

In the hand-piece, a gradual change from approximately 1 cm thick layer of mature cataclasite to 8 cm of increasingly coarser grained intermediate cataclasite is observable (Figure 74). As the thin section was prepared unoriented no zoning can be observed in the section.

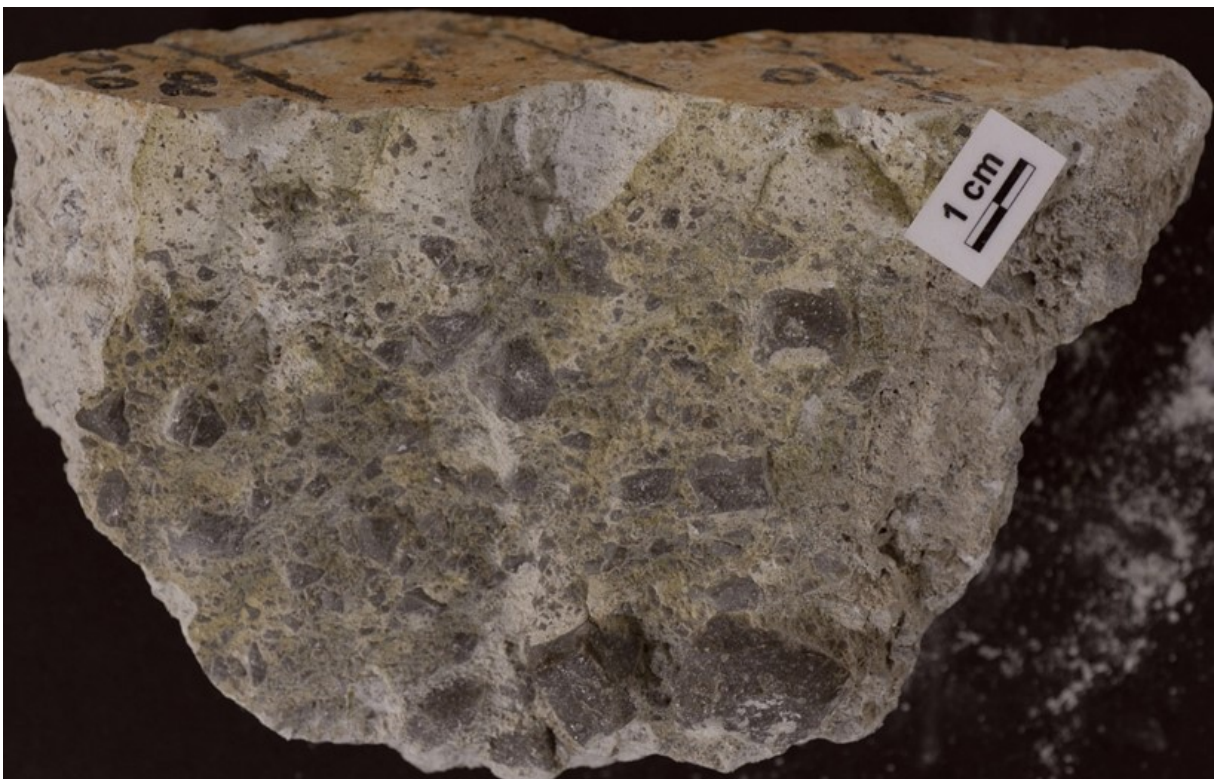


Figure 74: Sample 14. Between cohesive and incohesive fault rock.

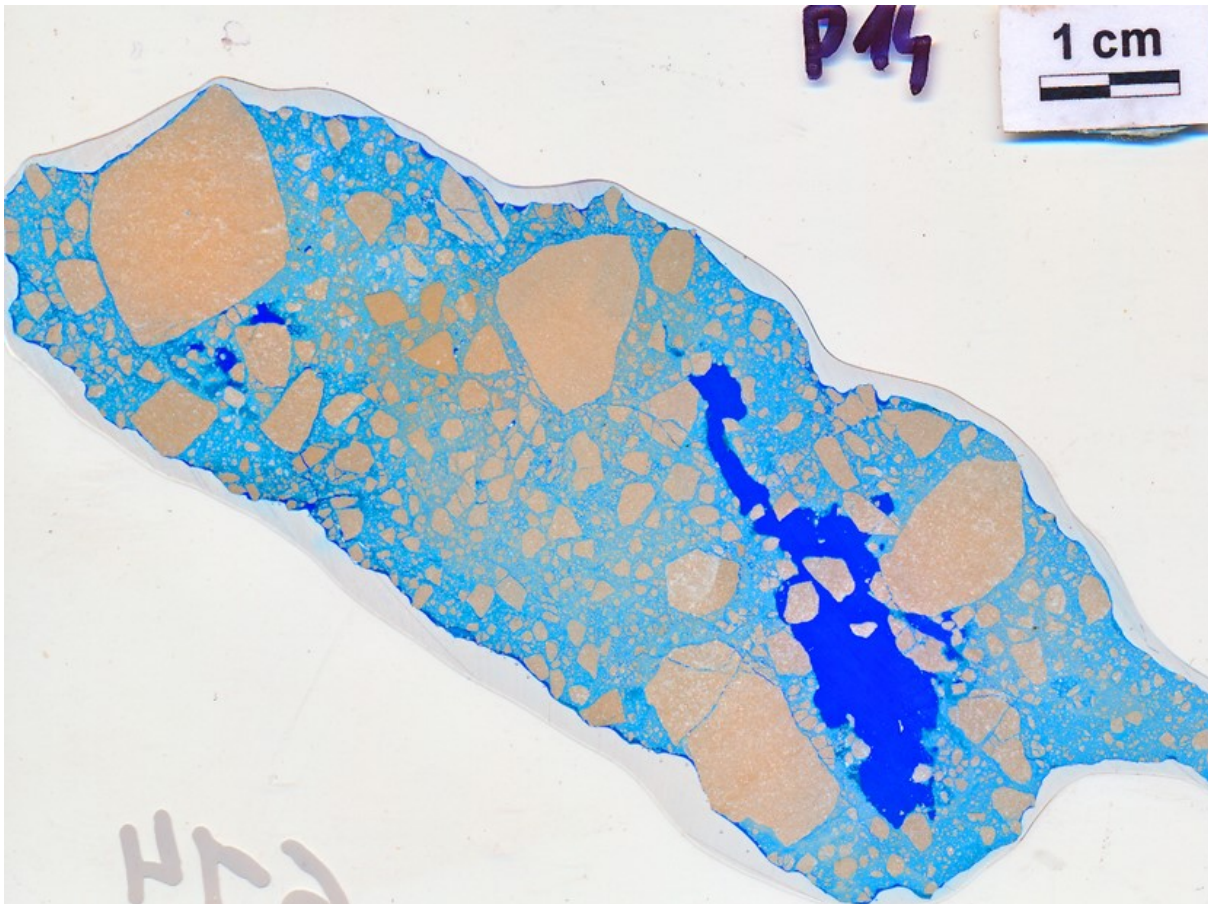


Figure 75: Highly porous fine cataclastic material separating subrounded to rounded protolith grains in a section prepared from sample 14. Protolith grains hardly show any fractures.

Distribution and carriers of porosity in the sample

The thin section shows a higher porosity than other cataclasites (the resin dyed it a deeper blue than other fine-grained cataclasites) carried foremost by the fine-grained matrix separating the big clasts swimming within it. All fragments in the section are rounded. Compared with other samples the protolith fragments show an interesting lack of fractures (Figure 75).

Matrix/protolith ratio

5-7.5 % in the mature cataclasite. 30 to 40% protolith in the intermediate cataclasite.

Protolith grain size, shape and orientation.

Pieces are subrounded to sub angular and partly quite big with diameters approaching 2 cm. Pieces are getting increasingly larger at a distance to the pss in the sample while angularity increases and sphericity decreases.

Other Observations

While the fine-grained matrix of the slip surface appears rough (most probably weathered) the clasts preserved the mirror-polished surface (Figure 76).

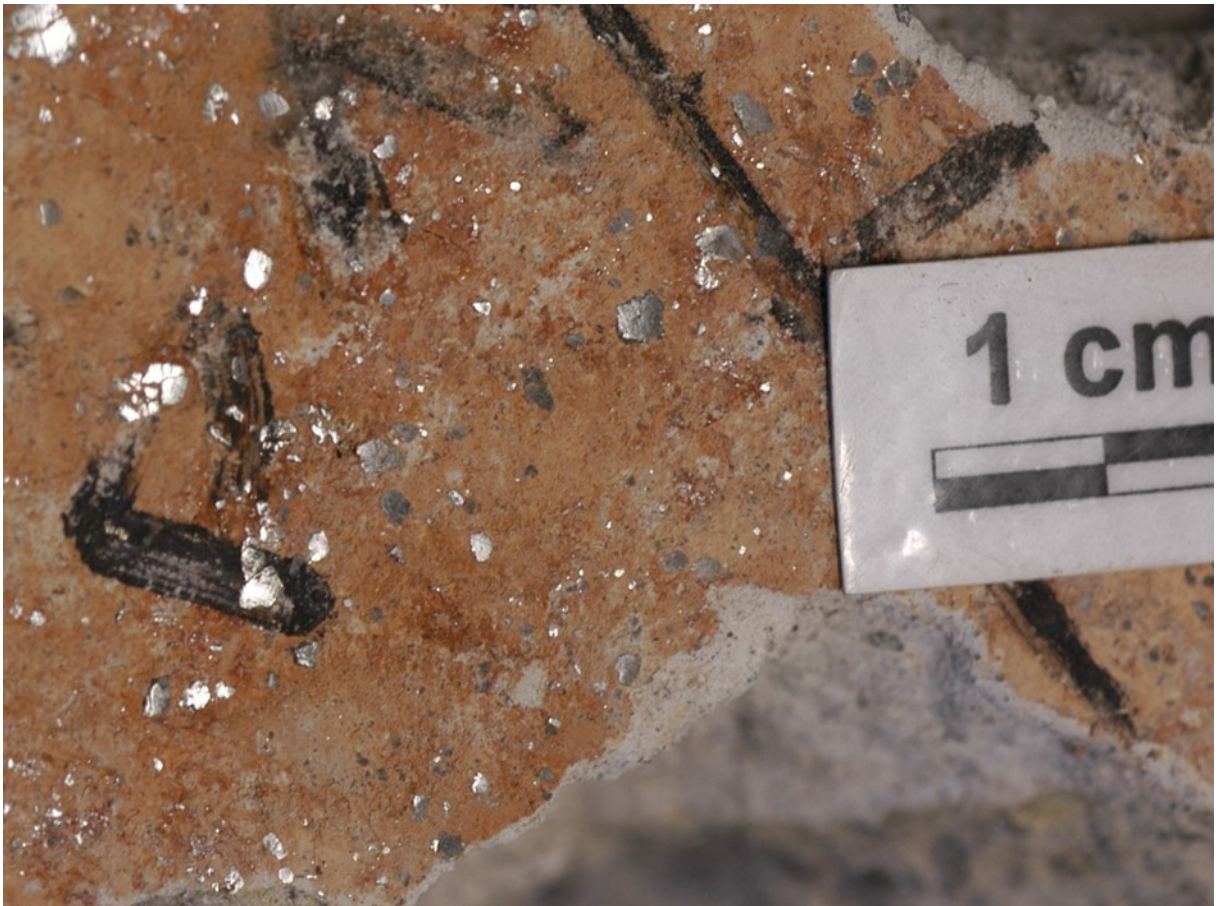


Figure 76: Mirror polished clasts in fine matrix roughened by weathering on the pss of sample 14. Note rusty discoloration of pss likely caused by meteoric waters felling iron-hydroxides.

5.2 Classification systems

In this chapter I want to discuss classification systems for fault rocks based on my experiences in Grossau.

5.2.1 The classic: Sibson 1977

The influential classification system of Sibson (Sibson, 1977), (see Table 8) classifies fault rocks in *cohesive* and *incohesive* rocks. He distinguishes them further by their *random* or *foliated fabric*, their *matrix content* and the dominance of *tectonic grain size reduction* vs. *dominance of grain growth* through recrystallization in the matrix.

		RANDOM - FABRIC	FOLIATED			
INCOHESIVE		FAULT BRECCIA (visible fragments >30% of rock mass)	?			
		FAULT GOUGE (visible fragments <30% of rock mass)	?			
COHESIVE	Glass/devitrified glass	PSEUDOTACHYLITE	?			
	NATURE OF MATRIX Tectonic reduction in grain size dominates grain growth by recrystallisation & neomineralisation	CRUSH BRECCIA FINE CRUSH BRECCIA CRUSH MICROBRECCIA	(fragments > 0.5 cm) (0.1cm < frags. < 0.5cm) (fragments < 0.1 cm)		0 - 10% 10 - 50% 50 - 90% 90 - 100%	PROPORTION OF MATRIX
		PROTOCATACLASITE	Cataclasite Series	PROTOMYLONITE	Mylonite Series	
		CATACLASITE		MYLONITE		
		ULTRACATACLASITE		ULTRAMYLONITE		
	PHYLONITE VARIETIES					
Grain growth pronounced	?		BLASTOMYLONITE			

Table 8: Fault rocks according to Sibson (1977, p. 192)

The problem with cohesion

Woodcock & Mort (2008) criticize the criterion of cohesion/primary cohesion. Their important point is that the reason of cohesion or lack thereof in a fault rock is hard to

determine in the field where rocks are exposed to the diverse effects of weathering and meteoric waters (e.g. secondary cohesion by post-faulting-cementation, loss of cohesion through weathering). Their reservations are well illustrated by the weathering and carstification of fault rocks in Grossau, which are likely linked to meteoric waters being acidified by biological processes in a region with coniferous forests (compare Reich et al. 2005, Thorley et al., 2015).



Figure 77: While soft enough at the surface to stick in a pencil, the cemented rock had to be chiseled to remove a sample after digging through around 40 cm of the “kakirite” to the “cataclasite” hidden beneath.

My observations at Grossau confirm that many so called “kakirites” are actually weathered cataclasites, as incohesive rocks gradually get more and more cohesive depending on the distance to the surface exposed to weathering (Figure 77). Sometimes the finer grain sizes get washed out forming a hard mass during dry weather below the fault while the coarser ones remain *in situ*.

Errors about the assessment of “cohesion” in fault rocks were also observed for apparently hard fault rock that was chiseled out for sampling in hot, dry weather. Some of the rocks crumbled up when getting into contact with water when trying to prepare blocks for thin sections.

Randomness

Woodcock & Mort (2008) also point out that the distinction between random and foliated fabric is not straight forward, as the fabric of many breccias is, at a closer look, not at all entirely random. At Grossau, preferred orientations, like for example of Riedel planes to the principal slip surface, tensile cracks at 45° with the slip surface commonly shape the fabric of the adjacent more or less brecciated rocks so I tend to agree with this argument too. Three-dimensional rocks fabrics looking entirely random in one cross-section may show preferred orientation of rock fragments in other sections. Most samples showed a more or less prominent layering with finer material near to the principal slip surface and coarser material away from it at a closer look in a section perpendicular to the slip surface. A fact that is not always obvious in the field, but would make a "cataclasite" a "mylonite" if strictly applied. The criterion therefor cannot be applied easily in the field.

5.2.2 Same, same but different: Implosion-, dilation and mosaic-breccias

Sibson (1986) describes breccias he sees as the results of implosion of void spaces created at releasing bends of faults (Figure 78). They are characterized by jigsaw puzzle textures, relatively well-sorted clasts and hydrothermal cement (see also chapter 5.2.1).

Tarasewicz et al. (2005) agree on the produced textures and widely also on the implosion mechanism but argue to call the rocks in question dilation breccias in order to make the category applicable also for rocks of similar fabric formed by slow/aseismic processes. They also observed that breccias with such fabric occurred not just at releasing bends, but also on a restraining bend and at locations with no obvious bend at all and define the term very generally: "*A dilation breccia can be defined as any fragmented rock in which there has been a net volume increase during formation.*" (Tarasewicz, et al., 2005 p.741). Wanting to use this term for field classification as well I agree with them and used the term "dilation breccia" with less genetic implications for the classification of rocks whenever they showed a jigsaw puzzle fit of clasts. Woodcock & Mort give a more precise differentiation into "*crackle, mosaic, and chaotic breccia – depending on how well the clasts fit together*" (Woodcock & Mort, 2008, p.438). They present two ternary classification systems classifying fault rocks by their content of clasts >2 mm, smaller clasts and matrix and cement or clasts >2 mm, cement and matrix and smaller clasts (Woodcock & Mort, 2008, pp.438-429). This classification system also has a problem: if one looks closer at fault rock samples from Grossau nearly all of them are heavily layered with a tendency of "coarsening outwards" in the direction perpendicular to the fault plane.



Figure 78: Fault rock thickening in a subhorizontal fault in Grossau: due to a releasing bend between overstepping faults?

In smaller faults (<1 m) this means changes of the classification within centimeters of fault rock, turning field classification of “the fault rock” for a certain fault into a rather tedious job, especially as the true geometries of the zones is often more complex than just layers parallel to the fault plane. Bigger, rather homogenous masses only develop in wider faults (with larger offset?) in Grossau, most smaller faults show the zoning from a coarse grained “damage zone” to an increasingly finer grained “core” mentioned above but also more complex patterns caused by multiple overstepping slip surfaces. Therefore, the differentiation between faults and fault systems seems mostly a matter of focus to me: The closer you look, the more internal complexity gets visible. Systems of overstepping slip surfaces seem to be quite common even in the dm scale, faults with one single, flat principal slip surface are not the rule. Slickenplanes are not necessarily flat planes, but often curved and meandering. Again, I would suggest, this is a result of their development between overstepping (micro-) faults, which again are likely caused by the onset of faulting on preexisting fractures from earlier deformation phases

I could also not agree with the simple explanation of dilation breccias by “mini-pull-aparts” as the most beautiful example of a breccia fitting the description of a “dilation breccia” stems from a flat of category 1 in the second level of the quarry, where no obvious bend is observable.

5.2.3 Classification system by fabric

Billi (2010) uses a similar system to the one introduced by Woodcock & Mort (2008) to classify low-PT Fault rocks in carbonate rocks. His terminology is less descriptive and more process-oriented, using terms that imply an evolution from “embryonic” over “intermediate” to “mature”. His classification was meant and is useful for microscopy work on carbonate fault rocks like the ones found in Grossau and so I used it when describing the thin sections. Billi’s (2010) embryonic fabric is distinguished from what I termed a dilational breccia in field and microscopy work by the very low matrix content. I used the term for puzzle like fabrics with protolith clasts clearly separated by matrix and/or cements with seemingly unrotated protolith grains.

Fabric	Embryonic	Intermediate	Mature
Location	Coarse breccia zones near boundary with damage zone	Breccia zones	Gouge zone/near principal slip surface
Grain Shape	Fractured, angular	Large Grains less angular than e. fabric	Large grains well rounded
Grain Contacts	“Jigsaw-Puzzle”	Partly in contact	Large grains rarely in contact
Grain Size	Large	Large grains	
Sorting	Well sorted with dominating large grains	Less well sorted than e. fabric	Poor. Small grains dominant
Matrix	Little to no matrix	Grains surrounded by fine matrix	Abundant Matrix

Table 9: Fault rock classification according to Billi (2010) used for the microscopic description of fault rocks in this work.

5.3 Processes of grain size reduction in fault rocks

Sibson (1986) distinguishes three types of mechanical brecciation-processes:

1. Attrition brecciation: produced by frictional wear along principal slip surfaces by both seismic and aseismic sliding
2. Distributed crush brecciation: micro-fracturing when slip is impeded by anti-dilational jogs or other barriers in situations with transpressional overstepping (e.g. at restraining bends)
3. Implosion brecciation producing high-dilation breccias: produced by the sudden creation of void space and fluid-pressure differentials at releasing bends (“dilational jogs” in the words of Sibson) during earthquake rupture propagation.

Fault geometries in the offset direction were hard to observe in most cases, so I cannot comment more on these ideas as I already did above for the dilation breccias. In Grossau I observed dilation breccias in faults with no obvious bends in the slip direction indicated by the dominant slickenline, so I would favor other explanations.

Jebrak (1997) gives an overview of the main processes of brecciation in hydrothermal vein deposits present in the literature at that time adding the possible influence of fluids beyond hydraulic fracturing to the fault-rock-producing mechanisms and distinguishes between chemical and physical mechanisms. He is mentioning, but not going in depth on highly interesting combinations of these: for example, when chemical processes at the tip of a fault allow for fault propagation before the stress field reaches the fail conditions of the unaltered rock.

Some of the processes presented by Jebrak, like hydraulic fluid assisted brecciation and possibly volume expansion by chemical reactions are likely explanations for dilation where fault geometry does not work:

Physical mechanisms	Chemical mechanisms
Tectonic comminution	Volume expansion
Wear abrasion	Volume reduction
Hydraulic fluid assisted brecciation	Selective dissolution
Critical fluid assisted brecciation	
Impact (e.g. of other clasts)	
Collapse	

Table 10: Brecciation mechanisms summarized by Jebrak (1997)

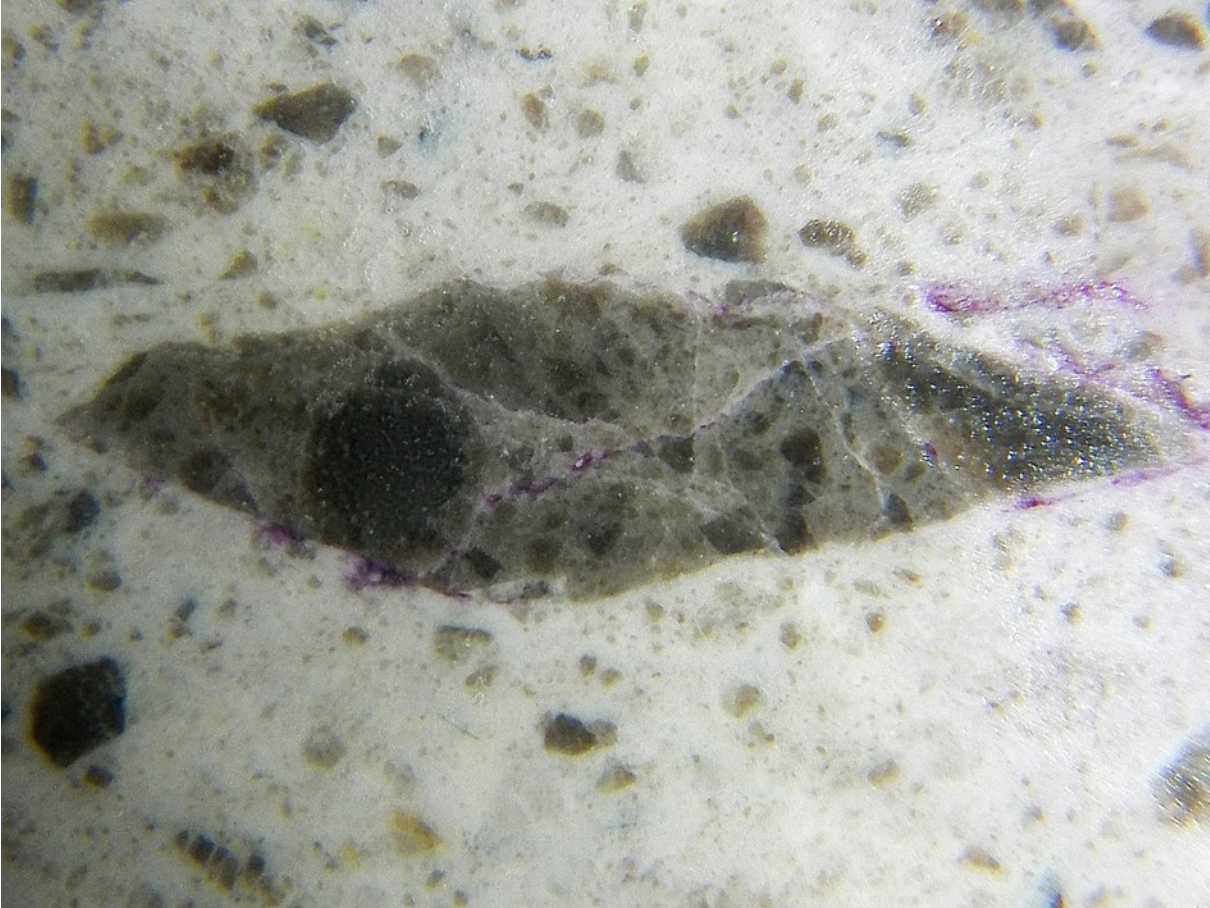


Figure 79: A 9.5 mm long lens shaped clast of reworked fault rock within mature cataclasite of sample 5.2

Yet something is missing in the “combined domain” in my opinion. Faults with repeated activity cementation processes could also affect the formation of fault rocks in later slip phases when already cemented fault rock is reworked in further faulting. This is the case with sample 5.2 where some of the rock fragments within the fault rock matrix are reworked cataclasites (Figure 79). In sample 7.2 the tips of propagating cracks show crystallized cement which would have to be fractured before further propagation of the crack (Figure 80).

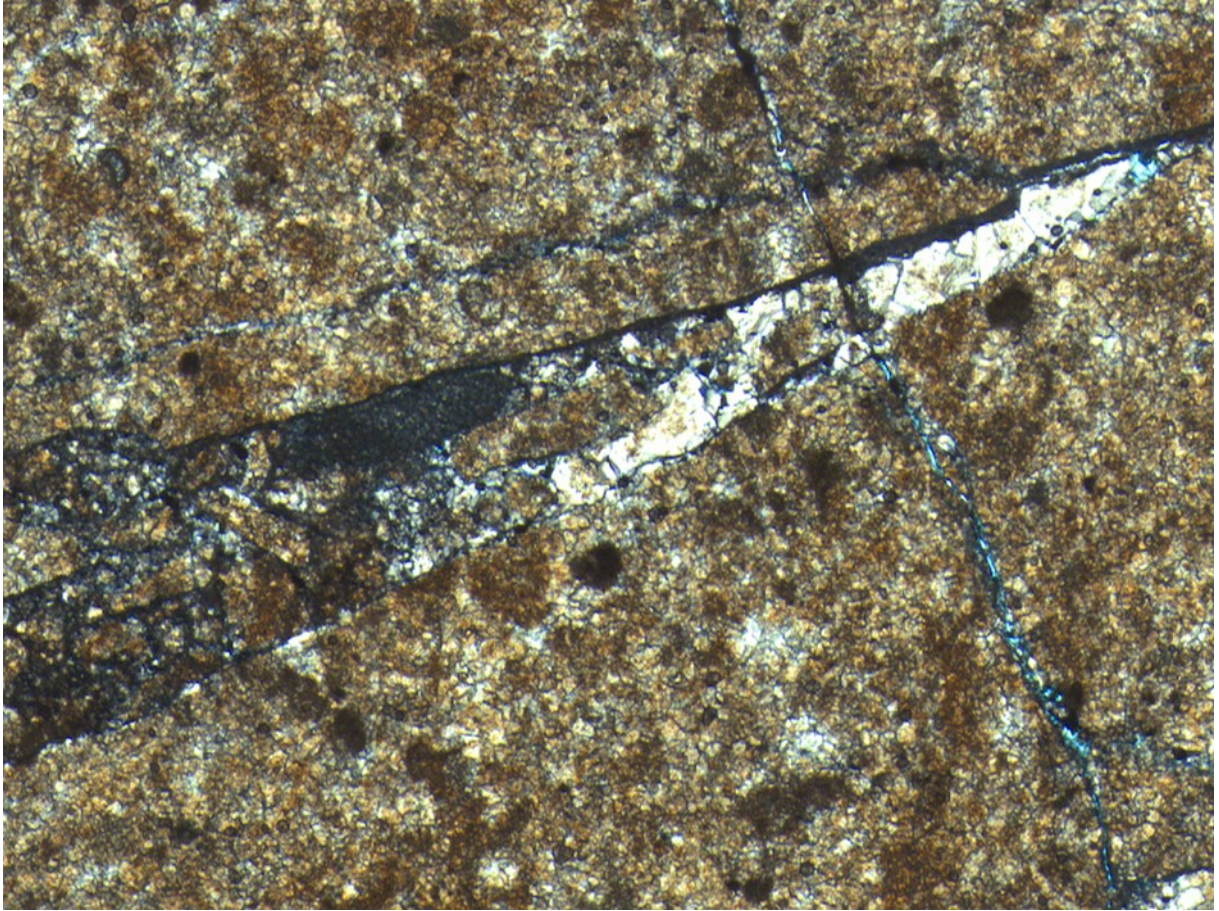


Figure 80: Sparitic dolomite cement at the tip of a tensile crack otherwise filled with cataclastic matrix and small grains (dark material). Long edge pf picture = 7mm.

Cementation on any kind of separating fracture surely affects the deformation behavior of the whole rock mass as experiments show (e.g. Patel & Shah, 2015).

Going into detail on the mechanisms at work in low-PT carbonate rocks Billi (2010) sees mostly cataclasis (in his definition: processes of fracturing and rotation) and rarely pressure solution at work.

He separates cataclasis into three main mechanisms (compare Billi, 2010, pp. 1397-1399): **Intragranular extension fracturing, chipping and shear fracturing**

1. **Intragranular extension fracturing:** Original structure of grains is fully destroyed by extensional fractures.

Variation 1: Fracturing along crystal borders with resulting monocrystalline fragments in a (secondary) dolomite made up of relatively coarse crystals.

Variation 2: Fragmentation of original grains in long, slender pieces by roughly systematic fractures which break again perpendicularly to their long axis producing angular pieces in the same order of magnitude than the original grains.

2. **Chipping:** Affects the edges and corners of original grains producing small fragments while tendentially rounding original grains and reducing their size only slightly.
3. **Shear fracturing:** Grains are cut into angular, elongated pieces by one to several shear fractures. Again, elongated pieces are often fragmented by extension fractures perpendicular to their long axis.

I could observe the structures described for the different processes (except for Variation1 of intragranular extension fracturing) but do not dare to argue about the processes proposed without observing their formation in some kind of model.

Pressure Solution

According to Billi (2010), intergranular stylolites like matrix stylolites and stylolites at grain contacts often are dilated because of sampling and handling. Intragranular stylolites (stylolites within protolith grains) are inherited from the previous history of the protolith and not part of the fault rocks history (Billi, 2010 p.1399). Intergranular stylolites, like the ones encountered in sample 7.2 from Grossau (Figure 81) that affect the cataclastic matrix are clearly part of the fault rocks history. A stylolite in dolostone is also pictured and described by James & Jones (2016, p. 401).



Figure 81: Lower edge= 1.5 cm Stylolites colored by iron hydroxides subparallel to the principal slip surface in a section of sample 7. 2 (false coloring of the picture to increase visibility of the stylolite)

In-situ processes

Schröckenfuchs et al. (Schröckenfuchs et al., 2015) argue for the importance of in-situ fracturing processes in early stages of fault rock formation and give evidence for processes rounding grains without rotation. A lot of their work depends on the use of EMS which was not used here, but structures like the obvious rounded but still unrotated grains in sample 1 (Figure 47) seem to show that in-situ grain diminution does play a role in the analyzed cataclasites.

5.4 Structural indicators for seismic slip on carbonate fault rocks

Schröckenfuchs et al. (2015) also give an overview of structures associated with seismic slip in carbonate fault rocks and the state of the discussion on their relevance in the literature, as none of the structures is widely accepted as seismic slip indicator.

1. **Mirror polished slickensides with truncated dolomite clasts:** Mirror polished slickensides like the one in were abundant in faults at Grossau. While some publications associate them with seismic slip rates after shear experiments (Fondriest 2013, who conducted their experiments on dolostone-gouges and thereby a material similar to the fault rocks from Grossau) others (Verberne et al., 2015, who worked with limestone or pure calcite-gouges) were also able to produce mirror polished surfaces at sub-seismic velocities. Mature cataclasites may lose their polish by weathering of the slip surface while it is preserved on the truncated clasts (see description of sample 14, p. 86).



Figure 82: Truncated clasts in sample 7.2, view on mirror-polished slickenside.

2. **Pulverized rock:** Rarely described from carbonate rocks, “*pulverized rocks (PR)* are a distinct type of fault rock that has been linked to coseismic damage. (...) PR experience little to no shear displacement and therefore preserve the internal mesoscopic structure of the protolith, with particles much smaller than the grain size of the host (...). Typically, the damage increases towards the fault core.” (Schröckenfuchs et al 2015, p. 68)
Asymmetric distribution of PR, parallel to the slipping zone is commonly observed in the field. A fact that may be related to the propagation of wrinkle-like ruptures along interfaces of different materials (Schröckenfuch et al 2015, p. 68) Following this definition, some of the fault rocks in Grossau could well

be (cemented) “pulverized rock”: Fault rocks showing little to no shear displacement but obvious grain size reduction were observed (see description of sample 11 below), as was in-situ grain size reduction (sample 1, Figure 47). Increasing grain size reduction towards the fault core/ slip surfaces is the rule for the faults in Grossau.

Moreover, as probable signs of liquefaction, Schröckenfuchs et al (2015) list the following candidates for seismic slip-indicators:

- 3. Bulbous protrusion of ultracataclastic material across sub-layer boundaries:** Cloudy distribution of fine, less porous material along of a former principal slip surface in sample 5.2 could fit this description (Figure 83): The trace appears as a plane formed by fine material parallel to the actual parallel slickenplanes bordering the sample. Under the microscope, it shows cloudy, bulbous shapes resembling structures from loose sediment liquefaction (e.g., Singh & Jain, 2007). Similar observations in cataclasites made up of sandstone protoliths within pelitic matrix were made by Brodsky et. al (2009) who compared them with flame structures in sediments (Brodsky et al. 2009, p.3-5).



Figure 83: The trace of a former principal slip surface in sample 5.2 (see also in the section of sample 5.2) is not a sharp plane at closer look: The fine grained, white material shows blurred and wavy structures that resemble such produced by liquefaction of loose sediments (length of lower picture edge is 2 cm).

4. **Clast distributions resembling imbrication:**

Microstructures that are in my opinion produced by en echelon fractures and in-situ rounding of grains like the ones in sample 1 (Figure 84) could be mistaken for imbrication.

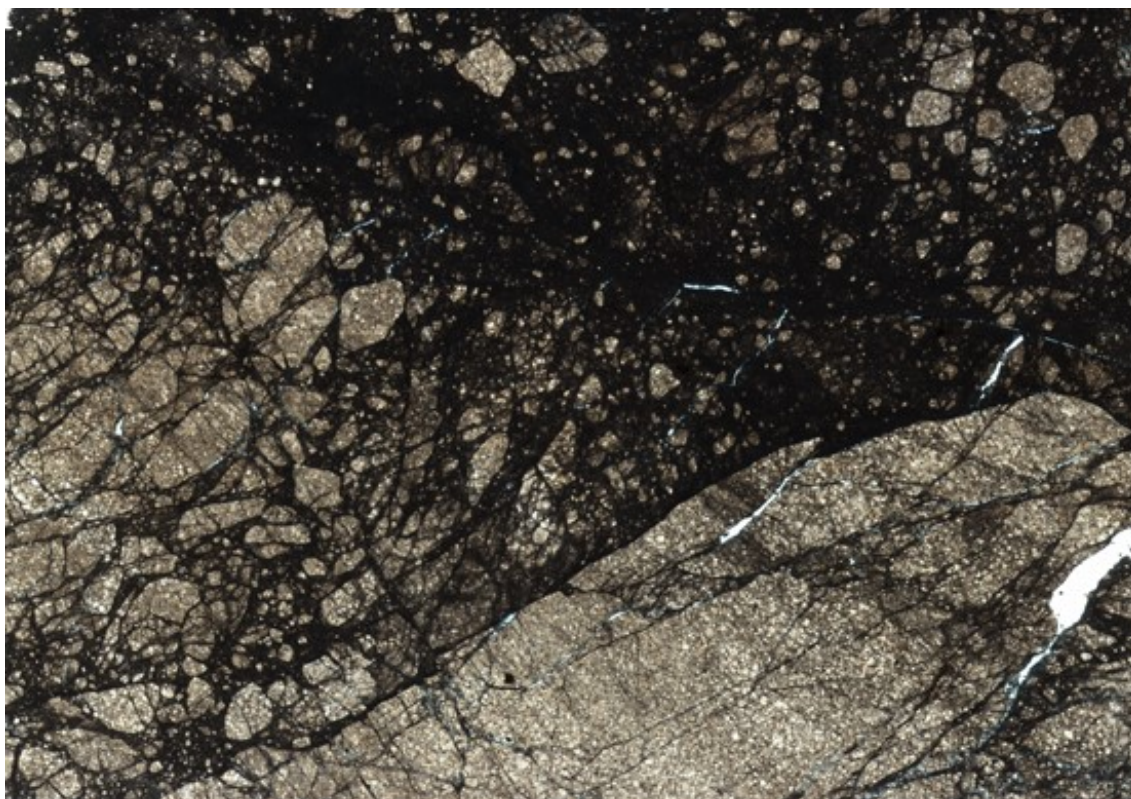


Figure 84: Lower edge is 3,2 cm. Preferred orientation of cracks (tensile cracks at roughly 45° to the PSS) and rounding of fragments produce an imbrication-like look in this section of sample 1.

I doubt the “stacking” is a result of fluidization in this case. Their orientation of roughly 45° with the fault plane lets me think they result from what Billi called “Intragranular extension fracturing” (Billi 2010): Tensile cracks fragment the pieces into long slender pieces (here at around 45° to the fault plane, so parallel to the shortening direction and in the expected orientation for tension gashes within a shear zone). A second series of cracks forms perpendicular to the long axis of this fragments. The remaining pieces are then in-situ rounded by a third process.

5. **Clasts with ultra-fine grained laminated coating:** Protolith grains in sample 10 show a dark rim in transmitted light that could well be such a coating. To be sure EMS would have to be employed.

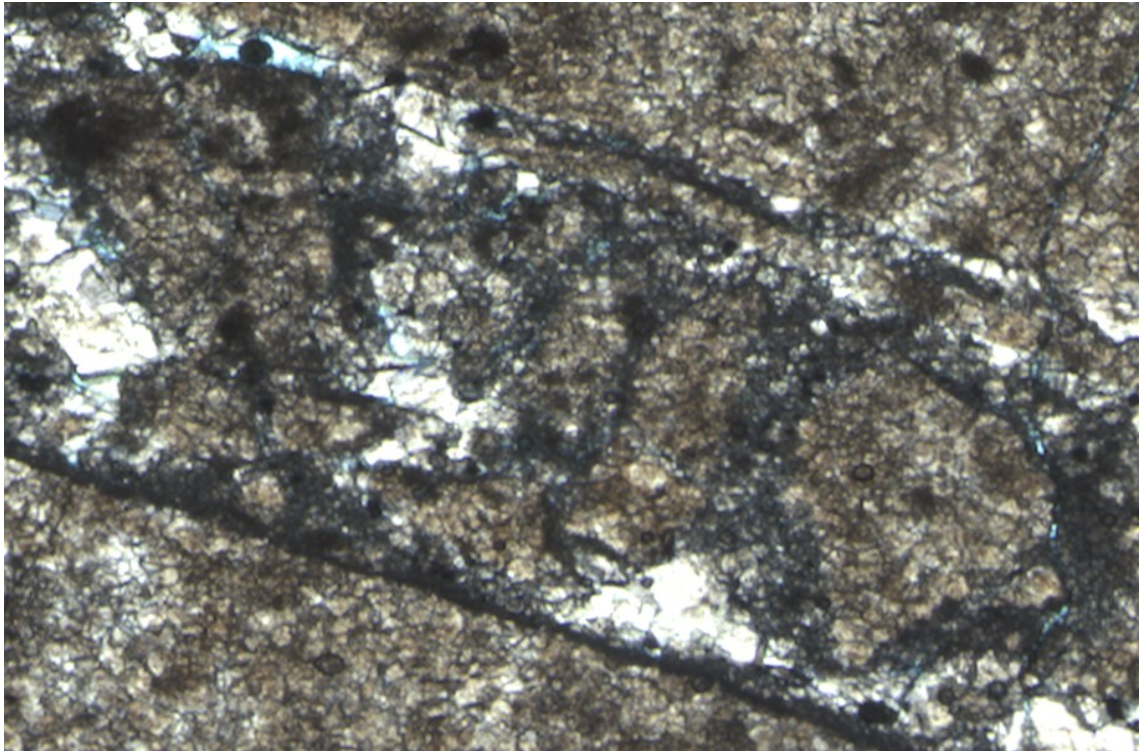


Figure 85: Fine grained rim? Picture width corresponds to 4mm.

The carbonate fault rocks of Grossau sampled for this work seem to show many of the structures (except imbricated clasts) discussed to be potentially indicative of seismic slip in carbonate fault rocks: mirror polished slickensides, structures pointing towards liquification, structures that fit the description of “pulverized rock” and possibly laminated grains.

6. Porosity Evaluation

6.1 *Effective porosity of rock samples*

6.1.1 **Effective porosity of fractured dolostones and fault rocks**

The visually distinguished FDCs coarsely correlate with the lab measurements on effective porosity increasing with fracture density. Values for FDC2 (2, median= 0.6%) overlap with FDC3 (3, median= 1.0%), while those for FDC 4 (4, median=3.5%) are clearly distinguished from the other two fracture density classes (Figure 86; porosity data are listed in the Appendix). The median value was used, as the median is less easily affected by outliers compared to the arithmetic or geometric mean. The calculation of median values for the different fracture density classes did not consider samples of dolostones with extremely high matrix porosity (pale red and “grainy” dolostones, see chapter 6.1.2).

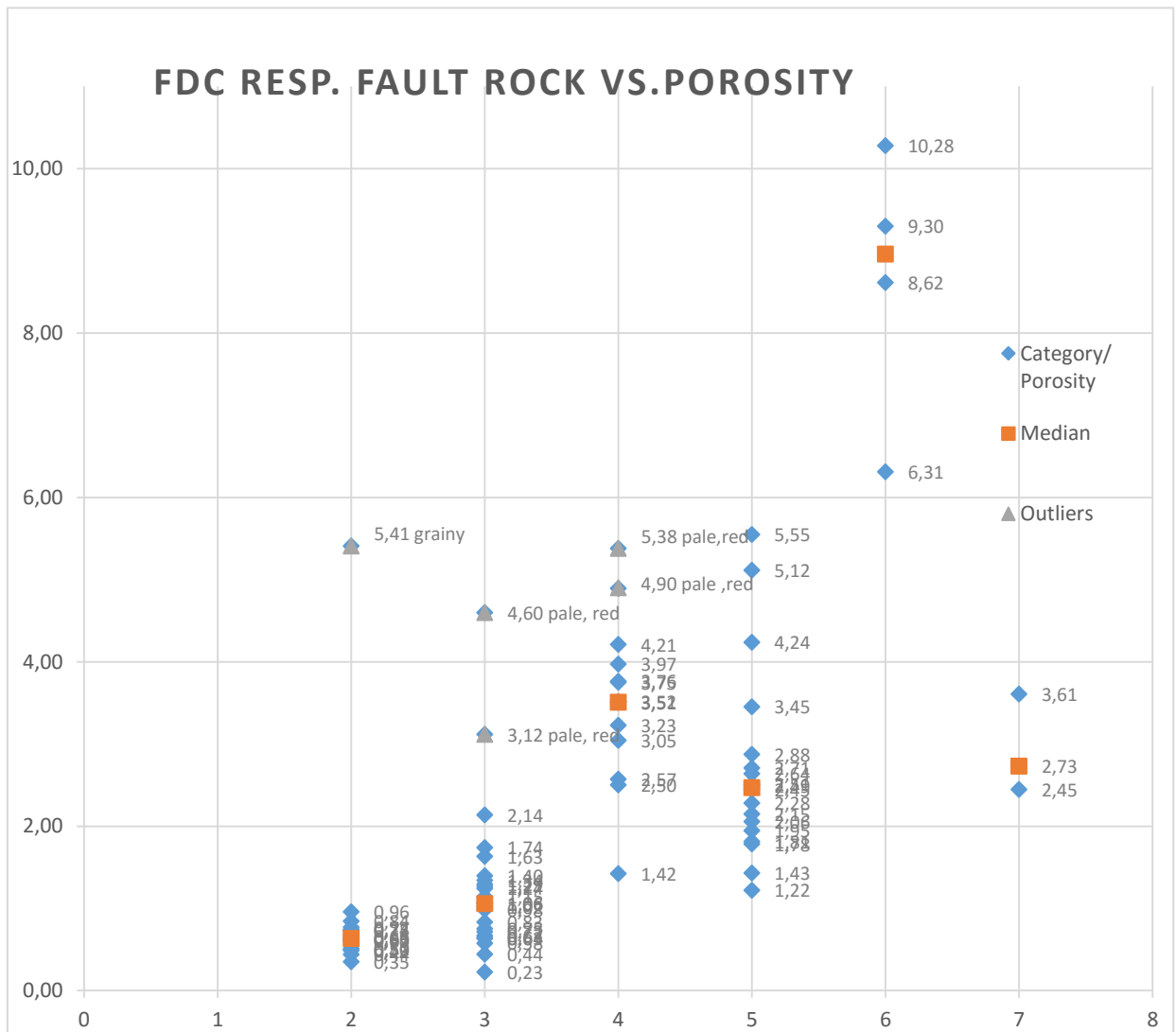


Figure 86: Effective porosities of dolostones with different fracture densities and fault rocks. Legend: FDC2, 3, 4= 2, 3, 4; cemented breccias=5, cataclasites=6, dilation breccias=7. Samples marked with grey symbols were not considered for median calculation (see text for discussion).

Well cemented embryonic to intermediate cataclasites (5) collected near fault cores show porosities in the range of FDC4 and 3 while (ultra-) fine grained mature cataclasites (6) of white, chalky appearance found in the fault cores show the highest porosities of the rocks measured. Dilation breccias plot near the cemented breccias. Samples of pale, rusty red colored beds in FDC3 and FDC 4 show high porosity for their respective FDC and quite similar porosity compared with each other, as does a sample of an unusual grainy, coarse crystallized dolomite bed in FDC2 which shows a high inter-crystalline porosity even when looked at with a 10x hand magnifier.

6.1.2 High porosity facies identified during measurements

The outliers (named “pale, red” and “grainy” in the plot in Figure 86) clearly belong to two different facies types of the dolostone which are easily identifiable in the field.

6.1.2.1 Pale, reddish discolored dolomite of high fracture density

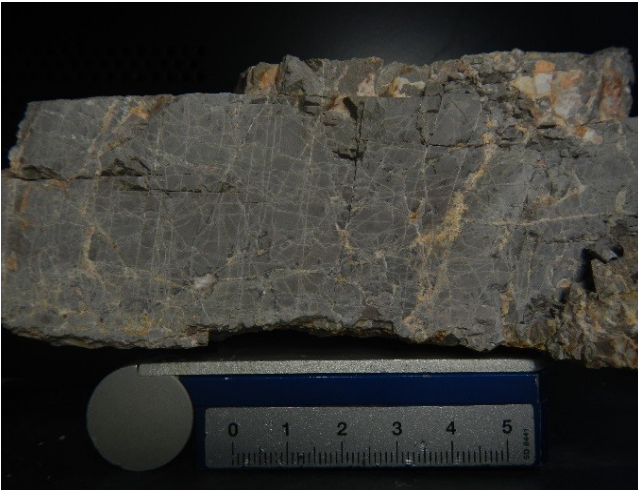


Figure 87: A sample of a finely fractured pale-reddish bed



Figure 88: Moss growing on a moist, finely fractured reddish bed after weeks of hot, dry weather in an otherwise bone-dry quarry in August 2015. Base of the NE quarry wall.

One Group of outliers are pale dolomites, which appear reddish due to iron-hydroxide precipitates, with, even for Grossau-dolomite, highly abundant, sometimes partly cemented fractures. They typically show sections with lamination with partly or fully cemented fenestrae. Their fine fracture networks produce exceptionally high (for samples from Grossau) effective porosity values in the range of 3.12 to 5.38 % porosity. For one instance, moss could be observed growing on a water soaked bed in the eastern part of the quarry after weeks of dry, hot weather, an indicator for these beds being also highly permeable and preferred pathways for water/fluids (see Figure 88).

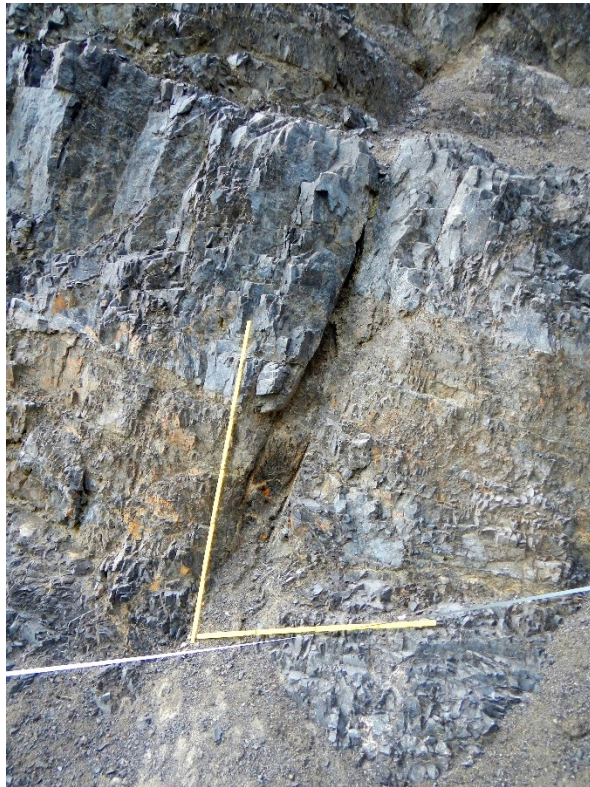


Figure 89: Fault widening at intersection with reddish bed. Also, observe contrast in fracture density between reddish and grey beds.



Figure 90: Increasing width of fault rock at intersection with reddish bed.

These beds repeatedly showed a distinctively different deformation behavior when intersected by faults, with the faults widening where they intersect those beds (see Figure 89 and Figure 90 above).

6.1.2.2 Grainy dolomite with high matrix porosity

The second easily identifiable rock type with high porosity are relatively coarse-grained rock made up of tiny dolomite crystals reminding of fine brown sugar (referred to as “grainy” in the plot in Figure 86). It showed an exceptionally high matrix porosity of 5.41%. The samples are nearly unfractured. It was sampled only once and not found during the work on the porosity profile and thereby did not play a role for the porosity modeling.



Figure 91: Sample of sugar-grained stone



Figure 92: A closer look reveals large pores between the crystalline grains even to the unaided eye.

6.2 Porosity evaluation for rock mass without fault rocks

The 42 m long lithostratigraphic profile (see chapter 2.5) done to assess the porosity of the fractured matrix without faults shows the following distribution of fine clastic sediments (“Keuper”), the three FDCs and the heavily fractured, iron-stained layers (Table 11). The spongy, porous sugar grained dolomite identified in the porosity measurements was not encountered within the profile.

The highly porous iron stained layers were assigned their own porosity class (pale red high-porosity dolostones; see chapter 6.1.2.1, HiPo below) based on the median values of porosity measurements from samples of these beds.

	Proportion in lithostratigraphic Profile [%]	Median eff. Porosity [%]
Keuper	0.12	0.00
FDC2	1.48	0.63
FDC3	83.25	1.06
FDC4	8.37	3.51
HiPo	6.79	4.75
Sum	100.00	Weighted Average: 1.51%

Table 11: Porosity evaluation for the rock mass without fault rocks.

Using this estimate together with the lab determined median values of porosity for the respective rock classes this would give a weighted average of 1.51% for the fractured rock mass without the fault rocks and damage zones.

6.3 Porosity of rock mass including fault rocks

The proportion of fault rock in the rock mass is assumed equal the proportion of fault rock in the scanlines.

Visible fault length was either determined by outcrop size, or rarely by intersection with other faults (or even then usually with little offset). Therefore, the length data was heavily truncated and censored and was omitted from the porosity estimation. I am well aware that this means to set equal 1 D –Proportion Data [m/m] with 3D –Proportion Data [m³/m³] without any real information on fault lengths, changes in fault rock thickness, 3-D fault distribution patterns etc., but there is no way to acquire this information from the outcrop.

As fault rock thickness data was recorded as fault rock *true thickness* the calculation uses the projected right angle distances of scanline-lengths for each fault category to assess the abundance of fault rock. (Had the data been acquired in the form of apparent fault rock thickness per meter of scanline the calculation would simply be the proportion of fault rock to scanline length.)

A positive side effect of this complication in computing is that the calculation also provides information on the proportion of fault rock that each category of faults contributes to the total fault rock volume (Table 12). Effective porosity data for cemented fault rock could be determined using the lab-method described above. Data for semi- or incohesive fault rock could not be produced this way, as any kind of sampling tried would destroy the packing of the sediment and any “true” information on the

in-situ material. No more efforts were undertaken to determine exact porosity values for these semi- or incohesive fault rocks as they are mostly weathering products with smaller grain sizes washed out and not expected to occur in reservoirs at depth. Instead, a porosity range of 5-20% based on literature values for the effective porosity of clastic sediments with a mixture of clay, gravel and sand sized particles was used. Hölting & Coldewey (2013, p. 14) write of 20- 25% effective porosity for sandy gravel, with values decreasing rapidly with reduced grain size to 5-10% for sandy silt and 2-5% for clay. Fetter (2000, p. 75) writes of 20-35% “porosity” for a mix of gravel and sand, while of 33-60% for clay, likely meaning total porosity but not clearly stating this. The clay sized particles in the fault rocks are rarely clay minerals with their electrostatic charge causing higher total porosity (and lower effective porosity by means of their huge surface). So, their influence has to be treated differently. Homogenization of grain size in fine fault rock though is likely to raise total porosity (while smaller grain sizes still reduce effective porosity by means of higher surface). To assume the lowest value for sandy gravel, 20% seems to be a proper upper value to use in a conservative estimate of effective porosity as most uncemented fault rocks seemed to consist of a lightly silty sand and gravel mixtures, though values for effective porosity could get even lower if the proportion of fine material was underestimated because these were washed out. In this case assuming a lowest value of 5%, that is the upper level of effective porosity for clay and the lower level for sandy silt after Hölting & Coldewey (2013) seems correct as sand and gravel sized particles were always present. Also, the value of 5% corresponds to the average effective porosity of unweathered cemented fault rocks encountered in the quarry Grossau.

Fault Category	Total Fault Rock true width	Uncemented fault rock true width	Cemented breccia true width	Cataclasite true width	Intensely fractured dolostone (FDC4) true width	Dilatation -breccia true width	Sampled Normal Distance (SND)
Category 1 [cm]	45.00	12.50	1.00	0.50	31.00	0.00	83.81 [m]
Category 2 [cm]	157.00	37.50	23.00	0.50	96.00	0.00	126.28 [m]
Category 3 [cm]	472.00	155.00	51.50	2.50	263.00	0.00	170.91 [m]
Category 4 [cm]	303.70	51.00	42.50	4.20	201.00	5.00	164.90 [m]
Category 5 [cm]	23.00	16.50	3.00	0.50	3.00	0.00	162.21 [m]
Category 6 [cm]	59.00	26.00	6.00	0.00	27.00	0.00	170.15 [m]
Category 7 [cm]	15.50	15.50	0.00	0.00	0.00	0.00	147.36 [m]

Fault Category	Total Fault Rock true width	Uncemented fault rock true width	Cemented breccia true width	Cataclasite true width	Intensely fractured dolostone (FDC4) true width	Dilatation-breccia true width	Sampled Normal Distance (SND)
Category 1 [% SND]	0.54	0.15	0.01	0.01	0.37	0.00	
Category 2 [% SND]	1.24	0.30	0.18	0.00	0.76	0.00	
Category 3 [%SND]	2.76	0.91	0.30	0.01	1.54	0.00	
Category 4 [%SND]	1.84	0.31	0.26	0.03	1.22	0.03	
Category 5 [%SND]	0.14	0.10	0.02	0.00	0.02	0.00	
Category 6 [%SND]	0.35	0.15	0.04	0.00	0.16	0.00	
Category 7 [%SND]	0.11	0.11	0.00	0.00	0.00	0.00	
Sum [%SND]	6.98	2.02	0.81	0.05	4.07	0.03	
	Rock Mass without fault rocks	Incohesive fault rocks	Cemented breccia	Cataclasite	F.FDC 4	Dilatation-breccia	
Proportion [% total rock volume]	93.02	2.02	0.81	0.05	4.07	0.03	
Median effective Porosity [%]	1.51	5-20.00 ⁽¹⁾	2.47	8.96	3.52	2.73	
Prop. *Por.	140.46	40.44	1.99	0.48	14.31	0.08	
Effective Porosity of rock mass including fault rocks [%] (weighted arithmetic average)						1.67 -1.98	

Table 12: All data from the scanlines and porosity measurements. ⁽¹⁾ The value of 5-20% for the effective porosity of incohesive fault rocks is an estimate based on literature data on mixes of sand, gravel and clay (Fetter 2000, p. 75, Hölting & Coldewey 2013 p. 14, see discussion above this table)

Discussion of total porosity evaluation

The value of 1.67- 1.98% effective porosity derived for the dolostone rock mass including fault rocks should be regarded as a “conservative estimate”. Leaving aside the estimated value of 5- 20% for the uncemented fault rocks as being uncertain, sampling problems tend to cause a bias towards lower porosity values. This is partly due to reasons already given in the discussion of the porosity values in chapter 0: even for individual samples of two kilos the sample size was not large enough to sample a representative share of fractures in FDC 2 and parts of FDC 3. Another cause for underestimation was the field assessment of the fracture density classes: If in doubt about classification, the lower value was used systematically. Thus, the value range can be regarded as a “conservative estimate”.

This range of 1.67 to 1.98% fits within the range of porosity values documented for heterogeneous dolomites rich in clastic sediments found in deep reservoirs of the Hauptdolomit Formation (4000-6300m) of 0-4% (Nicol et al. 1991 p. 182). As fracture porosity and permeability generally decrease with depth (compare Singhal & Gupta 2010, p.13) this doesn't sound promising for rocks equivalent to those from Grossau, as reservoirs of less than 5% effective porosity rarely produce economically (Ladwein & Sauer 1993, p.27).

7. Conclusions

The lithology of the Hauptdolomit Formation in the quarry Grossau with its various lithofacies and relative abundance of thin siliciclastic layers is interpreted as sedimentation in a distal part of a shallow-marine lagoon repeatedly affected by the sedimentation of clay-sized clastic sediments. With its repeated occurrence of siliciclastic layers it resembles rocks of the Hauptdolomit Formation described from the Göller Nappe in the Vienna Basin but is a little bit more “colorful” in terms of the variation of dolostone facies. Dolostones display different intensities of fracturing which are well reflected by effective porosities. Rocks with different fracture intensities expressed by fracture density classes show distinct effective porosities with median values of 0.6% (closely jointed), 1.0% (very closely jointed) and 3.5% (extremely fractured dolostone). Most of the rock mass consists of very closely jointed dolostone (c. 83%).

Clay layers (“Keuper intercalations”) within the rock mass are thought to have little influence on the reservoir properties as these layers are mostly very thin (millimeter to sub-millimeter range) and breached by abundant faults and fractures. The layers further act as detachment horizons causing a relative abundance of thrust flats which partly contain fault rocks with up to several meters thickness and increased porosity.

The most abundant faults in numbers and fault rock volume are steep NNW-SSE striking faults closely followed in rank by steep WNW-ESE striking faults, the latter likely belonging to the locally important Merkenstein-fault system. The faults of these two categories and of a third, less common group of NW striking and NE dipping faults probably enhance permeability of the rock mass in NW-SE direction. This interpretation is supported by karst features visible in the northern quarry wall which are controlled by these faults.

Many of the faults show mirror polished slickensides with truncated clasts, in situ grain size reduction indicative for pulverized rock and in one case signs for liquefaction in a fault rock could be found under the microscope. All of these are discussed as indicators of seismic events as these lines are written.

The cemented fault rocks generally show high effective porosities of up to 10% (median values of about 9% for cataclasites and 2.5% fault breccias, respectively). However, they are expected to have low permeability due to the small diameter of pores and pore necks. These fault rocks may accordingly act as local barriers. However, as fault rocks are frequently bypassed by younger faults and fractures they are unlikely to form continuous seals at a larger scale.

The quantitative assessment of rock types, fault frequencies, and fault orientations together with measurements of the effective porosity of different rocks allow for a rather precise calculation of the bulk porosity of the rock mass of the Hauptdolomit Formation exposed in the quarry Grossau. The calculated effective porosity ranges

from 1.7 to 2.0%. The values are derived from conservative assumptions. The range reflects different assumptions for the uncemented fault rocks, which contribute a significant volume of the fault rocks. The lack of cementation of these rocks is regarded as a result of weathering. An effective porosity of 1.7% may apply to unweathered reservoirs.

8. Literature

- Billi, A., 2010. Microtectonics of low-P low-T carbonate fault rocks. *J. Struct. Geol.* 32, pp. 1392-1402.
- Brodsky, E.E., Rowe, C.D., Meneghini, F., Moore, J.C., 2009. A geological fingerprint of low-viscosity fault fluids mobilized during an earthquake. *Journal of Geophysical Research* Vol. 114.
- Decker, K., Peresson, H., Hinsch, R., 2005. Active Tectonics and quaternary basin formation along the Vienna Basin Transform fault. In: *Quaternary Science Reviews* 24, pp. 307-322.
- Decker, K. 2007. Dolomite fracture and fault analysis. Unpublished report for OMV Austria, Vienna
- Fetter, C.W. 2000. *Applied Hydrogeology*. 4 ed. Pearson.
- Flügel, E. 1978. *Mikrofazielle Untersuchungsmethoden von Kalken*. Springer
- Fondriest, M., Smith, S.A.F., Candela, T., Nielsen, S.B., Mair, K., Di Toro, G., 2013. Mirror-like faults and power dissipation. *Geology* 41 (11): 1175-1178.
- Linzer, H.G., Ratschbacher, L., Frisch, W. (1995) Transpressional collision structures in the upper crust: the fold-thrust belt of the Northern Calcareous Alps. *Tectonophysics*, 242, pp. 41-61.
- Frisch, W., Gawlick H. J., 2001. Die tektonische Gliederung der Kalkalpen im Salzkammergut im Lichte der historischen Entwicklung. *Berichte der Geologischen Bundesanstalt* 56, pp. 41-43.
- Frisch, W. Gawlick H.J, 2002. The nappe structure of the central Northern Calcareous Alps and its disintegration during Miocene tectonic extrusion—a contribution to understanding the orogenic evolution of the Eastern Alps. *International Journal of Earth Sciences*. Vol. 92, Issue 5, pp. 712-727.
- Hölting B., Coldewey W.G., 2013. *Hydrogeologie*. 8ed. Springer
- James, N., Jones, B., 2016. *Origin of carbonate sedimentary rocks*. Wiley.

Lee, E.Y., Wagreich, M., 2016. Polyphase tectonic subsidence evolution of the Vienna Basin inferred from quantitative subsidence analysis of the northern and central parts. *International Journal of Earth Sciences*, Volume 106, Issue 2, pp. 687–705.

Ney, P., 1986. *Gesteinsaufbereitung im Labor*, Enke, Stuttgart

Nicol, S.A., 1991. Elektrofazies, Geochemie und Mikrofazies ausgewählter Triasschichten (Nördliche Kalkalpen) im Untergrund des Wiener Beckens. *Mitteilungen der österreichischen geologischen Gesellschaft*, Band 84, pp. 161-183.

Patel, M.B., Shaw M.V. 2015. Strength Characteristics for Limestone and Dolomite Rock Matrix using Tri-Axial System. *International Journal of Science Technology and Engineering* Vol. 1/ 11 pp. 114-124

Petit, J.P., 1987. Criteria for the sense of movement on fault surfaces in brittle rocks. *Journal of Structural Geology* Vol. 9, No. 5/6 pp. 597-608.

Peresson, H. and Decker, K., 1997. The Tertiary dynamics of the northern Eastern Alps (Austria): changing palaeostresses in a collisional plate boundary. *Tectonophysics* 272, pp. 125-157.

Piller, W., Decker, K. and Haas, M., 1996. Sedimentologie und Beckendynamik des Wiener Beckens. *Berichte der Geologischen Bundesanstalt*, Band 33, pp. 1-41.

Reich, P.B., Oleksyn J., Modrzynski J., Mrozinski, P., Hobbie, S.P., Eissenstat, D.M., Chorover, J., Chadwick, O.A, Hale C.M. Tjoelker M.G. 2005. Linking litter calcium, earthworms and soil properties: a common garden test with 14 tree species. *Journal of Ecology Letters*, Vol 8, Issue 8, pp. 811-818.

Root, K.G. 1990. Extensional duplex in the Purcell Mountains of southeastern British Columbia In: *Geology*, 18, I5, p. 419.

Salcher B.C., Meurers B., Smit J., Decker K., Hölzel M., Wagreich M. 2012. Strike-slip tectonics and Quaternary basin formation along the Vienna Basin fault system inferred from Bouguer gravity derivatives In: *Tectonics* 31, Issue 3, pp.1-20.

Schopper, T., 1991. Strukturgeologische Untersuchungen als Hilfe für die tektonische Deutung des Bewegungsmechanismus des Wiener Beckens. *Mitteilungen der österreichischen geologischen Gesellschaft*, Band 84, pp. 101-134.

Schröckenfuchs, T., Bauer H., Grasemann B., Decker K., 2015. Rock pulverization and localization of a strike-slip fault zone in dolomite rocks (Salzach-Ennstal-Mariazell-Puchberg fault, Austria). *Journal of Structural Geology* 78, pp. 67-85.

Sibson, R.H., 1977. Fault rocks and fault mechanisms. *J. Geol. Soc.* 133, pp. 191-213.

Sibson, R.H., 1986. Brecciation processes in fault zones: inferences from earthquake rupturing. *Pure Appl. Geophys.* 124, pp. 159- 175.

Singh, S., Jain, A.K. 2007. Liquefaction and fluidization of lacustrine deposits from Lahaul-Spiti and Ladakh Himalaya: Geological evidences of paleoseismicity along active fault zone. *Sedimentary Geology* 196, pp. 47–57.

Singhal, B., Gupta, R. ,2010. *Applied Hydrogeology of Fractured Rocks* (2nd ed.). Dordrecht: Springer.

Stern, G., Wagreich M., 2013. Provenance of the Upper Cretaceous to Eocene Gosau Group around and beneath the Vienna Basin (Austria and Slovakia): *Swiss Journal of Geosciences* 106/3, pp. 505-527.

Stüwe K., Schuster R. 2010 Initiation of subduction in the Alps: Continent or ocean? *Geology* 2010, 38, pp.175-178.

Tarasewicz, J.P.T., Woodcock, N.H., Dickson, J.A.D., 2005. Carbonate dilation breccias: examples from the damage zone to the Dent fault, northwest England. *Geol. Soc. Am. Bull.* 117, pp. 736-745.

Thorley, R.M.S, Taylor L.L. Banwart A.S., Leake J.R., Beerling D.J., 2015. The role of forest trees and their mycorrhizal fungi in carbonate rock weathering and its significance for global carbon cycling. *Plant, Cell and Environment*, Band 38, pp. 1947-1961.

Tollmann, A., 1966. Tektonische Karte der nördlichen Kalkalpen. 1. Teil: Der Ostabschnitt. *Mitteilungen der österreichischen geologischen Gesellschaft*, Band 59 pp. 231-253.

Verberne, B.A., Spiers, C.J., Niemeijer, A.R., De Bresser, J.H.P., De Winter, D.A.M., Plümper, O., 2014. Frictional properties and microstructure of calcite-rich fault gouges sheared at sub-seismic sliding velocities. *Pure Appl. Geophys.* 171, pp. 2617-2640.

- Wachtel, G. and Wessely, G., 1981. Die Tiefbohrung Berndorf 1 in den östlichen Kalkalpen und ihr geologischer Rahmen. Mitteilungen der österreichischen geologischen Gesellschaft, Band 74/75, pp. 137-165.
- Wang, X. (2005). Stereological Interpretation of Rock Fracture Traces on Borehole Walls and Other Cylindrical Surfaces. Blacksburg.
- Weber J., Vrabec M., Pavlovčič-Prešeren P., Dixon T., Jiang Y., Stopar B. 2010. GPS-derived motion of the Adriatic microplate from Istria Peninsula and Po Plain sites, and geodynamic implications. *Tectonophysics* 483, pp.214-222.
- Wessely, G., 1993. Der Untergrund des Wiener Beckens. In: F. Brix and O. Schulz, Hrsg. Erdöl und Erdgas in Österreich. Vienna: OMV, pp 249-280.
- Wessely, G., 2006. Geologie der österreichischen Bundesländer: Niederösterreich. Wien: Geologische Bundesanstalt.
- Wessely, G., Coric S., Rögl F., Draxler I., Zorn I., 2007. Geologie und Paläontologie von Bad Vöslau (Niederösterreich). *Jahrbuch der geologischen Bundesanstalt*, Band 147, pp. 419-448.
- Wessely, G., 2008. Kalkalpine Schichtfolgen und Strukturen im Wienerwald. *Journal of Alpine Geology*, Band 49, pp. 201-241.
- Wessely, G.; 2013. Schichttypen und Strukturen in den östlichen Kalkvorpalen. Handout. Arbeitstagung der geologischen Bundesanstalt 2013 Melk, pp. 15-19.
- Woodcock, N.H, Mort, K. 2008: Classification of fault breccias and related fault rocks. *Geol. Mag.* 145 (3), 2008, pp. 435–440.

Orthophotos:

Basemap Austria: <https://www.basemap.at/>

NÖGIS: Geo-Data Server of lower Austria providing historical aerial photos.

<http://atlas.noe.gv.at/>

Normed Test procedures used:

ÖNORM B3121: Testing of natural stone; density, apparent density, bulk density

ÖNORM EN 1936: Determination of real density and apparent density, total and open porosity

9. Appendix

FDC	Lithology	Sample	md				mh				ms				Density [g/cm ³]	Open Porosity
			24h	48h	MW	%	24h	48h	MW	%	24h	48h	MW	%		
2		P25	2405,1	2405,9	2405,50	0,03	1561	1560,9	1560,95	0,01	2409,9	2409,8	2409,85	0,00	2,83	0,51
2		P26	1368	1368,3	1368,15	0,02	887,9	887,8	887,85	0,01	1371,3	1371,4	1371,35	0,01	2,83	0,66
2	Grainy, highly porous	P27	1896	1896,7	1896,35	0,04	1167,1	1167,7	1167,40	0,05	1937,8	1938,3	1938,05	0,03	2,46	5,41
2		P28	2547	2547,5	2547,25	0,02	1653,7	1653,8	1653,75	0,01	2553,6	2552,3	2552,95	0,05	2,83	0,63
2		P29	1451,4	1451,8	1451,60	0,03	942,5	942,6	942,55	0,01	1455,6	1455,5	1455,55	0,01	2,83	0,77
2		P30	1654,4	1655	1654,70	0,04	1073,9	1073,7	1073,80	0,02	1657,5	1657,7	1657,60	0,01	2,83	0,50
2		P31	1951,5	1951,9	1951,70	0,02	1265,5	1265,6	1265,55	0,01	1956,1	1956	1956,05	0,01	2,83	0,63
2		P32	2117,8	2118,4	2118,10	0,03	1373,5	1373,4	1373,45	0,01	2123,8	2123,6	2123,70	0,01	2,82	0,75
2		P33	2341,8	2342,4	2342,10	0,03	1518	1517,9	1517,95	0,01	2350,1	2350,1	2350,10	0,00	2,81	0,96
2		P34	1270,8	1271,1	1270,95	0,02	823,5	824,2	823,85	0,09	1273,6	1273,7	1273,65	0,01	2,83	0,60
4	Red colored bed	P35	2089,9	2090,6	2090,25	0,03	1350,5	1350,8	1350,65	0,02	2132,4	2132,2	2132,30	0,01	2,67	5,38
3		P36	3030,8	3031,7	3031,25	0,03	1962,1	1961,8	1961,95	0,02	3054,6	3054,6	3054,60	0,00	2,77	2,14
3	Red colored bed	P37	2432,8	2433,2	2433,00	0,02	1553,5	1553,6	1553,55	0,01	2475,8	2475	2475,40	0,03	2,64	4,60
3		P38	2578,2	2578,7	2578,45	0,02	1670,9	1670,2	1670,55	0,04	2590,5	2590,2	2590,35	0,01	2,80	1,29
4		P39	2198,4	2198,8	2198,60	0,02	1421,6	1421,5	1421,55	0,01	2218,5	2218,6	2218,55	0,00	2,76	2,50
4		P40	3699,1	3699,8	3699,45	0,02	2394,6	2394,5	2394,55	0,00	3733,9	3733,9	3733,90	0,00	2,76	2,57
3		P41	2940,3	2940,9	2940,60	0,02	1907,4	1907,3	1907,35	0,01	2947,1	2947,5	2947,30	0,01	2,83	0,64
3		P42	1250,6	1251,1	1250,85	0,04	812,3	812,4	812,35	0,01	1253	1252,6	1252,80	0,03	2,84	0,44
3		P43	1934,6	1935,3	1934,95	0,04	1250,1	1250	1250,05	0,01	1940,5	1939,3	1939,90	0,06	2,80	0,72
4		P44	1420,1	1420,4	1420,25	0,02	917,8	917,4	917,60	0,04	1442,4	1442,3	1442,35	0,01	2,71	4,21
4		P45	1176,8	1177,5	1177,15	0,06	760,4	760,5	760,45	0,01	1193,6	1193,3	1193,45	0,03	2,72	3,76
4		P47a	1847,5	1847,9	1847,70	0,02	1186	1185,5	1185,75	0,04	1873,9	1873,1	1873,50	0,04	2,69	3,75
4		P47b	2879,7	2880,2	2879,95	0,02	1850,2	1849,5	1849,85	0,04	2917,5	2917,3	2917,40	0,01	2,70	3,51
4		P47c	2069,5	2070	2069,75	0,02	1333,6	1333,5	1333,55	0,01	2094,6	2094	2094,30	0,03	2,72	3,23
4		P47d	1753,9	1753,9	1753,90	0,00	1127,6	1127,6	1127,60	0,00	1780,4	1779,2	1779,80	0,07	2,69	3,97
4		P47e	3549,4	3549,8	3549,60	0,01	2284,6	2283,9	2284,25	0,03	3589,3	3589,4	3589,35	0,00	2,72	3,05
5	Breccie	P48	1455,1	1455,3	1455,20	0,01	941,3	941,2	941,25	0,01	1466,1	1465,9	1466,00	0,01	2,77	2,06
5	Breccie	P49	1635,5	1636	1635,75	0,03	1058,2	1058	1058,10	0,02	1643	1642,8	1642,90	0,01	2,80	1,22
3		PPK61	1396,1	1395,5	1395,8	0,04	904,1	904,2	904,15	0,01	1398,8	1398,5	1398,65	0,02	2,82	0,58
3		PPK62	2783,5	2783,8	2783,65	0,01	1797,5	1796,7	1797,10	0,04	2786,2	2785,6	2785,90	0,02	2,82	0,23
3		PPK63	948,6	948,9	948,75	0,03	612	612,5	612,25	0,08	950,9	950,9	950,90	0,00	2,80	0,63
3		PPK632	872,9	873,2	873,05	0,03	563,7	564	563,85	0,05	875,5	875,8	875,65	0,03	2,80	0,83
3		PPK65	879,8	880	879,9	0,02	567,8	567,9	567,85	0,02	883,2	883,3	883,25	0,01	2,79	1,06
5	Breccie	P12	3356,5	3356,6	3356,55	0,00	2158,6	2158,6	2158,6	0	3398,9	3399,9	3399,4	0,03	2,71	3,45
3		P23	1842,5	1842,3	1842,4	0,01	1190	1190	1190	0	1847	1846,6	1846,8	0,02	2,81	0,67
3	Red colored bed	P22	2449,6	2449,7	2449,65	0,00	1576,5	1576,2	1576,35	0,02	2477,3	2478,2	2477,75	0,04	2,72	3,12
3		P24	1214,8	1214,6	1214,7	0,02	785,9	786	785,95	0,01	1220,4	1219,8	1220,1	0,05	2,80	1,24
5	Breccie	P17	1078,1	1078,5	1078,3	0,04	689,3	689,1	689,2	0,03	1089,1	1088,6	1088,85	0,05	2,70	2,64
5	Breccie	P19	1009,1	1009,4	1009,25	0,03	648,2	648,2	648,2	0,00	1019,6	1019	1019,3	0,06	2,72	2,71
6	Katak-lasit	P48	3877,5	3878,1	3877,8	0,02	2508,9	2508,2	2508,55	0,03	4006,8	4007	4006,9	0,00	2,59	8,62
6	Katak-lasit	P5.2	2961,3	2961,9	2961,6	0,02	1917,4	1916,9	1917,15	0,03	3031,3	3032,6	3031,95	0,04	2,66	6,31
4		Pr2FDC4-1	3816,9	3816,4	3816,65	0,01	2455,8	2456	2455,9	0,01	3866,1	3866,4	3866,25	0,01	2,71	3,52

3		PR2-43m	3466,7	3467,3	3467	0,02	2246,7	2246,6	2246,65	0,00	3479,5	3479,6	3479,55	0,00	2,81	1,02
3		Pr2-27,2m	3979,7	3980,1	3979,9	0,01	2567,4	2567,6	2567,5	0,01	3989,9	3991,3	3990,6	0,04	2,80	0,75
3		PR2FDC3-3	2258,7	2259,2	2258,95	0,02	1459,4	1459,3	1459,35	0,01	2267	2266,8	2266,9	0,01	2,80	0,98
3		PR2FDC3-1	1914,6	1915,3	1914,95	0,04	1241,7	1242	1241,85	0,02	1923	1922,5	1922,75	0,03	2,81	1,15
3		Pr2-31m	2428	2428,7	2428,35	0,03	1564,9	1565,1	1565	0,01	2440,2	2441	2440,6	0,03	2,77	1,40
2		Pr2-10,9m	2189,7	2190,2	2189,95	0,02	1415,3	1425,5	1420,4	0,72	2193,9	2193,6	2193,75	0,01	2,83	0,49
5	Breccie	KAT1-4	1766,2	1766,4	1766,3	0,01	1128,9	1128,8	1128,85	0,01	1782,1	1783,1	1782,6	0,06	2,70	2,49
5	Breccie	Kat1-2	1382,5	1382,8	1382,65	0,02	890,7	890,9	890,8	0,02	1390	1389,6	1389,8	0,03	2,77	1,43
5	Breccie	Kat1-10,7m	2365,5	2365,9	2365,7	0,02	1520,8	1519,6	1520,2	0,08	2385	2385,9	2385,45	0,04	2,73	2,28
2		Pr2-16,2m	1539,6	1540,1	1539,85	0,03	997,2	997,1	997,15	0,01	1542,1	1542,4	1542,25	0,02	2,82	0,44
2		FDC2-10,7m	2246,3	2247,3	2246,8	0,04	1457	1452,2	1454,6	0,33	2251,6	2251,9	2251,75	0,01	2,82	0,62
2		FDC2-2	1399,6	1399,7	1399,65	0,01	906,1	905,9	906	0,02	1403,5	1404,2	1403,85	0,05	2,81	0,84
2		FDC2-1	1819,1	1819,6	1819,35	0,03	1177,1	1176,6	1176,85	0,04	1824,4	1823,9	1824,15	0,03	2,81	0,74
2		FDC2 14,6m	2653,5	2654,2	2653,85	0,03	1722	1721,7	1721,85	0,02	2657,5	2656,8	2657,15	0,03	2,84	0,35
5	Breccie	Kat113,8m	1673,8	1673,4	1673,6	0,02	1065,2	1065,5	1065,35	0,03	1705,8	1707	1706,4	0,07	2,61	5,12
5	Breccie	Kat1-1	1186,5	1187	1186,75	0,04	766,2	766,5	766,35	0,04	1195,2	1195	1195,1	0,02	2,77	1,95
3		FDC3 35m	1520,1	1520,6	1520,35	0,03	978,2	978,4	978,3	0,02	1529,4	1530,5	1529,95	0,07	2,76	1,74
3		FDC3-3	1976,5	1977,2	1976,85	0,04	1278,2	1278,4	1278,3	0,02	1985,9	1986,8	1986,35	0,05	2,79	1,34
3		FDC3-32m	2964,7	2965,4	2965,05	0,02	1918,5	1916,7	1917,6	0,09	2978,7	2978,3	2978,5	0,01	2,79	1,27
2		FDC2-17m	1634,8	1635	1634,9	0,01	1055,7	1056,7	1056,2	0,09	1639,1	1639,2	1639,15	0,01	2,80	0,73
5	Breccie	Kat2	2161,6	2162,7	2162,15	0,05	1398,3	1399,4	1398,85	0,08	2185	2184,5	2184,75	0,02	2,75	2,88
7	Dilata-tionsB.	PR2-DB2	4659,8	4658,5	4659,15	0,03	2990,9	2986,5	2988,7	0,15	4705,4	4706,8	4706,1	0,03	2,71	2,73
7	Dilata-tionsB.	PR2-DB1	1930,7	1930	1930,35	0,04	1242,1	1242,4	1242,25	0,02	1955,7	1956,5	1956,1	0,04	2,70	3,61
5	Breccie	PR2KAT1-3	1456,8	1457,3	1457,05	0,03	937,8	938,4	938,1	0,06	1468,2	1468,7	1468,45	0,03	2,75	2,15
4		PR2FDC4-25m	2513,7	2514,2	2513,95	0,02	1624,6	1625,1	1624,85	0,03	2526,9	2526,7	2526,8	0,01	2,79	1,42
3		PR2FDC3-45m	1535,5	1535,7	1535,6	0,01	993,7	993,9	993,8	0,02	1544	1545,2	1544,6	0,08	2,79	1,63
3		PR2FDC3-20m	4403,3	4401,8	4402,55	0,03	2836,7	2837,1	2836,9	0,01	4419,2	4419,4	4419,3	0,00	2,78	1,06
4	Red colored bed	PR2FDC4-13,7m	1703	1703,1	1703,05	0,01	1084,4	1084,1	1084,25	0,03	1734,6	1735,2	1734,9	0,03	2,62	4,90
5	Breccia with open vugs	ZB1	1730,3	1730	1730,15	0,02	1111,4	1111,2	1111,3	0,02	1756,9	1758,2	1757,55	0,07	2,68	4,24
5	Breccia	ZB2	2789,8	2789,5	2789,65	0,01	1792,3	1793,4	1792,85	0,06	2806,8	2809,3	2808,05	0,09	2,75	1,81
5	Breccia	ZB3	1811,7	1811,6	1811,65	0,01	1168,7	1169,3	1169	0,05	1849,9	1848,9	1849,4	0,05	2,66	5,55
5	Breccia	ZB4	3710,1	3709,9	3710	0,01	2380,4	2380,6	2380,5	0,01	3732,5	3735,8	3734,15	0,09	2,74	1,78
7	Dilata-tionsB.	DB3	4990,4	4989,7	4990,05	0,01	3191,6	3192,3	3191,95	0,02	5031,8	5038,6	5035,2	0,14	2,71	2,45
5	Breccie	ZB5	4257,6	4257	4257,3	0,01	2746,2	2747,6	2746,9	0,05	4294,3	4298,1	4296,2	0,09	2,75	2,51
5	Breccie	ZB6	3649,9	3648,9	3649,4	0,03	2351,8	2353,6	2352,7	0,08	3680,3	3683,6	3681,95	0,09	2,75	2,45
6	Katak-lasit	K1	1187,7	1187,6	1187,65	0,01	769,8	770,5	770,15	0,09	1229,9	1231	1230,45	0,09	2,58	9,30
6	Katak-lasit	K2	641,4	641,1	641,25	0,05	415,5	415,8	415,65	0,07	666,8	667,4	667,1	0,09	2,55	10,28

Table 13: Sample Porosity Calculations

Number	Bed thickness[m]	Description of lithology	Porosity Class
1	0,45	rusty, sparitic fenestrae	5
2	0,2200	dark grey	3
3	0,72	light grey	3
4	0,004	siliciclastic layer ("Keuper")	0
5	0,38	medium grey	3
6	0,005	siliciclastic layer ("Keuper")	0
7	0,21	grey, round sparitic lenses	3
8	0,22	grey, algal laminit	3
9	0,4	medium grey	4
10	0,003	siliciclastic layer ("Keuper")	0
11	2,4	o.D..Bedding hard to distinguish	3
12	0,002	siliciclastic layer ("Keuper")	0
13	1,05	light grey, sparitic fissures, rusty	4
14	0,32	medium grey, solid, bulky	2
15	0,7	medium grey	3
16	0,3	rusty layer	5
17	2,22	medium grey, solid, bulky , bedding hard to distinguish	3
18	4,3	medium grey, solid, bulky, bedding hard to distinguish	3
Interception due to intense faulting			
19	0,78	Brekksia with open cavities (fault rock?)	4
20	1,08	medium grey, bulky	3
21	0,001	siliciclastic layer ("Keuper")	0
22	2,23	medium grey, bulky, bedding hard to distinguish	3
23	6,2	medium grey, bulky, bedding hard to distinguish	3
Interception due to intense faulting			
24	2,24	medium grey	3
25	0,33	medium grey, intensely fractured	4
26	0,78	medium grey	3
(27	0,2	Bedding//Cataklasite FAULT ROCK	6)
28	1,91	medium grey, bulky	3
29	0,33	medium grey	4
30	0,005	siliciclastic layer ("Keuper")	0
31	0,28	medium grey	2
32	0,009	siliciclastic layer ("Keuper")	0
33	1,11	medium grey, very similar to 34	3
34	1,13	medium grey, very similar to 33	3
35	0,67	dark grey	3
36	0,31	featureless medium grey	3
37	0,3	featureless medium grey	3
38	0,3	featureless medium grey	3
39	0,31	featureless medium grey	3

40	0,29	featureless medium grey	3
41	0,29	featureless medium grey	3
42	0,31	featureless medium grey	3
43	0,3	featureless medium grey	3
44	0,32	featureless medium grey	3
45	0,28	featureless medium grey	3
46	0,009	siliciclastic layer ("Keuper")	0
47	0,71	rusty, sparitic fenestrae, partly laminated	5
48	0,39	medium grey	4
49	0,001	siliciclastic layer ("Keuper")	0
50	0,97	medium grey	3
51	0,6	red, partly laminated	5
(52	1,1	Bedding//Cataklasite FAULT ROCK	6)
Short profile in upper level of quarry			
53	0,12	grey, sparitic	4
54	1,13	o.d Grau	3
55	0,009	siliciclastic layer ("Keuper")	0
56	0,7	red dolomoite, fenestrae	5

Table 14: Stratigraphic profiles for matrix porosity

FaultCategory	Nr.	Strike of Scan-line [°]	[m]	Slickenside			Slickenline			Shear sense	Fault Rock [cm]total	Fault Rock [cm]/type					WGS 84 UTM33N coordinates	
				Dip Dir [°]	Dip [°]	Strike	Azimuth	Plunge	Kakint			zem. Brekkie	Kataklasit	FDC 4	DilatationsB.	N	E	
0	0	23	0													5314194	586259,1	
5	1	23	0,5	42	77	132			2		2					5314194,469	586259,2993	
5	2	23	0,9	60	75	150			2	3	3					5314194,847	586259,4595	
3	3	23	1,1	241	74	331			0	2	2					5314195,022	586259,5337	
3	4	23	2,0	252	62	342	248	65	0	0		0				5314195,85	586259,8854	
8	5	23	2,4	20	16	110			0	38		9	2	27		5314196,228	586260,0456	
5	6	23	3,0	42	85	132			2	3,5		3	0,5			5314196,78	586260,28	
6	7	23	4,1	98	85	188	12	51	0	6		6				5314197,792	586260,7098	
3	8	23	4,5	240	79	330	320	60	0	8		3		5		5314198,17	586260,87	
3	9	23	5,2	237	54	327			0	20				20		5314198,805	586261,1396	
1	10	23	6,2	138	25	228			0	0,5	0,5					5314199,716	586261,5264	
5	11	23	6,6	33	71	123			2	3,5	0,5			3		5314200,103	586261,6905	
3	12	23	8,4	246	64	336	240	60	0	0						5314201,751	586262,39	
1	13	23	12,5	172	25	262			0	3				3		5314205,525	586263,992	
2	14	23	15,9	314	51	404			0	0						5314208,645	586265,3165	
2	15	23	19,9	151	85	241			0	1	1					5314212,3	586266,8677	
2	16	23	20,6	326	66	416			0	1	1					5314212,962	586267,1491	
2	17	23	21	342	86	432			0	1	1					5314213,331	586267,3054	
2	18	23	21,9	348	81	438			0	119		23		96		5314214,159	586267,657	
0	19	162	22,7						0	0						5314214,895	586267,9696	
2	20	162	23,9	342	50	432			0	3	3					5314216,037	586267,5988	
2	21	162	24,8	326	61	416			0	3	3					5314216,893	586267,3207	
2	22	162	25,1	331	71	421			0	2	2					5314217,178	586267,228	
2	23	162	25,4	318	65	408			0	0,5			0,5			5314217,463	586267,1353	
3	24	162	26,7	250	56	340			0	13	13					5314218,7	586266,7335	
4	25	162	29,7	228	89	318			0	4	4					5314221,553	586265,8065	
4	26	162	31,1	209	85	299			0	5					5	5314222,884	586265,3739	
4	27	162	31,6	225	81	315			0	3				3		5314223,36	586265,2193	
4	28	162	35,7	209	84	299			0	5		5				5314227,259	586263,9524	
4	29	162	39,7	211	76	301	292	40	0	37		2		35		5314231,063	586262,7163	
4	30	128	41,3	202	71	292			0	18				18		5314232,585	586262,2219	
3	31	128	43,6	231	56	321			0	40,5		0,5		40		5314234,001	586260,4095	
1	32	128	52,1	138	21	228			0	2	2					5314239,234	586253,7114	
1	33	128	53,1	126	25	216			0	1	1					5314239,85	586252,9234	
1	34	128	53,6	128	17	218			0	1	1					5314240,158	586252,5293	
2	35	128	57,4	323	70	413			0	2	2					5314242,497	586249,5349	
3	36	128	58,4	246	89	336	325	52	0	2,5	2,5					5314243,113	586248,7469	
3	37	128	59,9	263	86	353			0	2,5	2,5					5314244,036	586247,5649	
0	38	128	63						0	0						5314245,945	586245,122	

Table 15: Data from scanline 1

Category	Strike of Scanline [°]	[m]	Slickenside			Slickenline			Fault Rock [cm]/type	WGS 84 UTM33N coordinates						
			Dip Dir [°]	Dip [°]	Strike(symb)	Azimuth	Plunge	Shear sense		Fault Rock [cm]total	Kakirit	zem. Brekkie	Kataklasis	FDC 4	DilatationsB.	N
0	20	0													5314212,3	586366,7
3	20	1,1	236	76	326								7		5314211,266	586366,324
0	20	3,3	108	30	198				0						5314209,199	586365,571
2	20	7,9	327	65	417				0						5314204,876	586363,998
1	20	8,8	78	40	168				1		1				5314204,031	586363,69
4	20	10,50	212	86	302	210	80	2	28		2		26		5314202,433	586363,109
3	20	21,1	244	59	334			2	12	2			10		5314192,472	586359,483
0	62	21,5							0						5314192,097	586359,347
1	62	21,6	82	50	172	84	50		8,5			0,5	8		5314192,05	586359,258
4	62	29,4	210	61	300			2	25				25		5314188,388	586352,371
1	62	34,6	86	34	176				0						5314185,947	586347,78
4	62	36,2	20	89	110	20	89		0,2			0,2			5314185,195	586346,367
3	62	38,9	240	50	330				99		48		51		5314183,928	586343,983
3	62	42,8	239	74	329				3	3					5314182,097	586340,54
3	62	44,800	239	49	329				2	2					5314181,158	586338,774

Table 16: Data from scanline 2

Category	Strike of Scanline [°]	[m]	Slickenside		Slickenline		Shear sense	Fault Rock +DC[cm]total	Fault Rock [cm]/type					WGS 84 UTM33N coordinates	
			Dip Dir [°]	Dip [°]	Azimuth	Plunge			Kakirit	zem. Brekkzie	Kataklasit	FDC 4	Dilatation B.	Z	E
0		0												5314257,60	586258,17
6	88	0,15	260	50				11	11					5314257,61	586258,32
4	88	8,22	212	80	302	40		14	7			7		5314257,89	586266,38
4	88	10,45	210	85	296	50		12	4	7	1			5314257,96	586268,61
4	88	21,2	202	89				36	3			33		5314258,34	586279,36
8	130	3,54	156	30				3	1	2				5314256,06	586282,07
6	130	6,22	110	60				2				2		5314254,34	586284,12
6	130	7	84	70	70	70		0						5314253,84	586284,72
1	130	8,31	110	35				0						5314253,00	586285,72
1	130	14,42	112	35				2	2					5314249,07	586290,40
0	130	18,22						0						5314246,63	586293,31
1	70	4,63	100	20	66	15		0						5314248,21	586297,67
1	70	4,63	80	50	70	45		2	1			1		5314248,21	586297,67
1	70	7,22	80	45				2	1			1		5314249,1	586300,10
1	70	7,22	92	50				2	1			1		5314249,1	586300,10
3	70	7,51	230	75				2	2					5314249,2	586300,37
1	70	8,02	90	30				20	3			17		5314249,37	586300,85
4	70	10,12	202	89	290	27		38,5	15	2,5	1	20		5314250,09	586302,82
3	70	15,23	232	60				60	60					5314251,84	586307,63
0	70	18,73						0						5314253,03	586310,91
6	60	0	278	60				13	13					5314253,03	586310,91
4	60	9,21	200	89				4	2			2		5314257,64	586318,89
3	60	14,11	250	65			2	12	12					5314260,09	586323,13
3	60	19,82	240	85			2	45,5			0,5	45		5314262,94	586328,08
6	60	19,82	280	60			2	25				25		5314262,94	586328,08
3	60	22,42	240	65				4			2	2		5314264,24	586330,33
4	60	34,22	200	80				52		20		32		5314270,14	586340,55
3	60	34,22	244	89				22				22		5314270,14	586340,55
3	60	35,63	230	80				21				21		5314270,85	586341,77

Table 17: Data from scanline 3

Category	Strike of Scanline [°]	[m]	Slickenside		Slickenline		Shear sense	Fault Rock +DC[cm]total	Fault Rock [cm]/type					WGS 84 UTM33N Coordinates	
			Dip Dir [°]	Dip [°]	Azimuth	Plunge			Kakirit	zem. Brekkzie	Kataklasiit	FDC 4	DilatationsB.	N	E
7	90	0	1	75				0,5	0,5					5314291	586279
2	90	2,31	328	80				0,5	0,5					5314291	586281,31
2	90	2,55	320	75				2	2					5314291	586281,55
3	90	5,71	240	85	308	25	1	6	6					5314291	586284,71
4	90	6,4	218	55				0	>1					5314291	586285,4
4	90	7,3	220	80				3	3					5314291	586286,3
2	90	8,2	310	85				2	2					5314291	586287,2
5	90	9,2	42	85				3	3					5314291	586288,2
5	90	10,02	50	85				4	4					5314291	586289,02
3	90	10,31	240	75				4	4					5314291	586289,31
3	90	15,21	254	70				20	20					5314291	586294,21
3	90	17,81	240	80				4	4					5314291	586296,81
3	90	19,22	248	75				40				40		5314291	586298,22
4	90	23,12	218	84				3	3					5314291	586302,12
3	90	24,02	228	60				20	20					5314291	586303,02
2	90	24,8	320	57				20	20					5314291	586303,8
4	90	28,8	212	89				6	6					5314291	586307,8
5	90	28,8	35	53	35	46		4	4					5314291	586307,8

Table 18: Data from scanline 4

Category	Strike of Scanline [°]	[m]	Slickenside		Slickenline		Shear sense	Fault Rock +DC[cm]total	Fault Rock [cm]/type					WGS 84 UTM33N Coordinates	
			Dip Dir [°]	Dip [°]	Azimuth	Plunge			Kakirit	zem. Brekkzie	Katakklasit	FDC 4	DilatationsB.	N	E
0	174	0						0						5314238	586399
7	174	0,91	12	89				1	1					5314237,09	586399,0951
7	174	3,72	182	79				10	10					5314234,3	586399,3888
6	174	4,8	82	75				2	2					5314233,23	586399,5017
2	174	9,71	308	80				0	0					5314228,34	586400,015
4	174	11,2	194	60				2			2			5314226,86	586400,1707
4	174	12,91	204	89				8	4	4				5314225,16	586400,3495
7	174	15,72	180	80				4	4					5314222,37	586400,6432
7	174	17,02	20	70				0	0					5314221,07	586400,7791

Table 19: Data from scanline 5

Zusammenfassung

Diese Masterarbeit beschäftigt sich mit der Abschätzung der effektiven Porosität der im Steinbruch Grossau bei Bad Vöslau aufgeschlossenen Hauptdolomit-Formation und der Beschreibung der dort vorkommenden Störungsgesteine.

Zur Bestimmung der effektiven Porosität wurden Messungen an typischen zementierten Störungsgesteinen und Dolomiten unterschiedlicher Kluftdichteklassen basierend auf ÖNORM EN 1936 bzw. ÖNORM B 3121. Weiters wurde eine Kartierung der Bruchflächen und Störungsgesteine entlang verschieden orientierter Profillinien durchgeführt. Die gemessenen Störungsflächen wurden in sieben Gruppen subparalleler Flächen eingeteilt. Um das Trennflächengefüge des Gebirges zu beschreiben wurden für jede dieser Gruppen die Normalabstände zwischen den einzelnen Störungen berechnet. Um den orientierungsbedingten systematischen Fehler der Profilaufnahme zu charakterisieren wurde für jede Gruppe von Störungen die Länge der Profillinie ihrer Entsprechung in der Richtung normal zu den Störungsflächen gegenübergestellt bzw. der beprobte Normalabstand in Prozent der Scanlinienlänge ausgedrückt.

Zur Abschätzung der effektiven Porosität des Gebirges wurden die Dolomite nach der Kluftdichte klassifiziert und die Volumsanteile der unterschiedlichen Kluftdichteklassen und Störungsgesteine am Gesamtgesteinsvolumen aus Profillinien ermittelt. Den Volumsanteilen der unterschiedenen Gesteinstypen wurden die Porositätswerte aus obigen Messungen zugeordnet. Für die für diese Art der Porositätsmessung nicht geeigneten kohäsionslosen Störungsgesteine wurde ein Bereich von Schätzwerten basierend auf Literaturwerten für die effektive Porosität von Lockersedimenten verwendet. Die daraus errechnete effektive Porosität der Gesteinsmasse liegt zwischen 1.7 und 2%.

Die Profilliniendaten zur Orientierung und Mächtigkeit von Trennflächen/Störungen, Störungsgesteinen und Zerrüttungszonen von Störungen erlauben aber Aussagen zur richtungsabhängigen Trennflächenhäufigkeit und Dimension der Störungsgesteine/Zerrüttungszonen im Gebirge. Drei Gruppen häufiger NNW- bis WNW streichender steiler Störungen durchschlagen jeweils den gesamten sichtbaren Aufschlussbereich und dürften für eine erhöhte Permeabilität zumindest im Verlauf ihrer mächtigen, nicht zementierten Zerrüttungszonen sorgen. Klassifikationsschemata für Störungsgesteine aus der Literatur werden im Hinblick auf ihre Anwendbarkeit am Mikroskop bzw. im Feld an Beispielen aus Grossau diskutiert. Mögliche Prozesse der Entstehung von karbonatischen Störungsgesteinen und ihrer (Mikro-) Strukturen werden anhand von Dünnschliffbeobachtungen aus Grossau und der Literatur besprochen.

Abstract

This master thesis deals with the assessment of the effective porosity of rocks of the Hauptdolomit Formation and the description of fault rocks cropping out in the quarry Grossau near Bad Vöslau. Effective porosity of rocks, which are categorized in different fracture density-, porosity- and fault rock classes, was determined using testing methods based on ÖNORM EN 1936 and ÖNORM B 3121, respectively.

Fault orientation and the distribution of fracture density classes and fault rock categories were assessed along scanlines of different orientation to minimize scanline bias. Right angle distance equivalents of total scanline lengths and right-angle-distances for faults within seven classes of sub parallel faults were determined and used to overcome scanline bias and describe the directional anisotropy of the rock mass. The approach uses the comparison between scanline length and right angle distance equivalent for each fault class. Data include the frequency and thickness of fault in the right-angle direction for each fault class.

The effective porosity of the bulk rock mass is assessed as a weighted mean by assigning the values measured for each rock type to their proportion in a lithostratigraphic profile (for the fracture density classes) and their proportion within the scanlines (for the fault rocks). For cohesionless fault rocks a range of effective porosity values based on literature data for the effective porosity of loose sediments was used. The calculated porosity values for the bulk rock mass range between 1.7 and 2%. The scanline data about orientation and thickness of fractures, faults, fault rocks and damage zones of faults allow calculations of the directional frequency of fractures and faults, and the dimension of fault rocks and damage zones. Three groups of steep NNW to WNW striking faults with occur with high frequency and well developed uncemented damage zones penetrate the entire visible outcrop area and are likely to cause a higher permeability of the rock mass in this direction. Classification schemes for fault rocks and proposed mechanisms for their genesis from the literature are discussed based on observations from the field, samples and thin sections from Grossau.